Solar Radiation in Large-Eddy Simulations Coupled to a General Circulation Model

by

E.D. van Laarhoven

to obtain the degree of Master of Science
in Applied Physics
at the Delft University of Technology,
to be defended on Thursday May 2, 2019 at 14:00.

An electronic version of this thesis is available at `http://repository.tudelft.nl/`.

TUDelft

Acknowledgements

A year ago, I embarked on an exciting voyage in the field of atmospheric science. This thesis is the final report of that adventure. Besides being very enjoyable and instructive, this project also turned out to become a battle with larger datasets than I was accustomed to work with, in programming languages I had yet to learn, using data formats I had never seen before. It goes without saying then, that the arrival of this thesis did not come without help. Although this section is too short to thank everyone I am grateful of, several people deserve to be mentioned in specific.

Words fall short in expressing my deep gratitude to prof. Harm Jonker. The immense amount of time spent in discussing my observations, lecturing me in atmospheric science on the ever crowded whiteboard and reviewing my work again and again is exceptionally praiseworthy. I admire his seemingly infinite knowledge, which guided me through a plethora of data and helped finding the right results. I feel very privileged to have been trusted a place inside his business, and genuinely hope that my findings may form a modest contribution to the development of GRASP.

I also don't know where to start in thanking Pim van Dorp. His contributions to this research are countless, ranging from the many lessons in Python to providing and arranging forecast data for my analyses. I am not sure if I have expressed how much I have appreciated the ability to use his data processing tools and that he always had time to help me with my struggles and questions. I don't think every graduate student becomes friends with his supervisor, and I am happy to say that I have.

I want to thank the entire staff of Whiffle B.V. for making me feel right at home in their midst. Having been part of the development that is driven by these guys (and understanding how complicated this can be), I have gained a deep respect for the work that is performed on a daily basis. I want to thank Evert in particular for his help in setting up an interactive development environment. I also want to thank Remco, Peter, Gerrit, Erwin and Bob. Their tips and tricks have been more valuable to me than they probably know.

I am furthermore grateful to my friends and family for patiently keeping up with my endless contemplation on clouds and radiation. I can only imagine that listening to my gibberish about atmospheric processes (which I did not always fully comprehend myself at that time) can have been a tedious pastime, but those who remained patiently interested in my project are those who have (perhaps unknowingly) contributed to its realization.

Last but not least, I want to thank the reader in advance. For every reader outside the field of atmospheric science, please don't worry if the terminology or concepts in this thesis sound confusing. Instead, next time you see the daily weather forecast on the news, take a moment to appreciate the beautiful complexity by which a combination of all fields of physics collaborate in the art of numerical weather prediction. I definitely know I will.

Ewout van Laarhoven
Delft, April 2019

Abstract

The present study aims to assess and advance the prediction skill of solar radiation in high resolution weather forecasts by large-eddy simulations (LES). The GPU-Resident Atmospheric Simulation Platform (GRASP) was used to simulate the atmosphere around the Cabauw experimental site for atmospheric research (CESAR) in the Netherlands. Large-scale boundary conditions were provided by coupling the simulation to a general circulation model (GCM). Radiative tendencies were calculated using two different implementations of the Rapid Radiative Transfer Method for GCMs (RRTM-G): one runs in advance of the simulation using pre-calculated atmospheric fields, the other employs dynamically updated fields during the simulation. Both configurations generated simulations of every day in 2016, which were compared to each other and validated using observations from the Baseline Surface Radiation Network (BSRN).

This study revealed that the implementation of interactive radiation altered cloud representation in the simulations, in most cases causing clouds to rise. This process correlated with an increase in turbulence kinetic energy of up to 2 m^2/s^2 locally. The clouds that were raised tended to break up more often between 5 and 7 km altitude, leading to a decrease in average cloud fraction and increase in short-wave down-welling radiation. The results suggest that the implementation of interactive radiation enabled the development of cloud top entrainment instabilities, which could be responsible for the cloud breakup in these cases.

Regardless of the chosen implementation of the radiative transfer method, large errors are made in the prediction of surface solar radiation. GRASP produced root mean squared errors (RMSE) of 122.4 W/m^2 and 115.7 W/m^2 using prescribed and interactive radiation, respectively, while the large-scale model used to provide the initial and boundary conditions to the simulation produced an RMSE of 87.3 W/m^2. The large error in GRASP's prediction of surface solar radiation can partly be attributed to conversion errors made during GRASP's initialization of the thermodynamic state, which lead to erroneous diagnoses of the liquid water content in the atmosphere.

Contents

6 Conclusions   **51**

A Extra Results   **53**

B A Note on Statistics   **59**

Bibliography   **63**

Nomenclature

Acronyms

BOMEX	Barbados Oceanographic and Meteorological Experiment
CESAR	Cabauw experimental site for atmospheric research
CEST	Central European Summer Time
CET	Central European Time
CPU	Central processing unit
DALES	Dutch Atmospheric Large-Eddy Simulation
DNS	Direct numerical simulation
ECMWF	European Centre for Medium-Range Weather Forecasts
ERA5	Fifth generation of ECMWF's atmospheric reanalysis forecast
GALES	GPU-resident Atmospheric Large-Eddy Simulation
GCM	General circulation model
GCOS	Global Climate Observing System
GEWEX	Global Energy and Water Experiment
GRASP	GPU-resident Atmospheric Simulation Platform
GRASP-I	GRASP with interactive radiation
GRASP-P	GRASP with prescribed radiation
GPU	Graphics processing unit
IFS	Integrated Forecasting System
IR	Infra-red
LES	Large-eddy simulation
LWD	Long-wave down-welling radiation
MAE	Mean absolute error
NWP	Numerical weather prediction
RMSE	Root mean squared error
rRMSE	Relative root mean squared error
RRTM	Rapid Radiative Transfer Model
RRTM-G	Rapid Radiative Transfer Model for GCMs
SWD	Short-wave down-welling radiation
TKE	Turbulence kinetic energy
TCIW	Total column ice water
TCLW	Total column liquid water
TCWV	Total column water vapor
UTC	Coordinated Universal Time
UV	Ultraviolet
WCRP	World Climate Research Programme

Symbols

α	Cloud fraction, or attenuation coefficient
θ	Solar zenith angle
θ_l	Liquid water potential temperature
θ_v	Virtual potential temperature
κ_v	Absorption coefficient at a specified frequency v
ρ	Density
σ	Standard deviation
τ_v	Optical thickness of a material for a specified frequency v
$\vec{\Omega}$	Earth's angular velocity vector
c_{pd}	Specific heat capacity of dry air
g	Earth's gravitational force
I_v	Intensity at a specified frequency v
L	Latent heat release upon vaporization
$L^\downarrow$	Long-wave down-welling radiation
$L^\uparrow$	Long-wave up-welling radiation
P	Precipitation rate
p	Pressure
p_{ref}	Reference pressure
Q_r	Radiative heating rate
q_c	Cloud specific humidity
q_i	Ice water specific humidity
q_l	Liquid water specific humidity
q_r	Precipitating water specific humidity
q_t	Total (non-precipitating) water specific humidity
q_v	Water vapor specific humidity
R_d	Specific gas constant of dry air
R_v	Specific gas constant of water vapor
$S^\downarrow$	Short-wave down-welling radiation
$S^\uparrow$	Short-wave up-welling radiation
$S_{\mathrm{b}}^\downarrow$	Short-wave down-welling radiation at the bottom of the atmosphere
$S_{\mathrm{b,clr}}^\downarrow$	Short-wave down-welling radiation at the bottom of the atmosphere for clear skies
$S_{\mathrm{t}}^\downarrow$	Short-wave down-welling radiation at the top of the atmosphere
T	Temperature
$\vec{u}$	Wind velocity vector
$\vec{u_g}$	Geostrophic wind velocity vector
w	Entrainment rate

Introduction

1.1 Weather forecasting for renewable energy technologies

Over the past few decades, the accuracy of weather forecasts has greatly improved as a result of steady advances in scientific knowledge and technological progress. This is rather impressive if one considers the complexity of all interactive atmospheric processes, the chaotic nature of the partial differential equations that govern fluid motion and the limited capability to execute repeatable physical experiments on the atmosphere.

Accurate forecasts support the management of emergency operations, prevent economic losses from extreme weather events and provide predictions of electric energy generation by renewable energy technologies. The latter includes providing wind farm operators with high-resolution wind forecasts (Mc Garrigle and Leahy, 2013), or forecasting solar irradiance for users of photovoltaic systems (Lorenz et al., 2009). These renewable energies have the major disadvantage that their availability depends on the ever-changing state of the atmosphere, impeding the ability to adjust their power output as conveniently as conventional power plants.

Producers and distributors of renewable energy are challenged by the fluctuating nature of wind and solar power production as a result of unexpected meteorological variations. If these fluctuations were to be predicted ahead of time, the value of these renewable energies would increase substantially. Fortunately, wind power forecasts already exist, predicting the amount of power that can be expected a day ahead. This enables efficient adoption of wind-generated energy into the electricity supply and aids scheduling of conventional power stations (Lange and Focken, 2006).

1.2 Challenges in radiative transfer methods

Clouds play an important role in the quality of solar radiation forecasts because of their impact on radiative transfer, but they are not always easy to resolve. Cumulus clouds in particular are notoriously difficult to represent in numerical weather prediction (NWP) models (Arakawa, 2004). Large-eddy simulations (LES) are mathematical models which are however characterized by a spatial resolution which is high enough to simulate the cumuli (Siebesma et al., 2003), which makes them serious candidates for solar energy forecasts.

Even with accurate cloud representations, the calculation of radiative transfer through the atmosphere remains one of the many challenges in these simulations. The theory behind radiative transfer is very well known, but the computational costs associated with exhaustive calculations are unacceptably high for use in LES, let alone at operational time-scales. To balance accuracy and computational cost, many approximate methods are available, and each contains the risk of introducing errors that might change the overall simulation.

1.3 Prescribed and interactive radiation

One such approximation is to prescribe radiation, or more exactly, prescribe the radiative tendencies that should occur at some specified time and place, before running the actual simulation. This is for example possible if one calculates the heating rates based on another already known, large-scale forecast (at lower resolution). An important disadvantage of this approach is that the radiative tendencies that operate on the simulation are detached from the actual thermodynamic state in that simulation. The dashed lines in figure 1.1 indicate the feedback loops that cannot take place as a consequence.

Radiative tendencies
Heating and cooling

Affects turbulent entrainment through heating/cooling

Determines magnitude and vertical distribution of heating/cooling

Affects condensation and evaporation through heating/cooling

Internal dynamics
Entrainment
Turbulent motions

Affects condensation and evaporation through mixing

Cloud microphysics
Ice/liquid water content
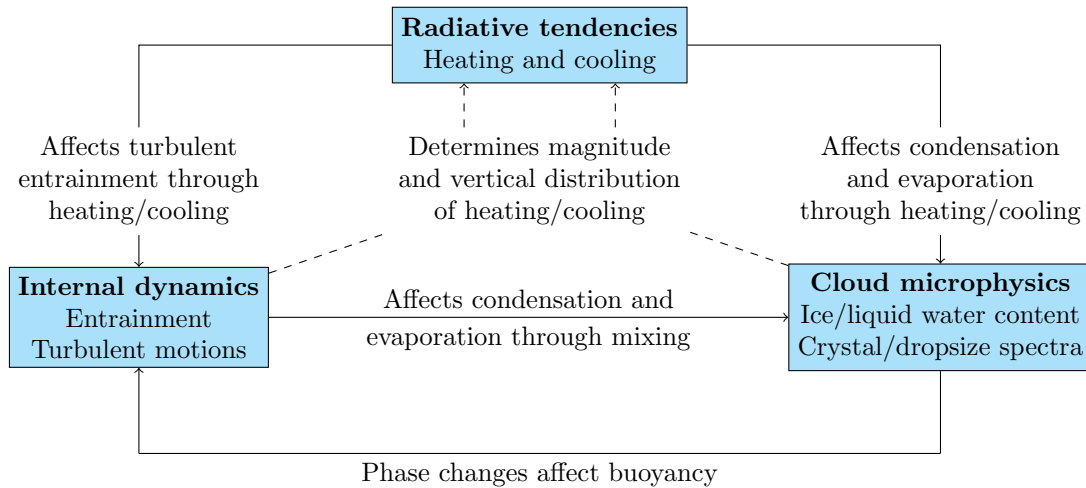Crystal/dropsize spectra

Phase changes affect buoyancy

Figure 1.1: Schematic diagram of the interactions between turbulence, radiation and cloud microphysics. The dashed lines indicated processes that are detached from the main simulation when prescribed radiation is used. Adapted from Curry (1986).

Although the use of prescribed radiation has been justified for some academic cases (e.g. the Barbados Oceanographic and Meteorological Experiment, or BOMEX, see Jiang and Cotton, 2000), there are many interactive feedback loops between clouds and radiation that deem such an approach undesirable for general operational forecasts that need to perform in a wide range of possible meteorological conditions. Figure 1.2 illustrates a few complications that could arise by using prescribed radiation. Suppose the large-scale GCM forecast (shown on the left) differs in its cloud representation from the LES (shown in the middle and right) as is shown in the illustration. In this case, the radiative tendencies that are applied to the LES with prescribed radiation are inconsistent with its actual thermodynamic state: cloud-top radiative cooling and cloud-bottom radiative heating are applied in cloud-free regions, no radiative heating or cooling is applied where there are clouds, and there is more solar radiation underneath the clouds than underneath clear skies. In contrast, the LES with interactive radiation may too differ in its cloud representation, but the radiative tendencies applied on the simulation are coherent with the simulation itself. Since many essential flows are influenced directly by radiative heating and cooling, it seems reasonable that the implementation of an interactive radiative transfer method (in which the radiative tendencies are evaluated during the simulation using the prevailing state of the atmosphere) might provide more realistic simulations and hence more accurate predictions of radiation itself.

This study expands on the previous work of Schalkwijk et al. (2012), who showed increased speed and resolution by porting LES models to run on graphics processing unit (GPU) systems. Schalkwijk et al. (2015a) furthermore reported the ability to represent a diverse range of weather simulations, including numerous transitions, which is promising for operational weather forecasts. Visualizations of cloud fields by Schalkwijk et al. (2015b) display accurately simulated cumulus clouds. The GPU-implementation of Schalkwijk et al. (2012) favored prescribed radiation, as no full radiative transfer method has yet been ported to GPU, and
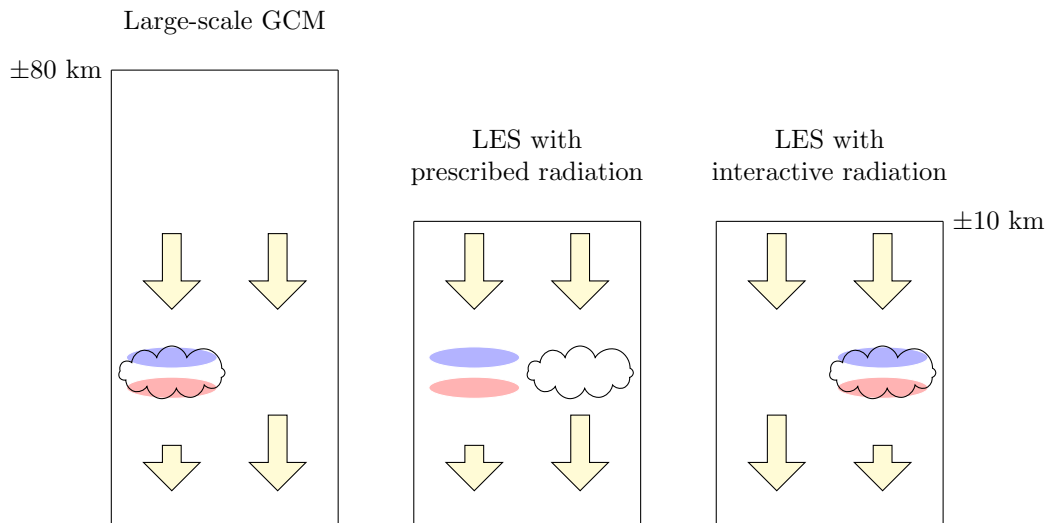
Large-scale GCM

±80 km

LES with
prescribed radiation

LES with
interactive radiation

±10 km

Figure 1.2: A simplified representation of the atmosphere in different simulations that high-lights some complications of prescribed radiation. Yellow arrows indicate solar fluxes, red and blue regions indicate radiative heating and cooling, respectively. The large-scale GCM is shown on the left. The middle simulation shows a LES with a different cloud representation than the GCM, which uses prescribed radiation: its radiative tendencies and fluxes are calculated on the basis of the GCM. The simulation on the right shows a LES with a different cloud representation than the GCM, which uses interactive radiation: the radiative tendencies and fluxes are calculated on the basis of the thermodynamic state in the LES itself.

continuous communication between CPU-based radiation and GPU-based flow calculations slows down the overall simulation. More importantly, the high vertical resolution of the LES almost doubles the number of calculations that need to be performed by the radiative transfer module.

1.4 The goal of this thesis

It is reasonable to assume that a combined ability to resolve cloud fields at the resolution of cumulus clouds with an interactive treatment of radiation could increase the predictive skill of down-welling solar radiation, thus enhancing the overall simulation. To what extent an implementation of interactive radiation (or its absence) has impact on the predictive skill of this particular LES model is not well known.

   The main goal of this research is to assess and advance the prediction skill of solar radiation in day-ahead LES forecasts. This thesis compares the effects of applying prescribed and interactive radiative tendencies. The impact of interactive radiation will be evaluated on a qualitative and quantitative basis. The goal of the qualitative study is to obtain an understanding of the different thermodynamics associated with the two configurations of radiative transfer. The goal of the quantitative study is to assess the prediction skill of solar radiation in these forecasts using both radiative methods.

1.5 Outline

The goal of chapter 2 is to build the theoretical framework required to understand the research that has been performed for this thesis. To this end, we shall first consider the physics that is used to simulate the dynamical flow of the atmosphere, followed by the basics of radiative transfer through the atmosphere. To investigate the cloud-radiation interactions, we have simulated every day in 2016 in two configurations: once using prescribed radiation and once using interactive radiation. How this was done is explained in chapter 3. The output of these simulations were evaluated with regard to surface radiation observations. The results of these analyses are examined in chapter 4 and further discussed in chapter 5. The conclusions of this study are finally summarized in chapter 6.

2

Theory

2.1 Modeling the atmosphere

Some 50 years before the arrival of the computer, Abbe (1901) suggested that the laws of physics could be used to predict the weather. For meteorology, this was a revolutionary idea, since weather forecasting was at that time mostly accomplished by recognizing the daily weather and connecting this to historic outcomes of similar situations. Abbe, however, proposed to treat weather prediction as a mathematical initial value problem, in which the future state of the atmosphere can be calculated by using the partial differential equations that govern fluid motion, starting from the observed weather. This is the very basic idea upon which the weather forecasts of today are founded.

An attempt to solve these equations by hand was performed by Richardson (1922) during the first World War. It was a spectacular failure, over-predicting an enormous rise of pressure. We now know that the mathematical techniques he used were actually correct, but the initial conditions which Richardson used needed to be smoothed to rule out unrealistic swells in pressure (Lynch, 2006).

Richardson dreamed of creating a 'forecast factory': a theater-like building with an enormous spherical hall, representing the globe. Here a large number of people (which he called 'computers') would be busy calculating the time integration of the basic equations of fluid mechanics for a particular area of the globe, sharing their results with the neighboring areas. He imagined a central director of operations standing in the center of the hall, in charge of the coordination and synchronization of the entire process. The beauty of 'Richardsons dream' lies in the striking similarities between his forecast factory and a modern computer, where many computations are performed in parallel under the command of a central processing unit (CPU), but it would still take a few decades before the first machine-generated weather forecast would be produced.

The Earth's atmosphere is a complex system, comprised of dynamic, chemical, radiative and thermodynamic processes that interact with one another. Furthermore, these processes operate on scales ranging from millimeter to thousands of kilometers and from seconds to weeks. Depending on the application of a certain model, specific processes may be of more or less importance, but in general, most atmospheric models are primarily concerned with the evolution of the scalar fields of temperature, density and pressure, and of the vector fields of wind (air velocity) in time.

The general approach of a numerical weather prediction (NWP) model is to divide the computational domain into volumetric elements called grid cells. For each time step, the physical processes affecting each grid cell are calculated as well as the interactions with neighboring cells. With a fixed amount of computing power, a trade-off between domain size and resolution has to be made. General circulation models (GCMs) are large atmospheric models spanning the entire planet. These models are often used for weather and climate forecasting, but feature relatively coarse grids with a typical spatial resolution ranging from 10-100 km. On the other

end of the spectrum are direct numerical simulations (DNS) which, with spatial resolutions in the order of centimeters, is small enough to explicitly account for the smallest scales of turbulence. As a result of their high resolution, DNS models have a limited domain size as a result.

2.2 Large-eddy simulations

Somewhere in-between are large-eddy simulations (LES), first proposed by Smagorinsky (1963). These simulations can accurately resolve the large scale turbulent motions (large eddies) containing the most energy. Only the small scale motions are modeled, reducing computational cost considerably compared to DNS and therefore enabling larger domains to be evaluated.

Besides the need for simplifying the motions at small spatial scales, there are other processes (such as radiation and cloud microphysics) which are simply too complicated to resolve them explicitly. These processes are however very important, as they drive the heat and momentum budgets on the larger (resolved) scales (Arakawa, 2004). As a solution, a simplified representation of the interactions between these processes and the resolved scales has to be made. These simplified representations are typically called 'parametrizations' in NWPs.

Some processes, such as the motion of large pressure systems, act on scales that are larger than the domain of the simulation, and are therefore also not resolved by the simulation itself. These can be represented by coupling the simulation to a GCM. How this was done for the simulations presented in this thesis will be discussed in chapter 3.

The LES model that was used for this thesis used is called the GPU-Resident Atmospheric Simulation Platform (GRASP). The code of GRASP is based on the Dutch Atmospheric Large-Eddy Simulation (DALES), which is described exhaustively by Heus et al. (2010). DALES is built to study stable and convective boundary layers, including cloudy boundary layers. An implementation of the anelastic approximation was performed by Böing et al. (2012b) to enable simulations of domains higher than the planetary boundary layer. DALES is written in FORTRAN90, and has been ported by Schalkwijk et al. (2012) to run completely on graphical processing units (GPUs) instead of CPUs, which resulted in the GPU-resident Atmospheric Large-Eddy Simulation (GALES). GRASP is a further advancement of GALES.

The goal of this chapter is to build the theoretical framework required to understand the research that has been performed for this thesis. To this end, we shall first consider the physics that is used to simulate the dynamical flow of the atmosphere. Then we will discuss the basics of radiative transfer through the atmosphere, focusing on processes that interact with solar radiation. Not all parametrizations will be discussed in detail here, as some are less essential for understanding the research presented here. The reader interested in these parts of the models is encouraged to visit Heus et al. (2010) as a more extensive starting point.

2.3 The physics of forecasting

The prognostic variables of GRASP are the wind velocity vector $\vec{u}$, the total (non-precipitating) water specific humidity q_t, the precipitating water specific humidity q_r and the liquid water potential temperature θ_l. The vector $\vec{u} = (u, v, w)$ is relatively straightforward, as it denotes the wind velocity in the three directions (x, y, z) where z denotes the vertical direction.

The total (non-precipitating) water specific humidity q_t is defined as the ratio of the mass of non-precipitating water (vapor, liquid and ice) and the mass of dry air in an air parcel. It can be decomposed into the the water vapor specific humidity q_v, the liquid water specific humidity q_l and the ice specific humidity q_i:

$$q_t = q_v + q_l + q_i. \tag{2.1}$$

These specific humidities are also referred to as mass mixing ratios. The distribution of q_t over $\{q_v, q_l, q_i\}$ depends on the temperature and pressure, which dictate the saturation curves of liquid and ice. Since clouds are composed of either liquid, ice, or a combination of both, we can define a cloud specific humidity q_c such that

$$q_c \equiv q_l + q_i \qquad ; \qquad q_t = q_v + q_c. \tag{2.2}$$

The conversion between q_t and q_r is handled by a micro-physics scheme in GRASP. The key difference between the two is that the non-precipitating q_t follows the flow of the fluid whereas the precipitating q_r can develop motion in a different direction.

The liquid water potential temperature θ_l is the temperature a parcel of air would have if all of its liquid water and ice were evaporated and it was adiabatically brought to a reference pressure of $p_{\text{ref}} = 1 \cdot 10^5$ Pa. The approach of using θ_l encapsulates temperature effects of latent heat and pressure, which are not accounted for when using temperature T. It is approximated as (Emanuel, 1994):

$$\theta_l \approx \frac{T}{\Pi} - \frac{L}{c_{pd}\Pi}q_c, \tag{2.3}$$

where

$$\Pi = \left(\frac{p}{p_{\text{ref}}}\right)^{R_d/c_{pd}}, \tag{2.4}$$

and $L = 2.5 \cdot 10^6$ J/kg is the latent heat release upon vaporization, $c_{pd} = 1004$ J/(kg·K) is the specific heat capacity of dry air and $R_d = 287.0$ J/(kg·K) is the specific gas constant of dry air.

The total water specific humidity q_t and the liquid water potential temperature θ_l are convenient variables for LES because they remain invariant under phase changes ($q_v \leftrightarrow q_c$) (Deardorff, 1976). For any conserved variable in general, we can state a very valuable relation called the conservation equation. This relation states that the rate of change ($\partial\phi/\partial t$) of a particular conserved variable ϕ in a certain control volume must always be equal to the transport in and out of that volume ($\vec{\nabla} \cdot \phi\vec{u}$) plus what is produced or consumed inside the volume (S_ϕ). Following the anelastic approximation as was implemented in DALES by Böing et al. (2012b), a base state density ρ_0 is added that only varies in the vertical direction ($\rho_0 = \rho_0(z)$):

$$\frac{1}{\rho_0}\left(\frac{\partial(\rho_0\phi)}{\partial t} + \vec{\nabla} \cdot (\rho_0\phi\vec{u})\right) - S_\phi = 0. \tag{2.5}$$

The conservation equation that is solved in GRASP for $\phi \in \{\theta_l, q_t\}$ reads (Schalkwijk et al., 2015a):

$$\underbrace{\frac{\partial\tilde{\phi}}{\partial t}}_{\text{rate of change}} = -\underbrace{\frac{1}{\rho_0}\vec{\nabla} \cdot (\rho_0\tilde{\phi}\tilde{\vec{u}})}_{\text{resolved}} - \underbrace{\frac{1}{\rho_0}\vec{\nabla} \cdot (\rho_0\widetilde{\phi_{\text{sg}}\vec{u}_{\text{sg}}})}_{\text{sub-grid}}$$

$$\qquad - \underbrace{w^{\text{LS}}\frac{\partial\tilde{\phi}}{\partial z}}_{\text{subsidence}} - \underbrace{\vec{u}_h^{\text{LS}} \cdot \vec{\nabla}_h\phi^{\text{LS}}}_{\text{large-scale advection}} \tag{2.6}$$

$$\qquad + \underbrace{\frac{1}{\tau}\left(\phi^{\text{LS}} - \langle\phi\rangle\right)}_{\text{nudging}} + \underbrace{S_\phi}_{\text{sources}}.$$

The tildes over a variable indicate the part of that variable at the resolved scale. The first term contains the turbulent transport of parameter ϕ on the resolved scale. The second term contains the sub-grid scale transport, which has to be parametrized by a sub-grid model (indicated by the subscript sg). The vertical and horizontal large-scale transport effects are introduced in the third and fourth term, respectively. The variables that are denoted with a superscripted LS indicate that they were obtained from a large-scale model. The subscript h is used to indicate horizontal components. The nudging term is designed to prevent the calculated state from diverging too much from the large-scale model. The angled brackets ($\langle\phi\rangle$) indicate the horizontal slab average. The final term contains sources and sinks of the variable:

$$S_{\theta_l} = Q_r, \tag{2.7}$$

$$S_{q_t} = P, \tag{2.8}$$

with Q_r the radiative heating rate and P the precipitation rate. The heating rate Q_r is where radiation effects are included. It is calculated by the radiative transfer method in GRASP, which will be explained in the upcoming sections.

We can use equation 2.5 for the conservation of momentum as well. In combination with conservation of mass, we then obtain at the Navier-Stokes equations for incompressible fluids:

$$\frac{1}{\rho_0}\left(\frac{\partial(\rho_0\vec{u})}{\partial t} + \vec{u}\cdot\vec{\nabla}(\rho_0\vec{u})\right) = -\frac{1}{\rho_0}\vec{\nabla}p - 2\vec{\Omega}\times\vec{u} + \vec{F}_u, \tag{2.9}$$

$$\vec{\nabla}\cdot(\rho_0\vec{u}) = 0, \tag{2.10}$$

where p is pressure and $\vec{\Omega}$ is Earth's angular velocity vector. The momentum equation that is solved in GRASP is given by (Schalkwijk et al., 2015a):

$$\underbrace{\frac{\partial\tilde{\vec{u}}}{\partial t}}_{\text{rate of change}} = -\underbrace{\frac{1}{\rho_0}\vec{\nabla}\cdot(\rho_0\tilde{\vec{u}}\tilde{\vec{u}})}_{\text{resolved}} - \underbrace{\frac{1}{\rho_0}\vec{\nabla}\cdot(\rho_0\widetilde{\vec{u}_{\text{sg}}\vec{u}_{\text{sg}}})}_{\text{sub-grid}}$$

$$-\underbrace{w^{\text{LS}}\frac{\partial\tilde{\vec{u}}_h}{\partial z}}_{\text{subsidence}} - \underbrace{\vec{u}_h^{\text{LS}}\cdot\vec{\nabla}_h\vec{u}^{\text{LS}}}_{\text{large-scale advection}}$$

$$+\underbrace{\frac{1}{\tau}\left(\vec{u}_h^{\text{LS}} - \langle\vec{u}_h\rangle\right)}_{\text{nudging}} + \underbrace{\vec{F}_{\vec{u}}}_{\text{sources}} \tag{2.11}$$

$$-\underbrace{2\vec{\Omega}\times(\tilde{\vec{u}} - \vec{u}_g^{\text{LS}})}_{\text{Coriolis \& large-scale pressure}}$$

$$-\underbrace{\vec{\nabla}\pi}_{\text{modified pressure}} - \underbrace{\frac{\tilde{\theta}_v - \langle\theta_v\rangle}{\langle\theta_v\rangle}g\hat{k}}_{\text{buoyancy}}.$$

The first six terms in equation 2.11 are analogous to equation 2.6, but pressure fluctuations, buoyancy effects and the rotation of the Earth are now also included. Here $\vec{u}_g^{\text{LS}}$ is the geostrophic wind velocity vector, again according to ECMWF. The virtual potential temperature is denoted with θ_v, g is the gravitational acceleration and π is a modified pressure term. The virtual potential temperature is a measure of buoyancy and may be calculated as

$$\theta_v \approx \left(\theta_l + \frac{L}{c_{pd}\Pi}q_c\right)\left(1 - \left(1 - \frac{R_v}{R_d}\right)q_t - \frac{R_v}{R_d}q_c\right), \tag{2.12}$$

where $R_v = 461.5$ J/(kg·K) is the specific gas constant for water vapor.

2.4 Earth's radiation budget

Solar radiation is the primary source of energy entering Earth's atmosphere, driving the weather and climate system. In approximation, the Sun may be considered as a black body emitting black-body radiation. This radiation is electromagnetic radiation generated by the thermal motion of particles, and its spectrum is determined solely by the body's temperature. With a temperature of $T_S \approx 5800$ K, the Sun emits radiation across a wide range of the electromagnetic spectrum, with the majority of its energy in the ultraviolet (UV), visible, and near infra-red (IR).

Upon reaching the Earth's system, solar radiation first travels through Earth's atmosphere where it interacts with matter through absorption, emission and scattering. Figure 2.1 displays a simplified schematic view of the mean global radiation balance. In the top middle, incoming solar radiation enters the system. Part of the solar radiation is reflected back into space by the atmosphere. Another part is absorbed by the atmosphere, which heats up as a result. Of
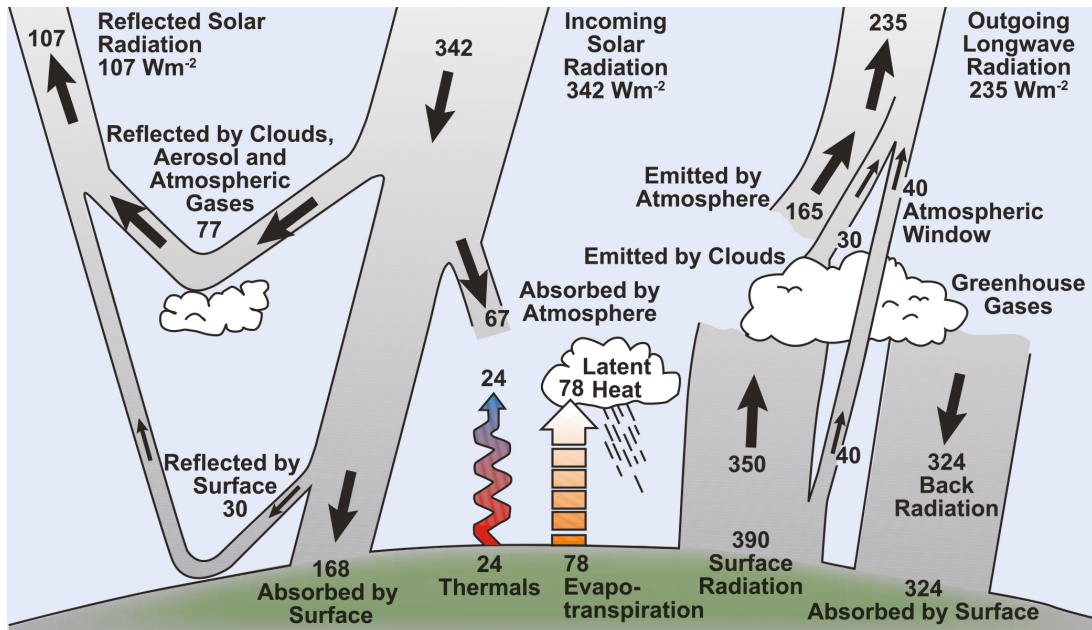
Figure 2.1: Schematic diagram of Earth's annual and global mean energy balance, showing the average fluxes of short-wave (left) and long-wave (right) radiation in the atmosphere. Adapted from Solomon (2007).

the solar radiation that reaches the bottom of the atmosphere (direct as well as diffuse), yet another part is reflected by Earth's surface. The remaining energy is absorbed by the surface, which also heats up as a result.

Like the Sun, the Earth is (in simple approximation) assumed to emit thermal radiation like a black body. Since the Earth has a very different body temperature ($T_E \approx 288$ K), the frequency spectrum of thermal radiation emitted by the Earth is also very different from the Sun. This is shown in figure 2.2a. The Earth emits no visible light, and most of the energy is emitted as far infra-red radiation.

When attempting to describe the radiative processes in the atmosphere, it is therefore common to make a distinction of two spectral regions of atmospheric radiation: we use *short-wave* radiation to denote the solar part of the spectrum (or extraterrestrial radiation), and *long-wave* radiation to denote the thermal infra-red part (also called terrestrial radiation) (Thomas and Stamnes, 2002).

Many of the interactions between radiation and matter are frequency-dependent. Since Earth's atmosphere is comprised of matter, it can be seen as a body absorbing and emitting thermal radiation as well. Its temperature (and therefore its emission spectrum) is similar to that of the Earth. Figure 2.2b shows that the gases that make up Earth's atmosphere are relatively transparent for a lot of the short (solar) wavelengths, but absorb the longer (terrestrial) wavelengths emitted by the Earth much better. The short wavelengths are in turn very much affected by the presence of clouds, since clouds reflect a significant amount of solar radiation. This distinction between short- and long-wave radiation is therefore very important.

The processes that affect the propagation of electromagnetic radiation through a medium are described by radiative transfer theory. The following section will contemplate on this phenomenon in slightly more detail, and the subsequent section will describe how radiative transfer is implemented in GRASP.
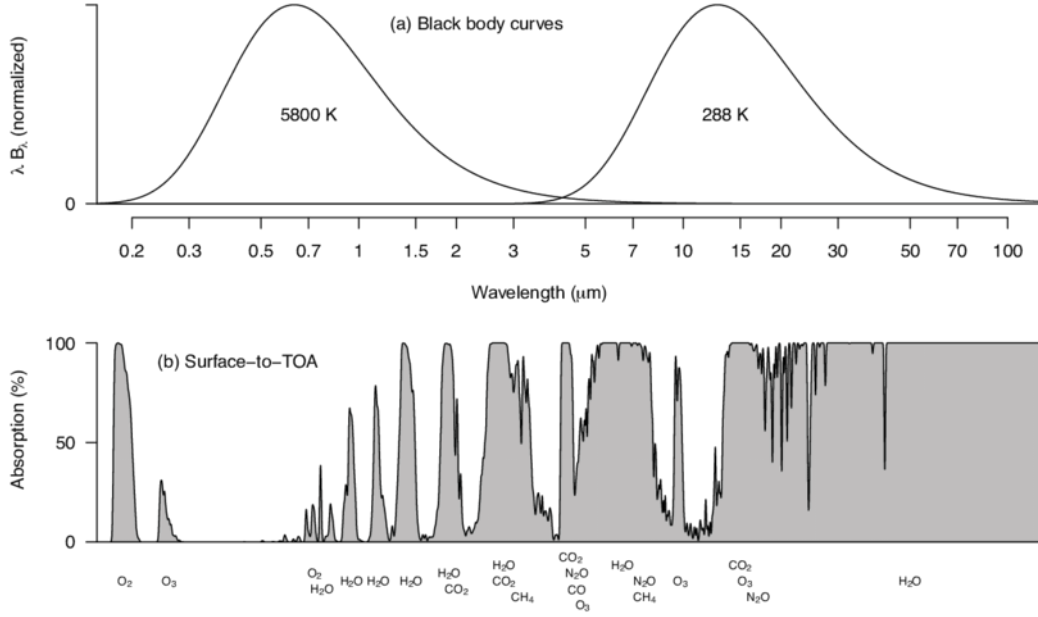
Figure 2.2: (a) Black body emission spectra for the Sun (on the left) and the Earth (on the right). Notice that the curves are normalized; in reality the intensity of terrestrial radiation is much lower than solar radiation. (b) The absorption spectrum of Earth's atmosphere from the surface to the top of the atmosphere (TOA). Adapted from Goody and Yung (1989).

2.5 Radiative transfer theory

In basic terms, the radiative transfer equation states that a beam of electromagnetic radiation gains energy by emission, loses energy to absorption and redistributes energy over different frequencies by scattering. The rate of change of the spectral radiance I_v (or more simply, the intensity at a specified frequency v) when traveling over a distance ds is then characterized by the mediums density ρ, absorption coefficient κ_v and emission coefficient j_v (Chandrasekhar, 1950, p. 9):

$$\frac{dI_v}{ds} = -\kappa_v \rho I_v + j_v \rho. \tag{2.13}$$

The ratio of the emission coefficient to the absorption coefficient plays an important role in radiation theory, and is called the source function $\mathcal{J}_v$:

$$\mathcal{J}_v \equiv \frac{j_v}{\kappa_v}. \tag{2.14}$$

We can then write equation 2.13 in terms of the source function $\mathcal{J}_v$:

$$-\frac{dI_v}{\kappa_v \rho ds} = I_v - \mathcal{J}_v. \tag{2.15}$$

This equation is known as the radiative transfer equation. A formal solution arises in the form of (Chandrasekhar, 1950)

$$I_v(s) = I_v(0) \cdot e^{-\tau_v(s,0)} + \int_0^s \mathcal{J}_v(s') e^{-\tau_v(s,s')} \kappa_v \rho ds', \tag{2.16}$$

where $\tau_v(s, s')$ is the optical thickness of the material for a specific frequency v between the points s and s':

$$\tau_v(s, s') = \int_{s'}^s \kappa_v \rho ds. \tag{2.17}$$

The first part of the right hand side of equation 2.16 describes the part of intensity that enters the domain at $s = 0$, accounting for absorption with a factor $e^{-\tau_v}$. The second part describes the intensity that results from emission at all points inside the domain, also reduced with absorption.

One of the major challenges in accurate calculation of atmospheric radiative transfer arises from the frequency-dependency of the interactions between radiation and matter. Even over narrow ranges, a small change in frequency can completely change the absorption coefficient κ_v. This makes the evaluation of the integrals in equation 2.16 computationally very expensive.

The waveband method is a possible approach to this challenge (see Rodgers, 1968, for example). Here, the spectrum is divided into a pre-specified set of wavelength intervals (wavebands), for which an average absorption coefficient is calculated. Another (more recent) approach is called 'the correlated k-distribution method' (Fu and Liou, 1992, Kato et al., 1999). This method uses a distribution function of the absorption coefficients for a given wavelength interval to estimate the average absorption for that interval, and then treats the wavelengths at which absorption is equally strong as one 'monochromatic' wavelength.

2.6 Radiative transfer modeling

In any NWP model, an atmospheric radiative transfer model is needed to calculate the transfer of radiative energy throughout Earth's atmosphere. An example of such a model is the Rapid Radiative Transfer Model (RRTM, Mlawer et al., 1997). This is a validated approach for the calculation of short-wave and long-wave radiative fluxes and heating rates. The method adopted in GRASP is called the RRTM for GCMs (RRTM-G), an accelerated version of RRTM. The same radiative transfer model is employed in ECMWF's IFS.

The physics that describes atmospheric radiative transfer is generally well understood (Pincus et al., 2005). However, because computing the solutions of the radiative transfer equations is computationally so very expensive, the challenge with radiation is primarily to find a balance between computational cost and accuracy (Pincus and Stevens, 2013). One approach for reducing computational cost is to prescribe forcings such as radiative heating profiles (e.g. Siebesma et al., 2003). This approach is very useful in academic cases where radiation is already known and drives the flow indirectly. However, the detachment between radiation and the state of the atmosphere in the simulation renders the study of interactive feedback loops between the clouds and radiation impossible.

Another approach is to perform radiative calculations on a reduced spatial grid and/or on a reduced temporal frequency. The results are then afterwards interpolated back to the original grid, using the solar zenith angle for a more accurate interpolation of the short-wave fluxes.

The RRTM-G scheme uses the surface albedo and the vertical profiles of temperature, pressure, density, humidity, cloud cover and ozone up to the top of the atmosphere for its calculations. The method uses the Monte Carlo Independent Column Approximation (McICA) of Pincus et al. (2003). McICA uses Monte Carlo sampling to simulate a realistic cloud state simultaneous with spectral interval integration.

We previously noted the importance of distinguishing between short- and long-wave radiation. For the same reasons as mentioned before, these two frequency bands are evaluated separately in RRTM-G. For the remainder of this thesis, a radiative flux F will be denoted S in the case of a short-wave flux, and L in the case of a long-wave flux. In addition, a superscripted arrow will indicate the direction of the flux with respect to Earth's surface. All radiation is considered only in one dimension, going either up or down. The net flux is defined as the difference between downward and upward fluxes, defining fluxes propagating towards the Earth as positive.

$$F^{\text{net}} \equiv F^{\downarrow} - F^{\uparrow}. \tag{2.18}$$

A subscript is used to identify the vertical level at which the flux is considered: F_{t} indicates a flux at the top of the atmosphere, and F_{b} indicates a flux at the bottom of the atmosphere (thus reaching Earth's surface). Unless stated otherwise, all radiative fluxes in this thesis pass through a flat, horizontal plane and have unit W/m^2.

Since this thesis focuses on the effects of solar radiation, a simplified derivation of the transfer equation for down-welling short-wave radiation will be treated here. Equation 2.16 is used as a starting point. There is no emission of short-wave radiation inside the atmosphere, so the second term in equation 2.16 vanishes. We can use:

$$I_v(0) = S_t^\downarrow = S_0 \cdot \cos\theta, \tag{2.19}$$

where $S_t^\downarrow$ denotes the down-welling short-wave radiation at the top of the atmosphere, which can be calculated by multiplication of the solar constant $S_0 \approx 1368$ W/m² (Thomas and Stamnes, 2002) and the cosine of the solar zenith angle θ. The optical thickness for a homogeneous mixed layer can be approximated by (Elterman, 1964):

$$\tau = \alpha l, \tag{2.20}$$

where α is the attenuation coefficient of the medium and l is the length of the path the light travels through that medium. A (very) simple description of the down-welling short-wave radiation that reaches the bottom of the atmosphere ($S_b^\downarrow$) is then:

$$S_b^\downarrow = S_t^\downarrow \cdot e^{-\tau} = S_0 \cdot \cos\theta \cdot e^{-\alpha l}. \tag{2.21}$$

In RRTM-G, the transfer of radiation is not calculated for the entire atmosphere at once. Instead, the transfer of short- and long-wave radiation, both down- and up-welling, is calculated for discrete pressure layers, using the optical properties of that layer. The result is a vertical profile of these fluxes for every radiation time-step.

When the fluxes have been calculated, the vertical flux profiles can be used to compute the heating rates. Consider an arbitrary atmospheric grid cell in GRASP with height Δz. Since we only consider radiation in the vertical direction, the only boundaries of interest are the horizontal surfaces of the grid box, the bottom (at altitude z) and top (at $z + \Delta z$). At these surfaces, the net fluxes are calculated following the convention of equation 2.18:

$$S^{\text{net}}(z) = S^\downarrow(z) - S^\uparrow(z), \tag{2.22}$$

$$L^{\text{net}}(z) = L^\downarrow(z) - L^\uparrow(z). \tag{2.23}$$

Conservation of energy states that the in- and outflow of radiative energy through the boundaries of a volume must equal the heating (or cooling) rate within that volume. For any net radiative surface flux F^{net}, the corresponding heating rate dT/dt (in K/s) can be evaluated using (Hanjalić et al., 2007):

$$\rho c_{pd} \frac{dT}{dt} = \frac{\partial F^{\text{net}}}{\partial z} = \frac{F^{\text{net}}(z + \Delta z) - F^{\text{net}}(z)}{\Delta z}. \tag{2.24}$$

RRTM-G operates on pressure levels (instead of height levels), so to enable compatibility this equation is adjusted using the hydrostatic equation ($dp = -\rho g \, dz$):

$$\frac{dT}{dt} = \frac{1}{\rho c_{pd}} \frac{\partial F^{\text{net}}}{\partial z} = -\frac{g}{c_{pd}} \frac{\partial F^{\text{net}}}{\partial p}. \tag{2.25}$$

In RRTM-G, the short-wave and long-wave heating rates are thus calculated as:

$$\left.\frac{dT}{dt}\right|_S = -\frac{g}{c_{pd}} \frac{S^{\text{net}}(p + \Delta p) - S^{\text{net}}(p)}{\Delta p}, \tag{2.26}$$

$$\left.\frac{dT}{dt}\right|_L = -\frac{g}{c_{pd}} \frac{L^{\text{net}}(p + \Delta p) - L^{\text{net}}(p)}{\Delta p}. \tag{2.27}$$

The total heating rate dT/dt can then easily be calculated as the sum of both components:

$$\frac{dT}{dt} = \left.\frac{dT}{dt}\right|_S + \left.\frac{dT}{dt}\right|_L, \tag{2.28}$$

and this value of dT/dt is then used as the previously mentioned heating rate Q_r that enters GRASP as a source term for the liquid water potential temperature θ_l in equation 2.7.

3

Methods

3.1 Set-up of the simulations

The atmosphere was simulated using the GPU-Resident Atmospheric Simulation Platform (GRASP). The physical equations that formulate the core of this large-eddy simulation (LES) were discussed in chapter 2. In this chapter, the specific configuration of the simulations will be discussed.

3.1.1 Domain

The simulated domain was roughly 10x10 km^2 at equal grid spacings of 80 m in horizontal directions. This domain was placed with the Cabauw experimental site for atmospheric research (CESAR) at its center so we can use the site's observations in validating the simulations. This observational site is located in the western part of the Netherlands (51.971° N, 4.927° E) and is equipped with an extensive set of instruments used to study the atmosphere (Russchenburg et al., 2002).

In the vertical direction, the domain starts at Earth's surface, and the grid spacing increases with height. The lowest grid cells have a height of $\Delta z_0 = 30$ m and each model level k has a height that is larger by a factor of $\alpha = 1.312\%$ than the level $k - 1$ below it:

$$\Delta z_k = \Delta z_0 (1 + \alpha)^k \tag{3.1}$$

This compounded growth ends at roughly $\Delta z = 160$ m at almost 10 km altitude.

3.1.2 Initialization

For this thesis, a simulation was performed for every single day of the year 2016. The simulations are day-ahead forecasts, which means that they are simulations of a certain day that are initialized with the information that was on hands the day before that day. The simulations are forecasts with a duration of 27 hours, starting from 21:00 UTC on the day before the day of interest. The initial conditions of $\{u, v, \theta_l, q_t\}$ at 21:00 UTC are obtained from $\{u^E, v^E, T^E, p^E, q_v^E, q_l^E, q_i^E\}$ from the large-scale forecast. The high-resolution (HRES) version of the Integrated Forecasting System (IFS) from the European Centre for Medium-Range Weather Forecasts (ECMWF) was used to this end (specifics will be discussed in section 3.2.1). This forecast uses 4D-Var data assimilation techniques to derive the state of the atmosphere at 00:00 UTC, from which it starts a 10-day forecast. These ECMWF-fields are first linearly interpolated to GRASP's space-time grid after which they are converted to the prognostic

GRASP variables using:

$$u = u^E,$$
$$\tag{3.2}$$

$$v = v^E,$$
$$\tag{3.3}$$

$$q_t = q_v^E + q_l^E + q_i^E,$$
$$\tag{3.4}$$

$$\theta_l = \frac{T^E}{\Pi} - \frac{L}{c_{pd}\Pi}q_c,$$
$$\tag{3.5}$$

with

$$\Pi = \left(\frac{p^E}{p_{\text{ref}}}\right)^{R_d/c_{pd}}.$$
$$\tag{3.6}$$

3.1.3 Coupling to a general circulation model

As mentioned earlier, a larger (general circulation) model is required to provide large-scale advective scalar transport, geostrophic wind and large-scale subsidence to the LES. To this end we used the same model as was used for initialization: the HRES IFS forecast by ECMWF.

The domain of GRASP extends to about 10 km in the vertical direction. For accurate calculation of radiative transfer, the upper part of the atmosphere must also be accounted for. This was achieved by stacking the vertical profiles of humidity and temperature from ECMWF IFS (which extend to the top of the atmosphere) on top of the GRASP profiles. To prevent discontinuities, the term that controls the amount of nudging (τ in equation 2.5 and 2.11) is designed as such that the amount of nudging of the atmospheric fields in GRASP towards IFS increases with height z.

Finally, it is important to note that ozone is currently not included in GRASP. The chemical processes that produce and destroy ozone mainly take place above the domain of the LES, impeding the need to include those in the simulation. Since this trace gas has effects on radiation that should not be neglected, ECMWF's values of the ozone mass mixing ratio are used to calculate radiative transfer across the entire atmosphere.

3.1.4 Implementation of cloud-radiation feedback

To study the interaction between radiation and the state of the atmosphere, the module that calculates the radiative transfer (RRTM-G) was used in two different configurations. One setting applied prescribed radiative tendencies, which were calculated ahead of the simulation using the state of the atmosphere as forecasted by a large-scale NWP model. We again used ECMWF IFS for this purpose, the same large-scale model used to account for other processes in our simulations. For the remainder of this thesis, we shall refer to this configuration as GRASP with prescribed radiation, or GRASP-P in short.

The other configuration calculated the radiative tendencies interactively, using the actual thermodynamic state of GRASP to evaluate radiative transfer. This way, the effects of the resulting heating rates on the state of the atmosphere influence the subsequent calculations of radiative transfer, thus enabling interaction between clouds and radiation. This configuration will henceforth be referred to as GRASP with interactive radiation, or GRASP-I in short.

The resulting output of both configurations was analyzed and compared to one another. We will now discuss both modes in more detail to ensure proper understanding of their differences.

Figure 3.1 displays a simplified schematic overview of GRASP-P. GRASP is responsible for solving the governing equations that were discussed in section 2.3. The initial conditions to these differential equations (e.g. the state of the atmosphere at the start of every simulation) are provided by the most recent HRES IFS forecast by ECMWF. The IFS forecast also provides the terms for large-scale subsidence, large-scale advection, nudging and large-scale pressure systems.

GRASP also needs information on the radiative forcings, which are prescribed using RRTM-G on the basis of IFS ahead of the main simulation. RRTM-G needs vertical profiles of temperature, humidity, pressure, density, horizontal wind speed, cloud cover and ozone up to the top of the atmosphere. In the figure, all these variables are summarized as 'thermodynamic state'. RRTM-G thus uses the thermodynamic state of the atmosphere as forecasted by IFS to calculate the heating rates and the surface fluxes, which are then applied as radiative forcings in GRASP. RRTM-G is employed a second time to calculate the heating rates and the surface fluxes on the basis of the state of the atmosphere in GRASP.
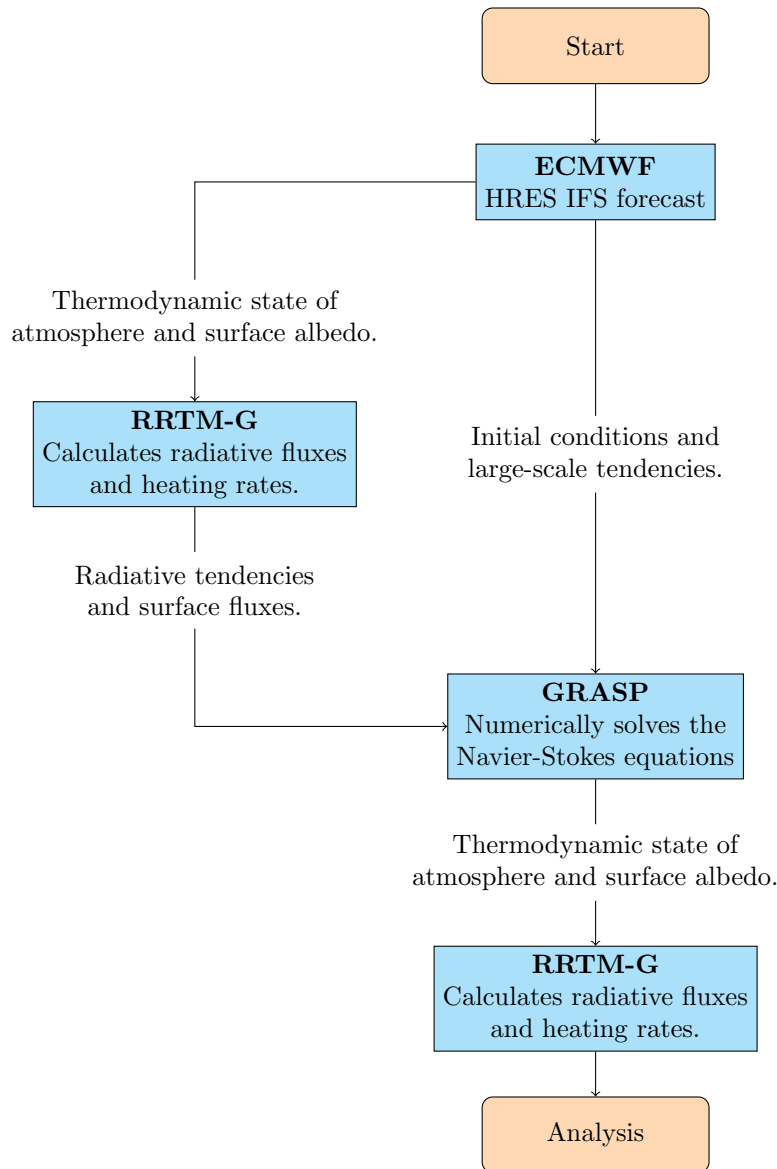
Figure 3.1: Simplified schematic diagram of GRASP running in the prescribed radiation configuration (GRASP-P).

Figure 3.2 displays a schematic overview of GRASP-I. The simulation is almost identical to GRASP-P, with the only exception being the calculation of the radiative tendencies that are applied to the model. The difference is that GRASP now uses the radiative tendencies that are calculated based on its own thermodynamic state to evaluate the equations of motion. This configuration therefore enables the development of cloud-radiative feedback loops. The top of the domain of GRASP lies at an altitude of $z = 10$ km. Information about the part of the atmosphere above GRASP's domain was still provided to RRTM-G by the IFS forecast.
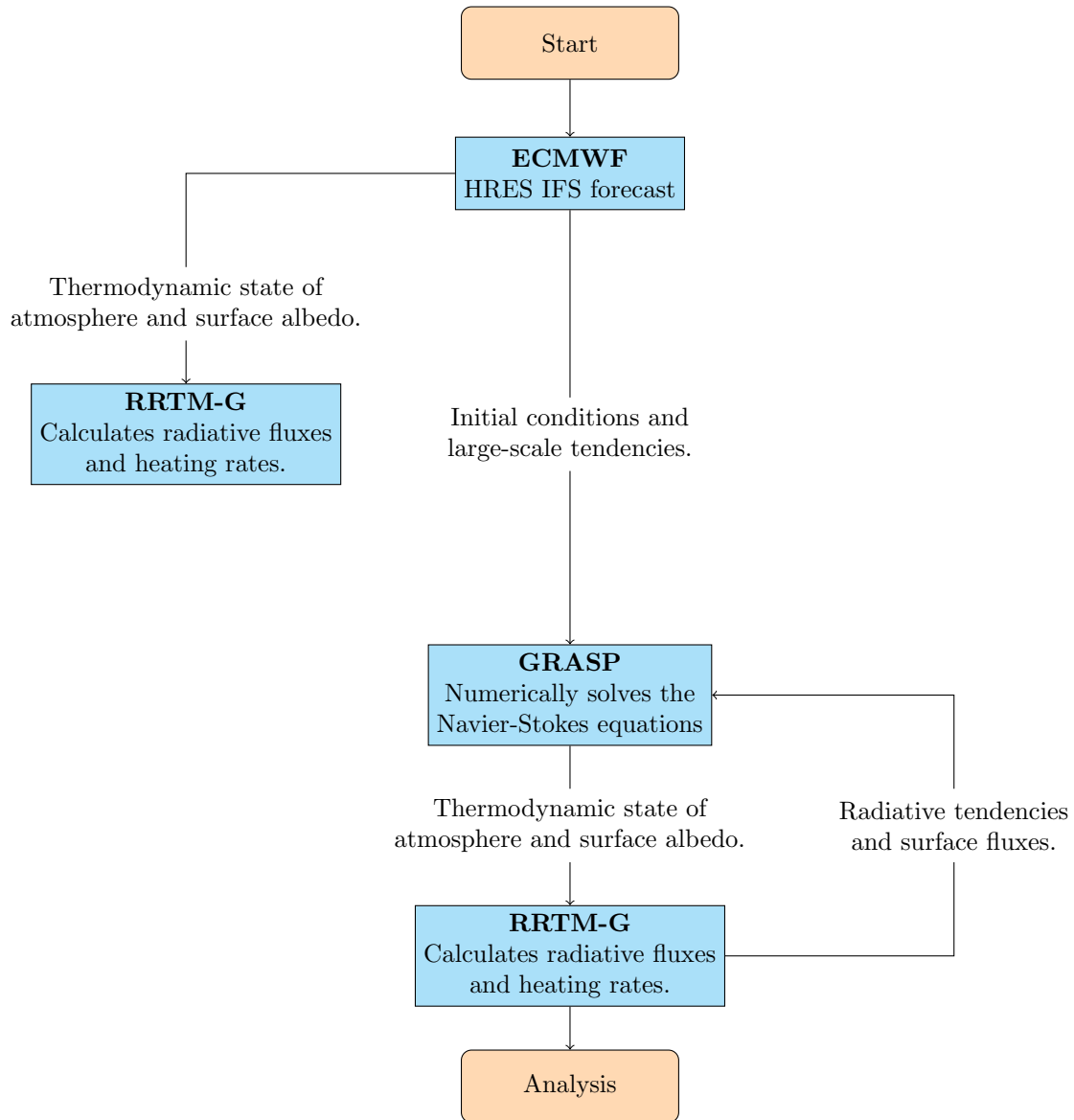
Figure 3.2: Simplified schematic diagram of GRASP running in the interactive radiation configuration (GRASP-I).

3.2 Data

Multiple datasets were used in this study. For the remainder of this thesis, we will often refer to a particular dataset using its designated short name as depicted in table 3.1. In this section, all datasets will be described and their important characteristics will be discussed. The data processing steps that need to be taken to reproduce the results are also listed here.

3.2.1 Data description

The Integrated Forecasting System (IFS) is a global circulation model (GCM) that is developed and maintained by both the European Centre for Medium-Range Weather Forecasts (ECMWF) and Météo-France. It is one of the prevailing GCMs used worldwide and was the first operational NWP model that utilized 4D-Var data assimilation (Andersson and Thépaut, 2008). ECMWF runs the IFS in a number of different configurations, of which we use the operational medium-range forecast with the highest spatial resolution (denoted 'HRES' by ECMWF, previously denoted 'deterministic atmospheric model'). This configuration runs at a horizontal resolution of ~ 9 km and has 137 vertical levels, from the surface up to 0.01 hPa (which is around 80 km). The model runs every twelve hours out to ten days, and uses the most accurate estimate of the current conditions for its initialization. We used the runs that are based at 00:00 UTC to compile the yearly dataset, since these are the same runs that were used to initialize GRASP. Note that, even though there are many variations of IFS, this particular configuration of IFS is the one that is referred to when we simply discuss 'IFS' in this thesis.

We have studied two configurations of the GRASP model, one with prescribed radiation (GRASP-P) and one with interactive radiation (GRASP-I). The difference between these two models is described in section 3.1.4. Apart from these differences, both models share the same characteristics. They are both large-eddy simulations of 27 hours, initialized at 21:00 UTC using the most recent 00:00 UTC IFS medium-range forecast described above. Both have the same spatial grid of 80 m horizontal resolution and 128 vertical levels up to approximately 10 km, and the temporal output resolution has been set to 5 minutes.

ERA5 is the fifth generation of a global climate reanalysis dataset produced by ECMWF. It also employs the IFS (cycle CY41R2) and its 4D-Var data assimilation. Again, some variations of ERA5 are available. Here we have used the high resolution realization as well, which consists of analyses and short forecasts of 18 hours at hourly resolution, initialized twice a day from the analyses at 06:00 and 18:00 UTC. This configuration runs at a horizontal resolution of 31 km and has 137 vertical levels, from the surface up to 0.01 hPa. For further details, see Hersbach and Dee (2016).

The final dataset used for this study is the Baseline Surface Radiation Network (BSRN). This is a project of the the World Climate Research Programme (WCRP) and the Global Energy and Water Experiment (GEWEX) and was designated as the global baseline network for surface radiation for the Global Climate Observing System (GCOS) in 2004. The project features high time resolution measurements of key quantities related to surface radiation in different climatic zones around the world. There are about 40 stations worldwide currently, one of which is located at the Cabauw experimental site for atmospheric research (CESAR). This observational supersite, located in the western part of the Netherlands (51.971° N, 4.927° E), is the centerpiece of atmospheric research in the Netherlands. Among the measured quantities, global irradiance (W/m^2) is available at a temporal resolution of 1 minute, which is the quantity that was used to validate down-welling short-wave radiation. For further details about the Cabauw BSRN station, see Knap et al. (2010).
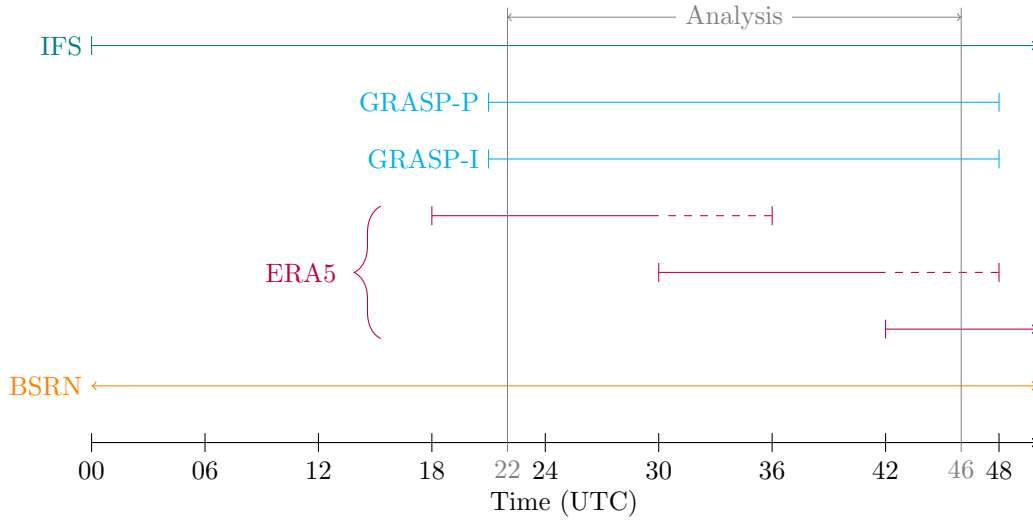
Figure 3.3: Overview of all datasets used in this study with respect to time. The window for the analysis has been chosen so it ranges exactly from midnight to midnight in Central European Summer Time (CEST) which ensures that the $S_b^\downarrow$ is always zero at the borders of the window. Such a window was singled out of the datasets for every day in 2016, and on

Table 3.1: Summary of data sources used in this study

Short name	Description
IFS	ECMWF's operational medium-range forecast
ERA5	Fifth generation of ECMWF's atmospheric reanalysis forecast
GRASP-P	GRASP forecast with prescribed radiation
GRASP-I	GRASP forecast with interactive radiation
BSRN	Surface radiation observations

3.2.2 Data processing

For the statistical part of this study, these datasets are processed to form inter-comparable continuous datasets at the same temporal resolution for the entire year of 2016. As recommended by Roesch et al. (2011), a strict quality check on all datasets (BSRN in particular) has been applied, discarding all data entries during night time and values beyond physical possible limits (such as negative $S_b^\downarrow$, or $S_b^\downarrow$ higher than the irradiation at the top of the atmosphere).

After this cleaning procedure, all datasets are temporally aggregated to generate comparable time windows of radiation. This procedure is very important, since it directly impacts the results of the statistical validation study (Boilley et al., 2016). Radiation values are collected and averaged in bins of 3 hours, because that is the highest temporal resolution at which we have at least one data entry of every dataset. If less than 75% of the possible slots are available to synthesize the mean radiation, the entire bin was discarded. This selection is restrictive, but it ensures that sampling errors are kept as low as possible. This is especially important for time windows containing sunrises or sunsets, where a less radical selection can lead to erroneous results.

4

Results

4.1 Dynamic effects of cloud-radiation feedback

The goal of this section of the results is to qualitatively assess the changes that were observed in the thermodynamics of the simulations after implementing the interactive radiation configuration. Two-dimensional visualizations of every day-ahead forecast in 2016 were created for a series of variables for both GRASP-P and GRASP-I, which were all studied to identify the differences between the two. The vast amount of figures created in this study is far too large to be comprehensively presented here, so a selection was made of figures that display the behavior that is characteristic for the entire set of simulations.

Many of the figures that were used in this section are z, t-diagrams, which might need a little introduction. In these diagrams, the y-axis represents the height z (km) of the simulated domain and the x-axis represents time t (h UTC) throughout the coarse of a day. The value of a particular variable at time t and height z is depicted by color. Using this representation, the development of the vertical profile of a certain variable can be visualized throughout time.

4.1.1 Clouds

As was expected, the implementation of interactive radiation showed impact on the presence of clouds in the atmosphere. In general, clouds in GRASP-I were often observed around the same time and height as in GRASP-P, with extreme deviations being rare. However, the development of the vertical profile of the cloud fraction in time shows dissimilarities. Figure 4.1 shows the z, t-diagrams of the cloud fraction in GRASP-P and GRASP-I for several days that display the differences between GRASP-P and GRASP-I that were widely observed.

One of the main results shown in figure 4.1 is that clouds in GRASP-I are more often rising in height than their counterparts in GRASP-P. Especially for clouds up to ~ 7 km, such as in figure 4.1b and 4.1c, the upwards movement of the cloud fraction in time is clearly visible. The right column (depicting the difference between GRASP-I and GRASP-P) displays that GRASP-I produced a region with clouds where GRASP-P had no clouds, directly above a region where GRASP-P had clouds but GRASP-I had fewer clouds (or none at all).

At heights above approximately 7 km, such as in figure 4.1a and 4.1d, clouds in GRASP-I can be observed to lose cloud fraction at the cloud base as well (again, compared to GRASP-P). However, the region of lesser cloud fraction is not accompanied by a region of higher cloud fraction, as is the case with the lower clouds. In these cases, the cloud just seems to rise and evaporate, perhaps as a consequence of the rising motion.
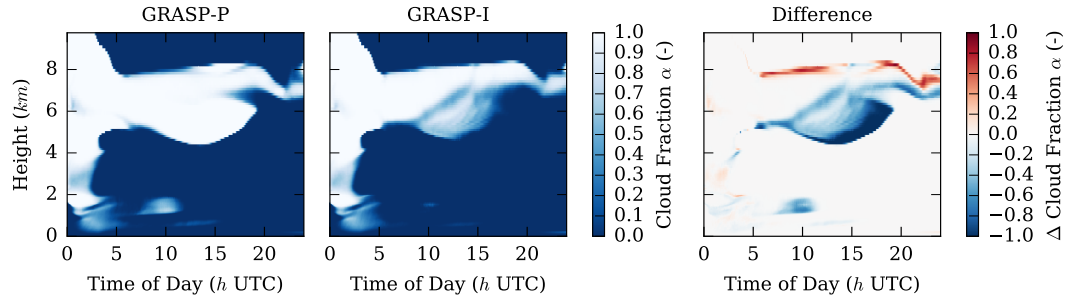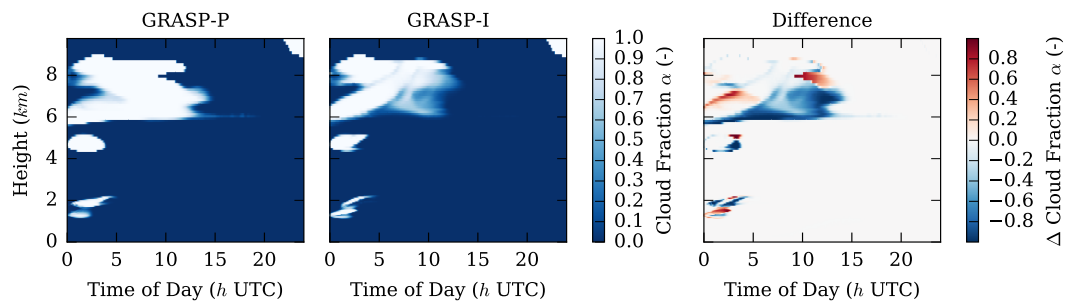
(a) January 10, 2016
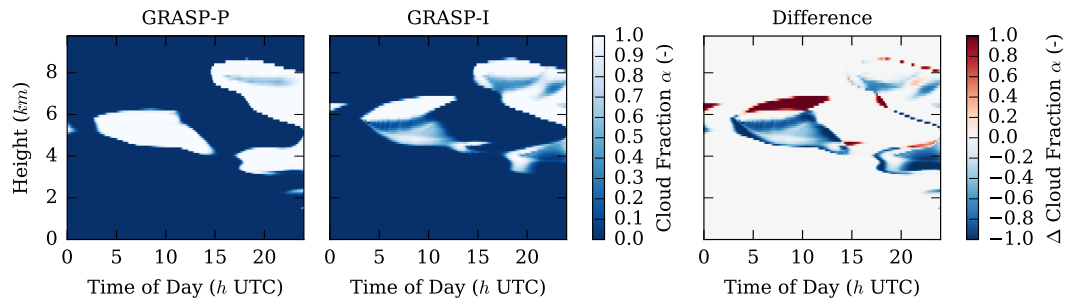
(b) February 13, 2016
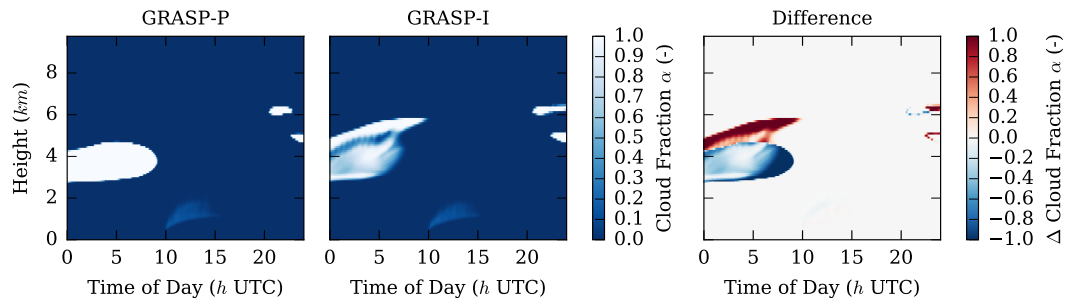
(c) March 7, 2016

(d) March 9, 2016

Figure 4.1: Height-time diagrams of the cloud fraction α at Cabauw (the Netherlands) as predicted by the two GRASP models a day ahead. Several individual days are shown that display the characteristic behavior that was observed in many cases. The model with the prescribed radiation is displayed in the left column, the one with the interactive radiation in the middle column, and the difference between both models, calculated as GRASP-I minus GRASP-P, is shown in the right column.

To analyze the net effect of interactive radiation, a yearly average z,t-diagram of cloud fractions was constructed. Displayed in figure 4.2, these graphs show the average diurnal evolution of the vertical profile of the cloud fraction. The results are as follows.

It appears that the simulations on average create most clouds on altitudes between 0 and 2 km and between 5 and 7 km, and that less clouds are created between 2 and 5 km. Apart from the fringes in the top of the domain, the average diurnal evolution of the vertical profile of the cloud fractions does not exhibit clear correlation in time in both prescribed and interactive cases.

Above 7 km, a periodic pattern shows at intervals of 3 hours. This pattern can be observed in both GRASP-P and GRASP-I, which indicates it is independent of the chosen configuration of radiation. This phenomenon is likely an artifact of the coupling with the ECMWF IFS forecast, which has a temporal resolution of 3 hours. It could possibly result from large-scale forcings or the stronger nudging in the upper part of the domain. This pattern is further discussed in chapter 5. Motivated by the likelihood that the presented clouds above 7 km are artifacts of the simulation, we refrain from drawing conclusions from the results obtained in the upper part of the domain.

The right panel in figure 4.2 shows that the cloud fraction between approximately 5 and 7 km is reduced after introduction of interactive radiation. Another important result is that no clear diurnal pattern is visible in the difference in cloud representation between GRASP-I and GRASP-P. Since short-wave effects should be visible at daytime but absent at night-time, this suggests that the reduction in cloud fraction between 5 and 7 km is a consequence of the long-wave effects of interactive radiation rather than the short-wave effects. The following section will therefore investigate the long-wave heating rates in both simulations.
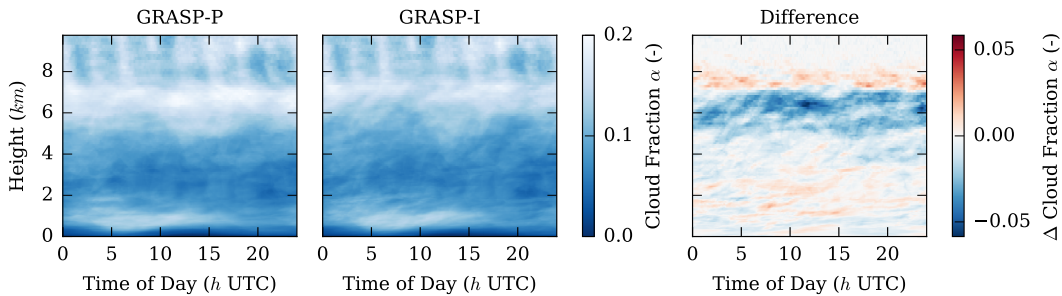

Figure 4.2: Height-time diagrams of the average cloud fraction α at Cabauw (the Netherlands) as predicted by the two GRASP models a day ahead. The model with the prescribed radiation is displayed in the left column, the one with the interactive radiation in the middle column, and the difference between both models, calculated as GRASP-I minus GRASP-P, is shown in the right column. The average diurnal profile was calculated based on individual daily forecasts of every day in 2016.

Figure 4.3 shows the average vertical profiles of the cloud fraction α. On average, GRASP-I and GRASP-P report the same cloud fractions between Earth's surface and 4 km altitude. Between 4 and 7 km however, the cloud fraction is on average lower when interactive radiation is used.
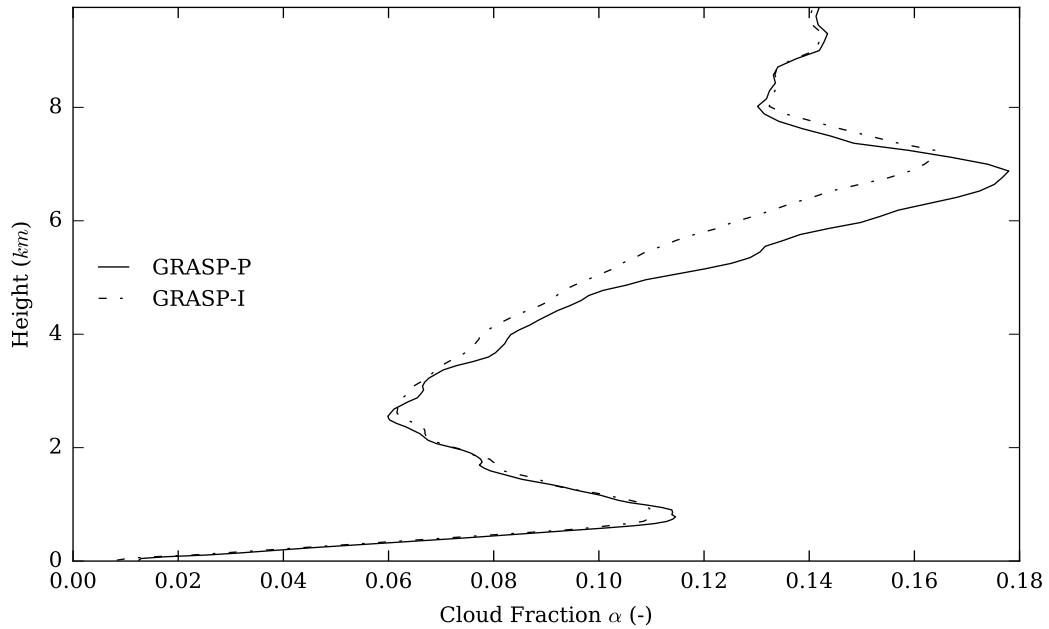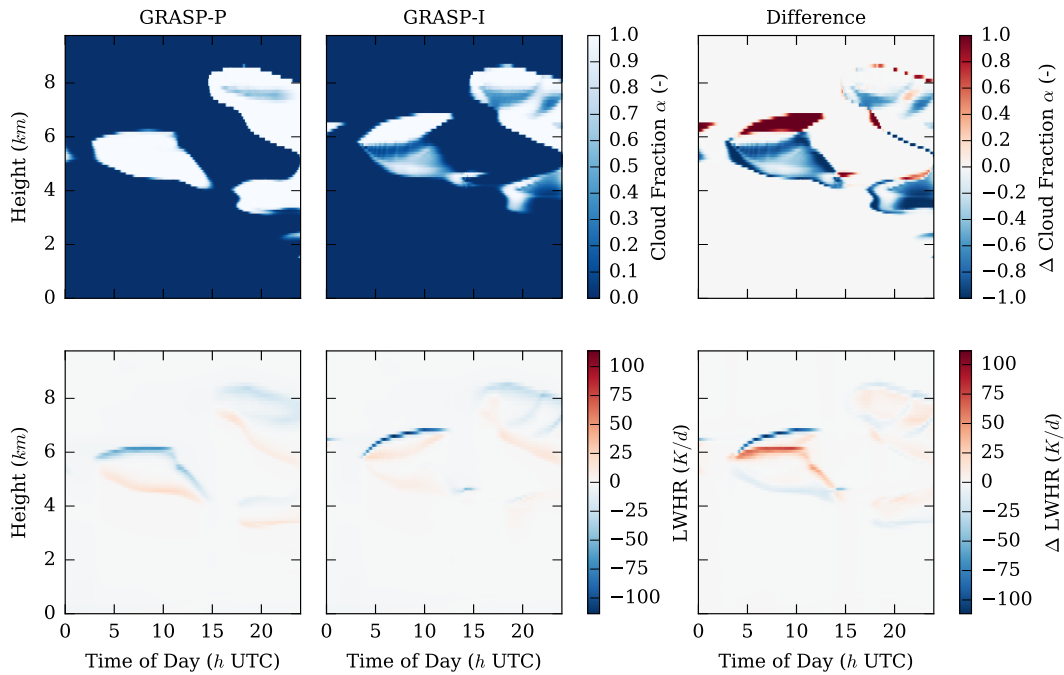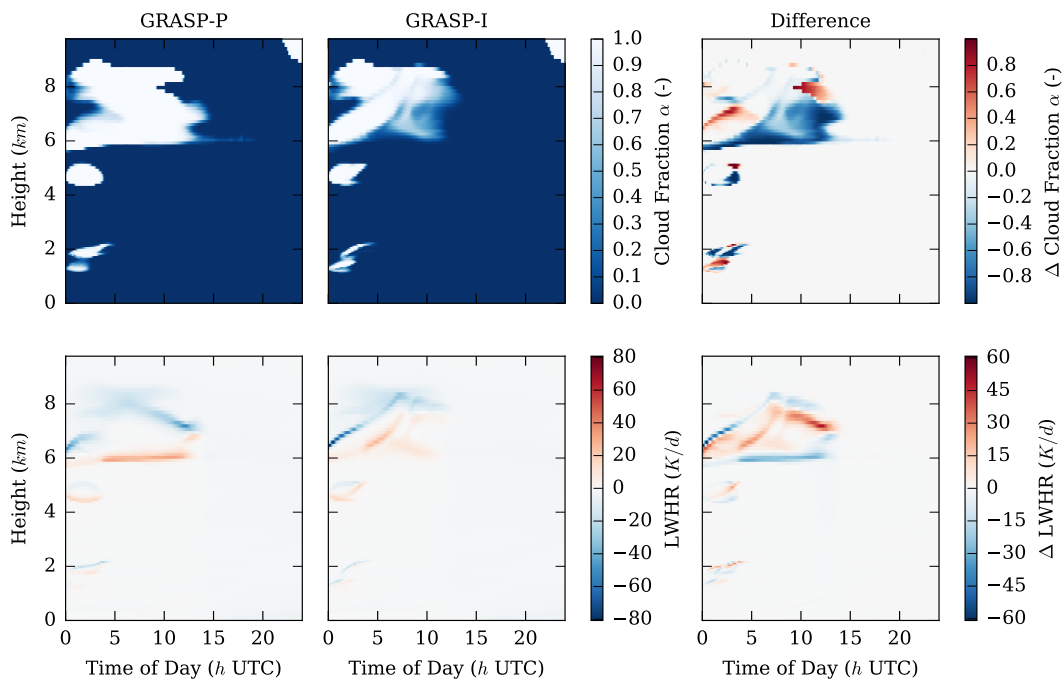

Figure 4.3: Vertical profile of the average cloud fraction α in all day-ahead forecasts by the two GRASP models at Cabauw, the Netherlands. Solid lines represent the model with the prescribed radiation and dotted lines represent the one with the interactive radiation.

4.1.2 Long-wave heating rates

(a) February 13, 2016

(b) March 9, 2016

Figure 4.4: Height-time diagrams of several day-ahead forecasts by the two GRASP models at Cabauw, the Netherlands. The model with the prescribed radiation is displayed in the left column, the one with the interactive radiation in the middle column, and the difference between both models, calculated as GRASP-I minus GRASP-P, is shown in the right column. The first row shows the vertical profile of the cloud fraction α (-) through the course of the day, the second row shows the long-wave heating rate $(dT/dt)_L$ (K/d) likewise.

Figure 4.4 shows the diurnal evolution of the vertical profile of the long-wave heating rate $(dT/dt)_L$ during two of the days that were explored in the previous section. In both GRASP-P and GRASP-I, cloud top radiative cooling in the order of magnitude of several $\sim 10^1$ K/d was applied and radiative heating of the same order of magnitude took place at the bottom of clouds.

In general there does not seem to be a difference in the calculation of long-wave heating rates between GRASP-P and GRASP-I: both models show radiative cooling at the cloud top and radiative heating at the cloud bottom, which is expected behavior. The displacement in the z, t-diagrams of $(dT/dt)_L$ is consistent with the displacement of the clouds. The cloud top radiative cooling is slightly stronger in the case of interactive radiation.
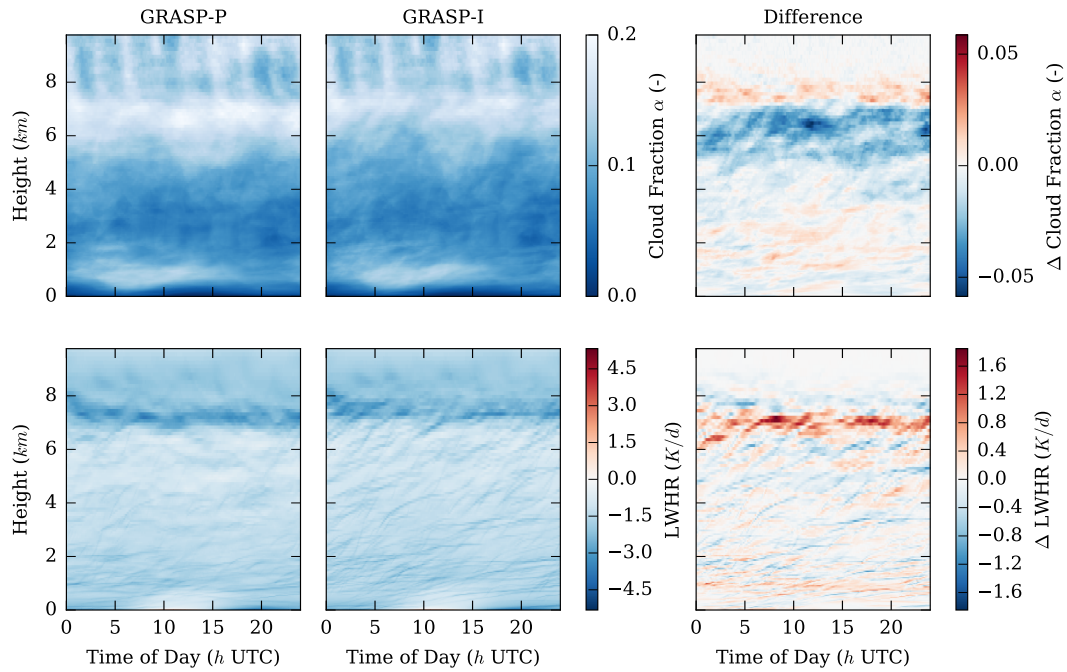
Figure 4.5: The average diurnal cycle of the vertical profiles of the cloud fraction α (-) and the long-wave heating rate $(dT/dt)_L$ (K/d) at Cabauw (the Netherlands) as predicted by the two GRASP models a day ahead. The model with the prescribed radiation is displayed in the left column, the one with the interactive radiation in the middle column, and the difference between both models, calculated as GRASP-I minus GRASP-P, is shown in the right column. The first row shows the vertical profile of α through the course of the day, the second row shows $(dT/dt)_L$. The average diurnal profiles were calculated based on individual daily forecasts of every day in 2016.

An average z, t-diagram was again constructed to assess the net effect of interactive radiation on the long-wave heating radiation. The results are displayed in figure 4.5. On average, both simulations demonstrate a cooling rate of several K/d. The differences between GRASP-P and GRASP-I are small, with the exception of a small region around 7 km altitude, where the cooling rates in GRASP-P are stronger than those in GRASP-I.

Furthermore, figure 4.6 shows the average vertical profiles of $(dT/dt)_L$ (K/d) next to the vertical profiles of the cloud fraction. This graph resonates that the differences between GRASP-P and GRASP-I are small, with the exception around 7 km. From 6 to 7 km altitude, the long-wave heating rate decreases from -1 K/d to almost -3 K/d. In this region, the vertical profile of GRASP-I lies slightly higher than the profile of GRASP-P.
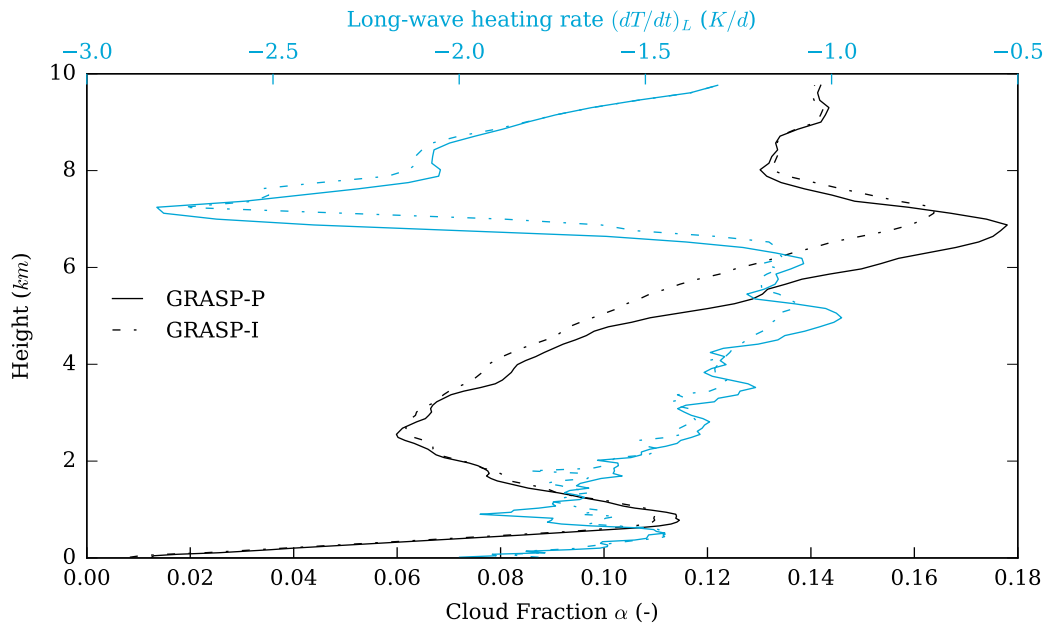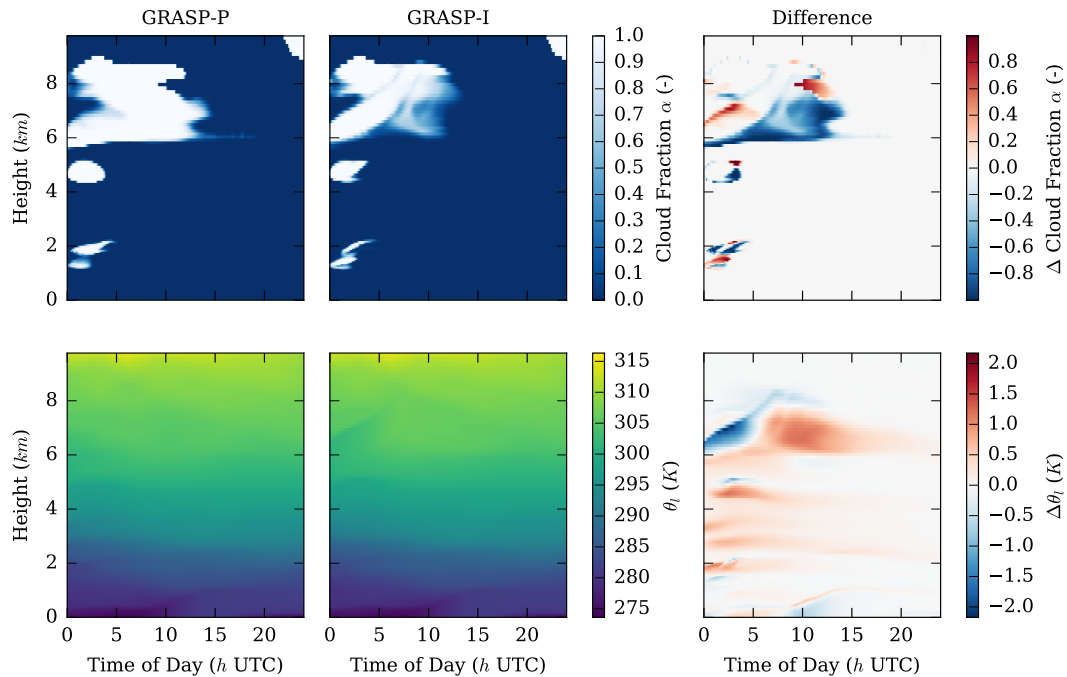

Figure 4.6: Average vertical profiles of all day-ahead forecasts in 2016 by the two GRASP models at Cabauw, the Netherlands. Solid lines represent the model with the prescribed radiation and dotted lines represent the one with the interactive radiation. The vertical profile of the average cloud fraction α is shown in black, the one of the average long-wave heating rate $(dT/dt)_L$ (K/d) is displayed blue.

4.1.3 Liquid water potential temperature
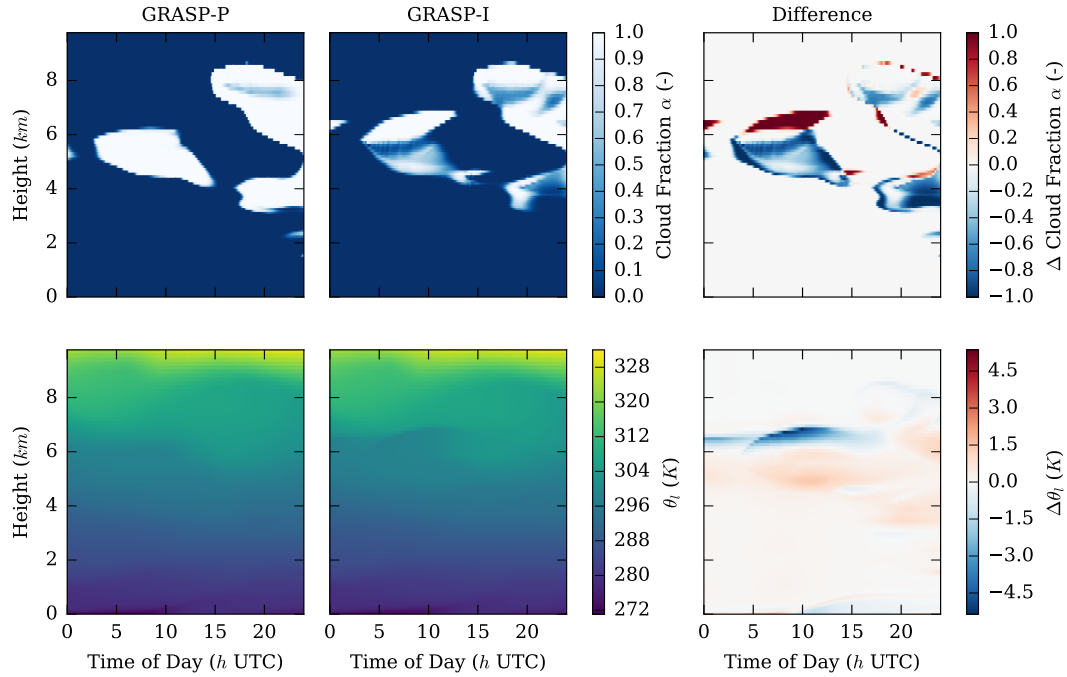
(a) February 13, 2016

(b) March 9, 2016

Figure 4.7: Height-time diagrams of several day-ahead forecasts by the two GRASP models at Cabauw, the Netherlands. The model with the prescribed radiation is displayed in the left column, the one with the interactive radiation in the middle column, and the difference between both models, calculated as GRASP-I minus GRASP-P, is shown in the right column. The first row shows the vertical profile of the cloud fraction α (-) through the course of the day, the second row shows the liquid water potential temperature θ_l (K).

Figure 4.7 shows the diurnal evolution of the vertical profile of the liquid water potential temperature θ_l during the same two days that were highlighted in the previous sections. It can be observed that in both GRASP models θ_l increases with height, and differences between models are visible where cloud representations differ.

In the panels on the right in both figure 4.7a and 4.7b, the effects of interactive radiation are visible. Where and when clouds are rising in GRASP-I, the increase in cloud fraction at a higher altitude is associated with colder air. Underneath that region, where there are less clouds in GRASP-I compared to GRASP-P, an increase in θ_l was observed.

These results are in accordance with the preceding results. Remember from the previous section that radiative heating occurs at the bottom of clouds, and radiative cooling occurs at the top of clouds. Because the clouds are rising in GRASP-I, we observed that the heating associated with clouds are located higher in GRASP-I than in GRASP-P. The results in figure 4.7 resonate this finding, showing that GRASP-I contains cooler regions above warmer regions compared to GRASP-P. In the GRASP-I simulation of March 9, where cloud breakup as a consequence of the rising movement of the cloud was observed, figure 4.7b shows that the region that is vacated by clouds is warmed up. This region then continues to remain warmer for several hours, even after the same cloud in GRASP-P also disappeared. This could be the result of the dryer atmosphere, the displaced heating rates, or a combination of both.
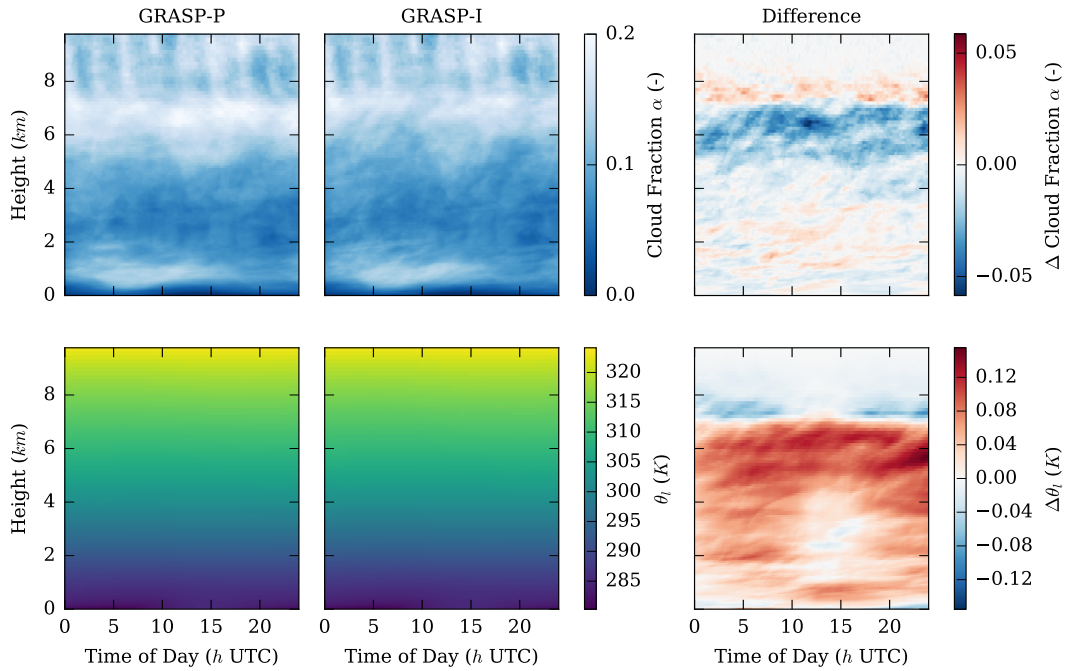

Figure 4.8: The average diurnal cycle of the vertical profiles of the cloud fraction α (-) and the liquid water potential temperature θ_l (K) at Cabauw (the Netherlands) as predicted by the two GRASP models a day ahead. The model with the prescribed radiation is displayed in the left column, the one with the interactive radiation in the middle column, and the difference between both models, calculated as GRASP-I minus GRASP-P, is shown in the right column. The first row shows the vertical profile of α through the course of the day, the second row shows θ_l. The average diurnal profiles were calculated based on individual daily forecasts of every day in 2016.

An average z, t-diagram was constructed to assess the net effect of interactive radiation on the liquid water potential temperature. The results are displayed in figure 4.8. On average, the differences between GRASP-P and GRASP-I are small. Both simulations show that θ_l is mainly dependent on height and ranges on average from 280 K at Earth's surface to 325 K at 10 km altitude. GRASP-I is slightly warmer than GRASP-P, most notably between 5 and 7 km where there temperature difference is about 0.1 K. Figure 4.9 shows the average vertical profiles of θ_l along with the average vertical profiles of the cloud fraction, which confirms that the temperature difference between GRASP-P and GRASP-I is very small.
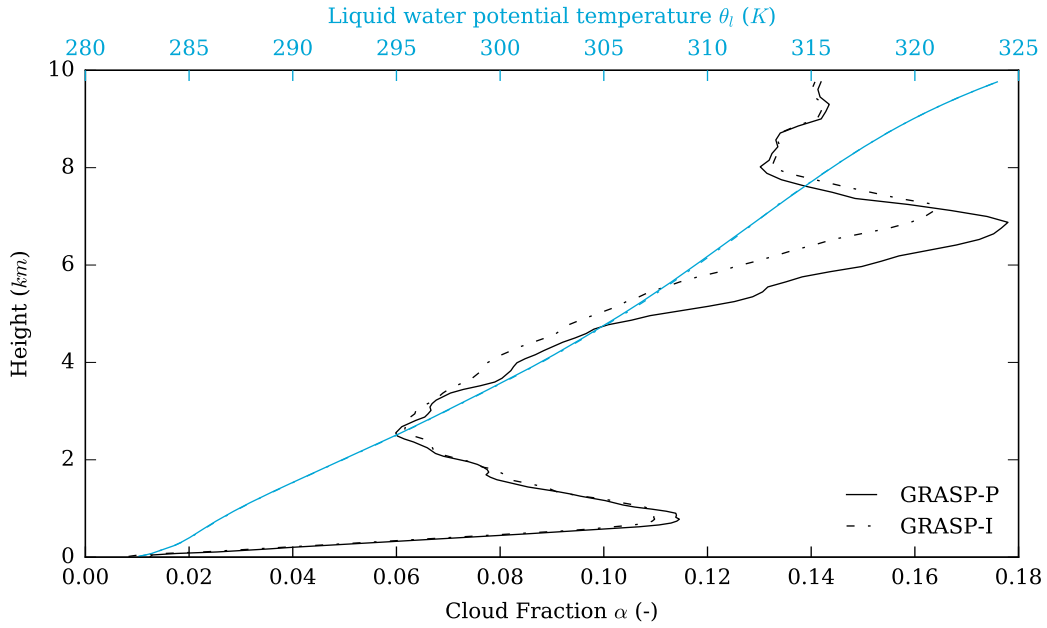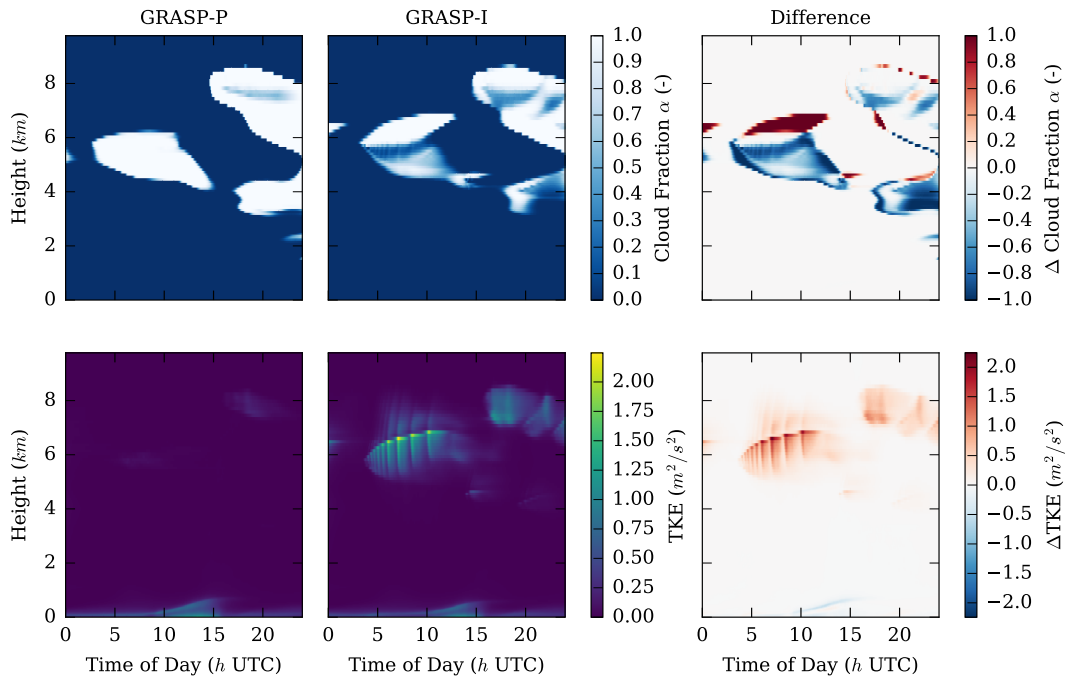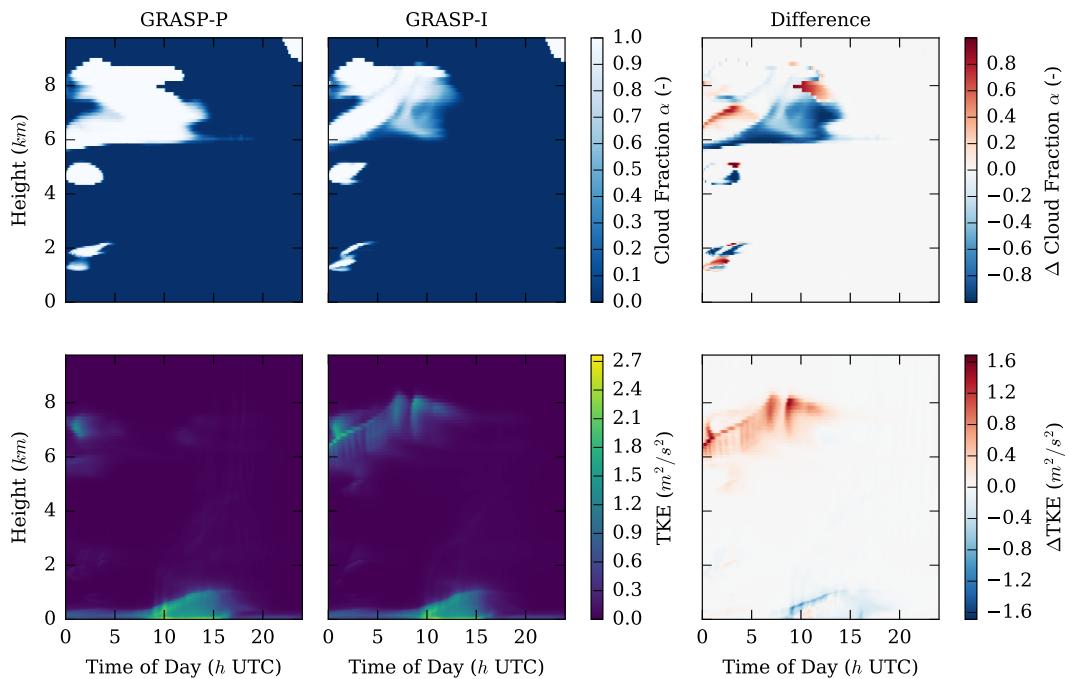

Figure 4.9: The average vertical profile of all day-ahead forecasts in 2016 by the two GRASP models at Cabauw, the Netherlands. Solid lines represent the model with the prescribed radiation and dotted lines represent the one with the interactive radiation. The average vertical profile of the cloud fraction α is shown in black, the one of the liquid water potential temperature θ_l (K) is displayed blue.

4.1.4 Turbulence

(a) February 13, 2016

(b) March 9, 2016

Figure 4.10: Height-time diagrams of several day-ahead forecasts by the two GRASP models at Cabauw, the Netherlands. The model with the prescribed radiation is displayed in the left column, the one with the interactive radiation in the middle column, and the difference between both models, calculated as GRASP-I minus GRASP-P, is shown in the right column. The first row shows the vertical profile of the cloud fraction α (-) through the course of the day, the second row shows the turbulence kinetic energy (TKE, m^2/s^2) likewise.

We investigated the effects of interactive radiation on the turbulence in the atmosphere. This was done by creating z,t-diagrams for the turbulence kinetic energy (TKE, m^2/s^2), calculated as

$$\text{TKE} = \frac{1}{2}\left(\overline{(u')^2} + \overline{(v')^2} + \overline{(w')^2}\right). \tag{4.1}$$

Here u', v' and w' denote the fluctuating (turbulent) parts of u, v and w using Reynolds decomposition ($u' = u - \langle u \rangle$). The results are displayed in figure 4.10. In both models, the turbulence in the planetary boundary layer builds up throughout the course of the day. This turbulence is related to convective instabilities driven by radiative heating of Earth's surface by the Sun.

A prominent effect of interactive radiation can be observed where and when the rising movement of clouds is occurring in GRASP-I. Figure 4.10 shows that these regions are associated with increased TKE. The difference with GRASP-P is substantial in these cases, with GRASP-I usually reporting TKE up to 2 m^2/s^2 in regions where GRASP-P is relatively non-turbulent.

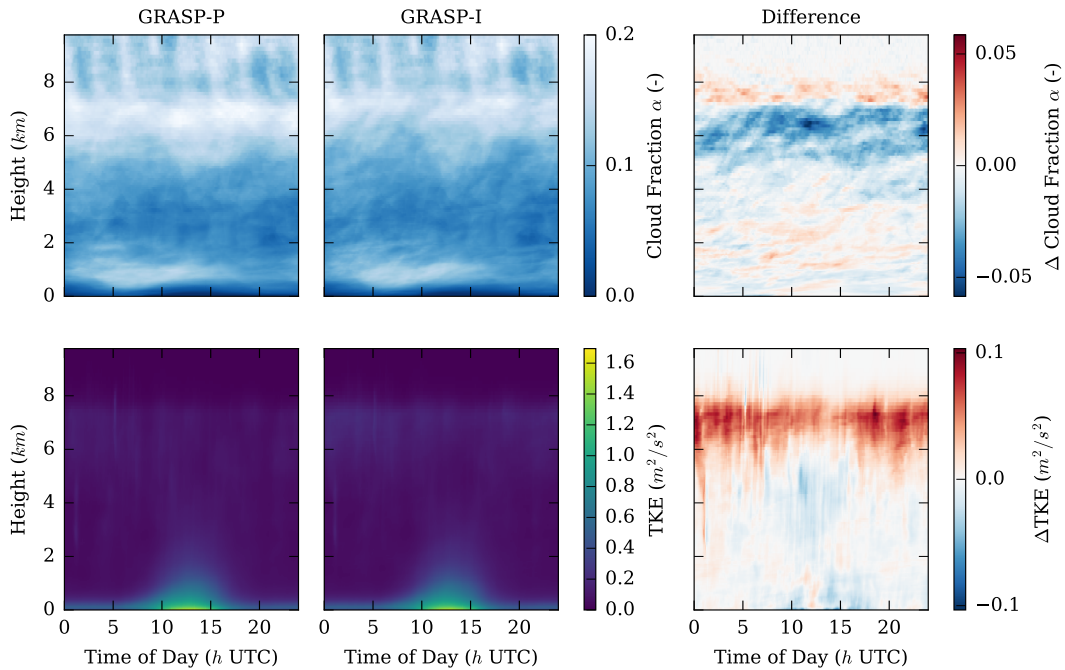Figure 4.11: The average diurnal cycle of the vertical profiles of the cloud fraction α (-) and the turbulence kinetic energy (TKE, m^2/s^2) at Cabauw (the Netherlands) as predicted by the two GRASP models a day ahead. The model with the prescribed radiation is displayed in the left column, the one with the interactive radiation in the middle column, and the difference between both models, calculated as GRASP-I minus GRASP-P, is shown in the right column. The first row shows the vertical profile of α through the course of the day, the second row shows TKE. The average diurnal profiles were calculated based on individual daily forecasts of every day in 2016.

On a yearly average, GRASP-I has a higher TKE than GRASP-P in the region between 5 and 8 km. This can be observed in figure 4.11, which also shows that the time of day does not affect this difference in TKE between both models much. Furthermore, the implementation of interactive radiation does not show significant differences in the average turbulence in the convective boundary layer.

The average vertical profile of the day-ahead forecasted TKE is displayed in figure 4.12. This figure resonates that the region where the turbulence differs between the models closely overlaps with the region in which GRASP-I creates less clouds than GRASP-P.
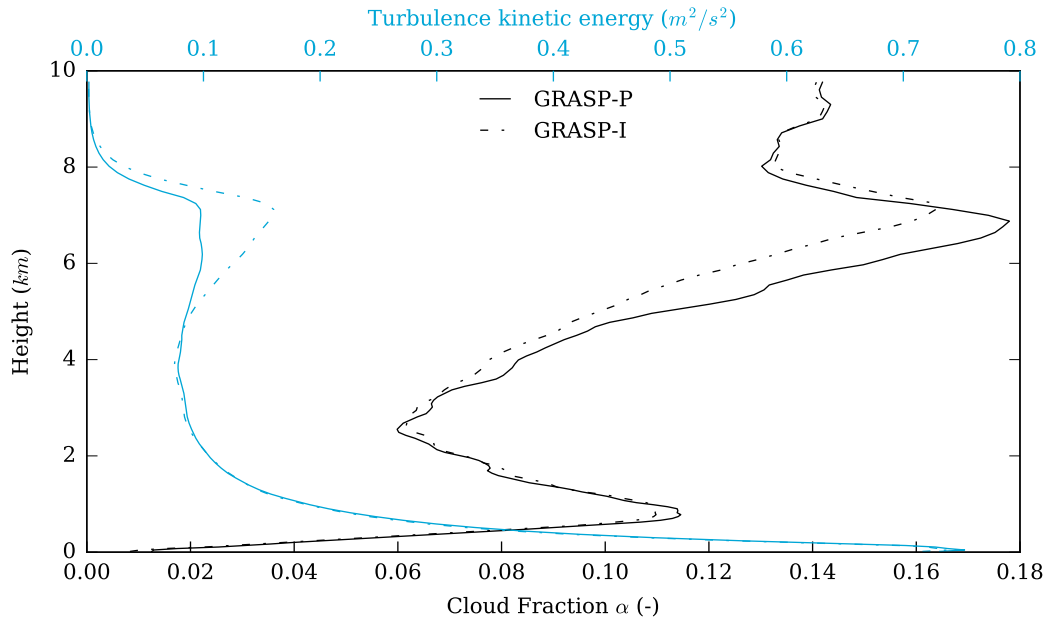

Figure 4.12: Average vertical profiles of all day-ahead forecasts in 2016 by the two GRASP models at Cabauw, the Netherlands. Solid lines represent the model with the prescribed radiation and dotted lines represent the one with the interactive radiation. The vertical profile of the average cloud fraction α is shown in black, the one of the average turbulence kinetic energy (TKE) is displayed blue.

4.2 Effect on down-welling radiation

In the previous section, the changes in thermodynamics that were introduced by implementing interactive radiation were discussed. Because the thermodynamic states of the atmosphere in both configurations of GRASP are different, down-welling radiation will be affected differently. This motivates studying the down-welling radiative fluxes, both short- and long-wave, in GRASP-P as well as GRASP-I and comparing the results. This section therefore addresses the effects of using interactive radiation on down-welling radiation.

4.2.1 Short-wave down-welling radiation

The effects of interactive radiation on short-wave down-welling radiation $S^{\downarrow}$ were studied by creating z, t-diagrams for $S^{\downarrow}$. The resulting figures showed that the effects of interactive radiation are consistent throughout all simulations, so the same two days are shown here as in the figures that were displayed in the previous section. The results are displayed in figure 4.13.

The basic features in figure 4.13 display the anticipated behavior for solar radiation. At the top of the domain, no $S^{\downarrow}$ is present during the night. When the Sun rises, the intensity of the radiative flux increases up to a maximum at the middle of the day, after which it decreases until it reaches zero at sunset. Following $S^{\downarrow}$ on its path down the atmosphere, figure 4.13 shows that clouds absorb (part of) the radiation, resulting in a decreased radiative flux underneath a cloud.

It is easily visible that the resulting radiative fluxes are different throughout the atmosphere. However, these differences between GRASP-I and GRASP-P are in accordance with the different cloud representations. The differences are again displayed in the panels on the right in figure 4.13.

In figure 4.13a, the clouds in GRASP-I rise in altitude, and disappear sooner than in GRASP-P. The difference panel shows that the higher cloud absorbs radiation higher in the atmosphere, leading to a decrease in $S^{\downarrow}$ in the region that was cloud-free in GRASP-P. The amount of $S^{\downarrow}$ eventually increases as a consequence of the earlier cloud evaporation in GRASP-I. In figure 4.13b, the clouds in GRASP-I rise in altitude and evaporate even more quickly. The impact on $S^{\downarrow}$ is clear, leading to an increase in $S^{\downarrow}$ up to 320 W/m^2.
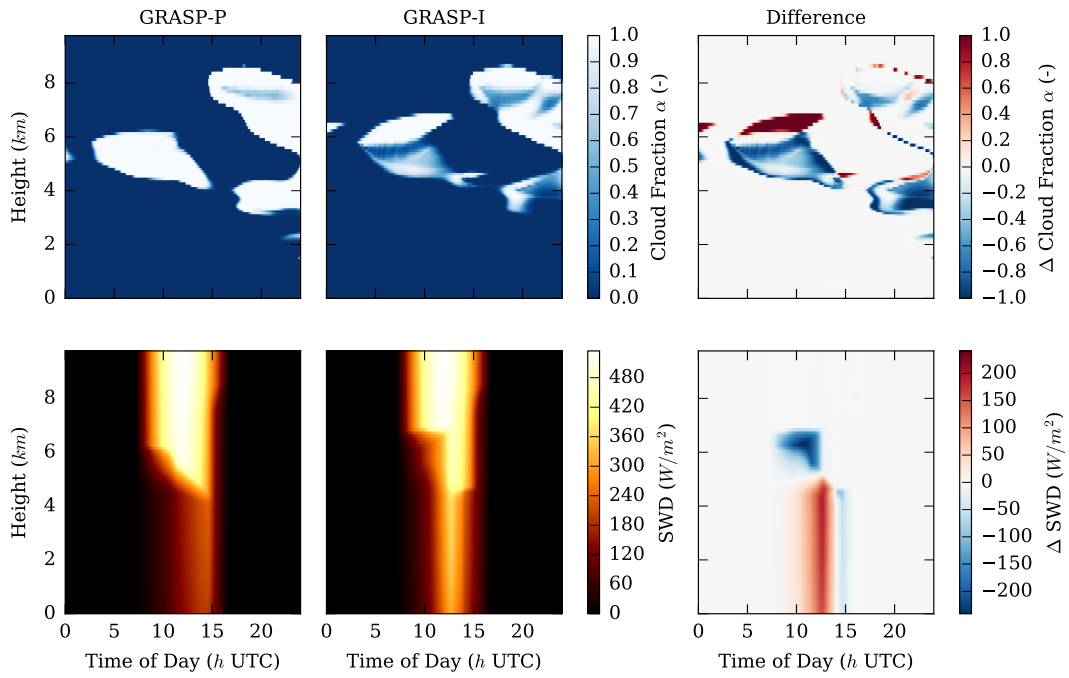
(a) February 13, 2016
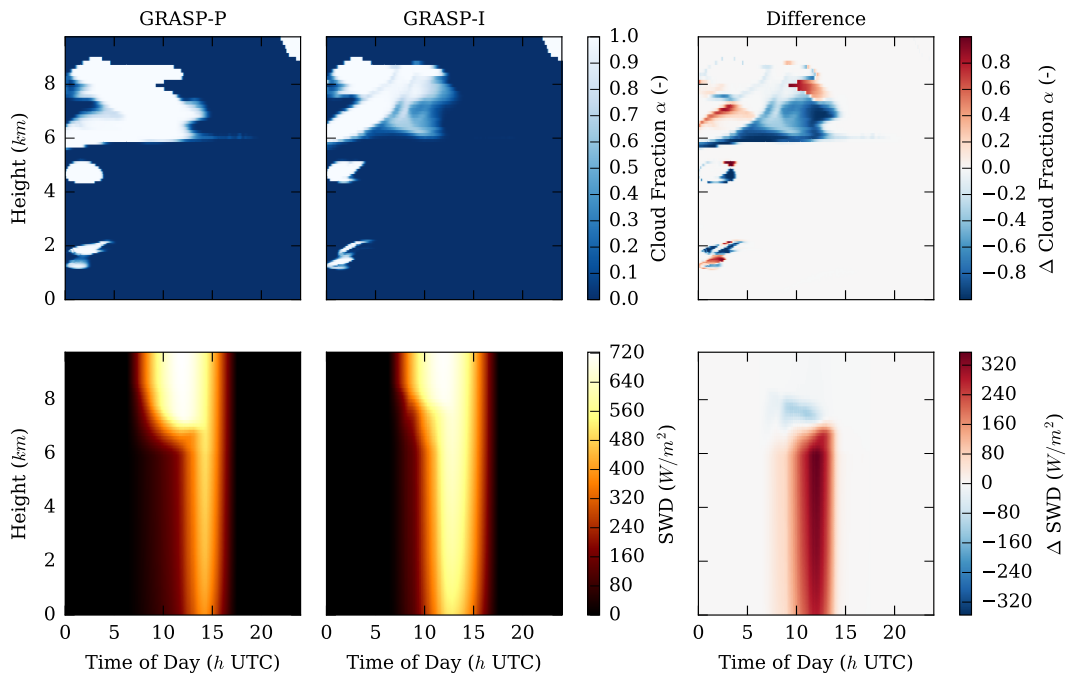
(b) March 9, 2016

Figure 4.13: Height-time diagrams of several day-ahead forecasts by the two GRASP models at Cabauw, the Netherlands. The model with the prescribed radiation is displayed in the left column, the one with the interactive radiation in the middle column, and the difference between both models, calculated as GRASP-I minus GRASP-P, is shown in the right column. The first row shows the vertical profile of the cloud fraction α (-) through the course of the day, the second row shows the short-wave down-welling radiation $S_b^{\downarrow}$ (SWD, W/m^2).

The average decline in cloud fraction between 4 and 7 km causes GRASP-I to exhibit more short-wave down-welling radiation on average than GRASP-P. The average z, t-diagrams are displayed in figure 4.14, showing that the difference in $S^\downarrow$ is up to 15 W/m^2 at the middle of the day. This discrepancy between both configurations results in more $S_b^\downarrow$ in GRASP-I. Figure 4.15 displays the average vertical profile of the cloud fraction α and the short-wave down-welling radiation $S^\downarrow$, which resonates the results of figure 4.14.
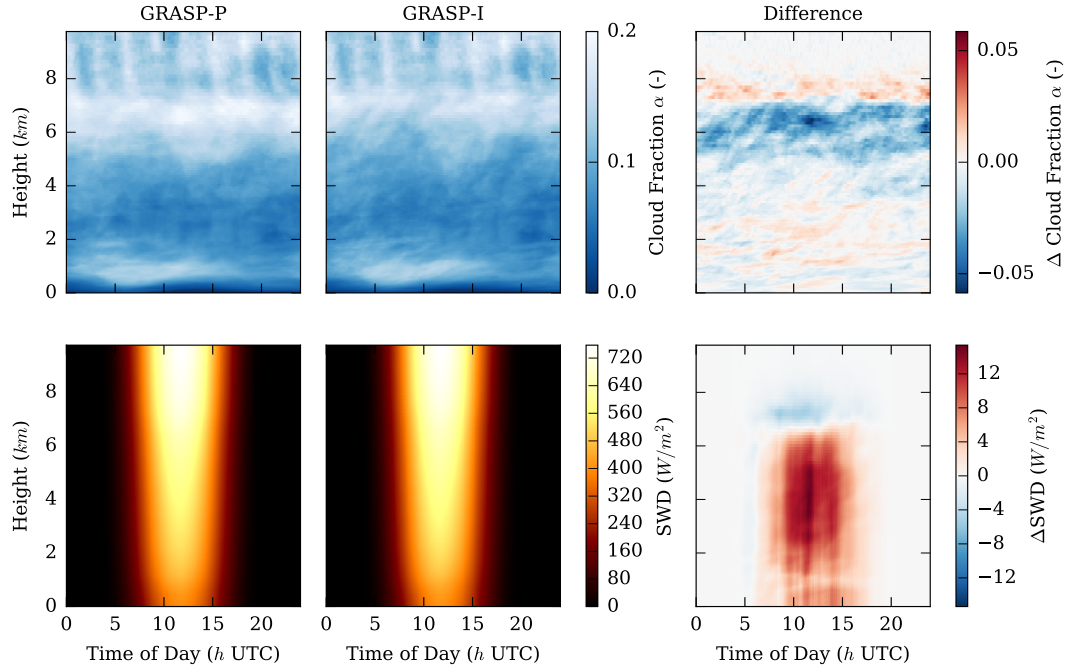

Figure 4.14: The average diurnal cycle of the vertical profiles of the cloud fraction α (-) and the short-wave down-welling radiation $S^\downarrow$ (SWD, W/m^2) at Cabauw (the Netherlands) as predicted by the two GRASP models a day ahead. The model with the prescribed radiation is displayed in the left column, the one with the interactive radiation in the middle column, and the difference between both models, calculated as GRASP-I minus GRASP-P, is shown in the right column. The first row shows the vertical profile of α through the course of the day, the second row shows $S^\downarrow$. The average diurnal profiles were calculated based on individual daily forecasts of every day in 2016.
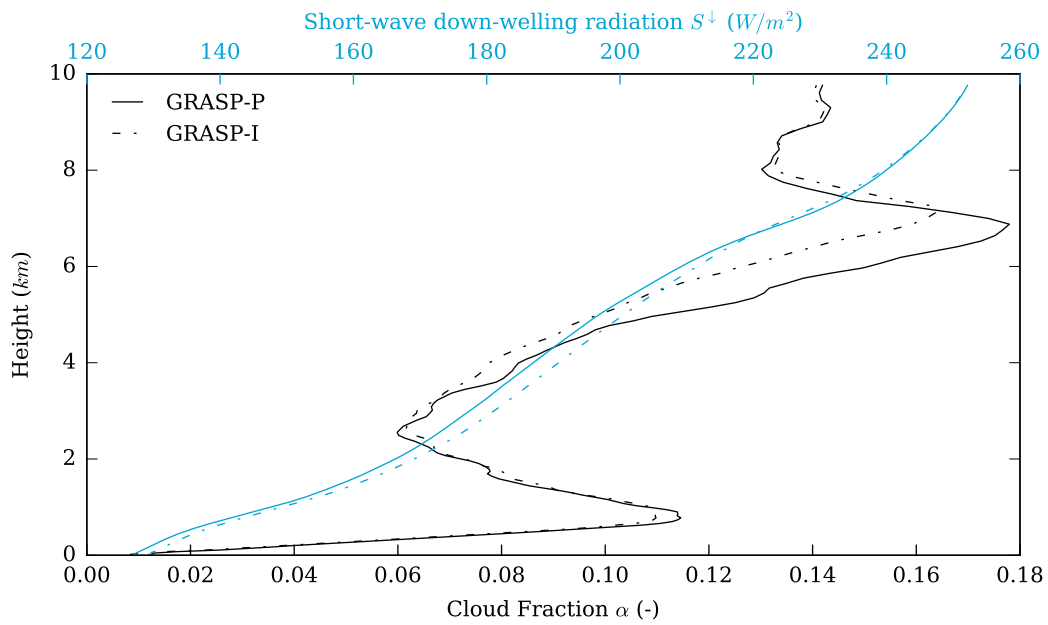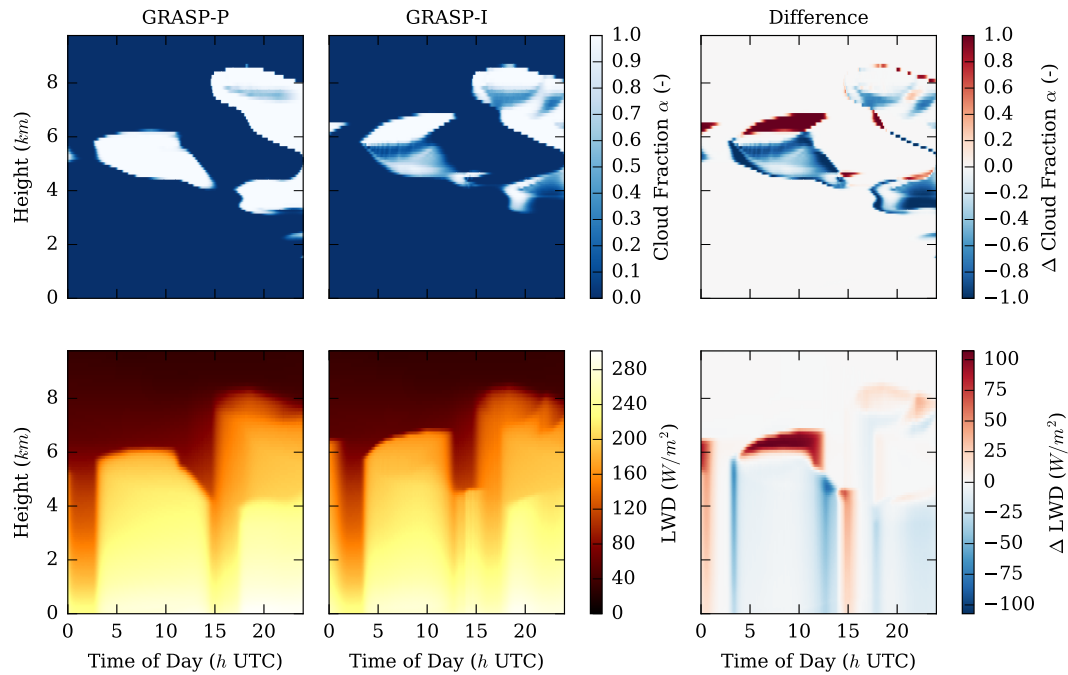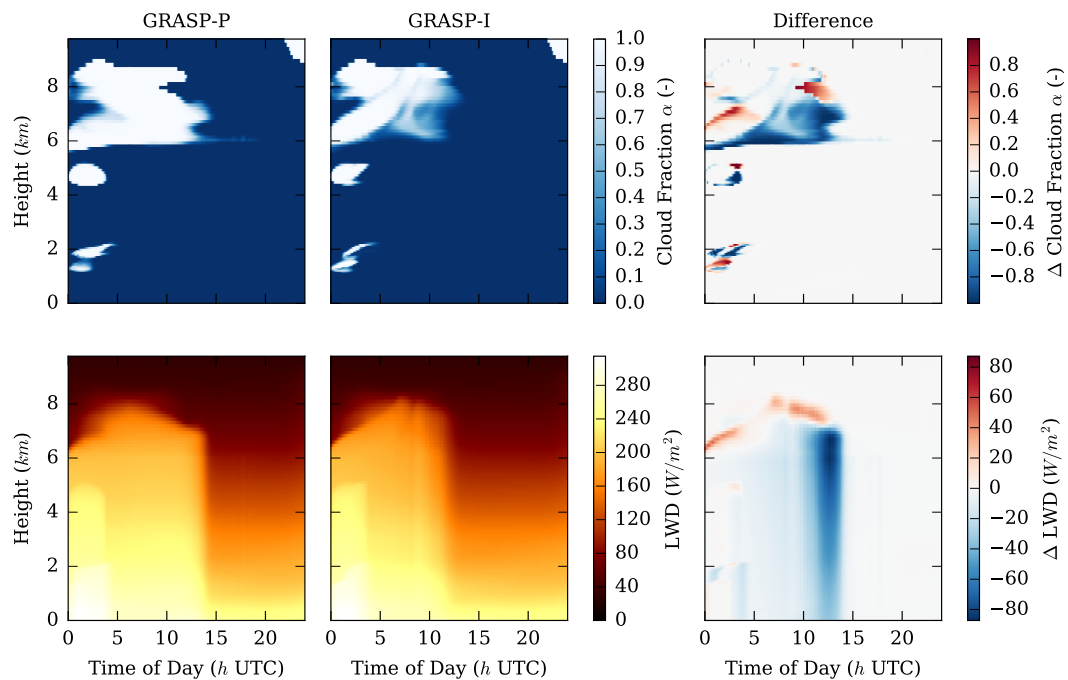
Figure 4.15: Average vertical profiles of all day-ahead forecasts in 2016 by the two GRASP models at Cabauw, the Netherlands. Solid lines represent the model with the prescribed radiation and dotted lines represent the one with the interactive radiation. The vertical profile of the average cloud fraction α is shown in black, the one of the average short-wave down-welling radiation $S^\downarrow$ (SWD, W/m^2) is displayed blue.

4.2.2 Long-wave down-welling radiation

(a) February 13, 2016

(b) March 9, 2016

Figure 4.16: Height-time diagrams of several day-ahead forecasts by the two GRASP models at Cabauw, the Netherlands. The model with the prescribed radiation is displayed in the left column, the one with the interactive radiation in the middle column, and the difference between both models, calculated as GRASP-I minus GRASP-P, is shown in the right column. The first row shows the vertical profile of the cloud fraction α (-) through the course of the day, the second row shows the long-wave down-welling radiation $L^{\downarrow}$ (LWD, W/m^2).

The effects of interactive radiation on long-wave down-welling radiation $L^\downarrow$ were also studied by creating z, t-diagrams for $L^\downarrow$. As with $S^\downarrow$, we display the same two simulated cases here, and these results are representative for all simulations that were performed. The results are displayed in figure 4.16.

Figure 4.16 displays the anticipated behavior for long-wave radiation, as the presence of clouds clearly increases the $L^\downarrow$ underneath them. The differences in $L^\downarrow$ between GRASP-I and GRASP-P are again in accordance with the different cloud representations; where GRASP-I simulated more clouds there is an increase in $L^\downarrow$, and $L^\downarrow$ decreases where less clouds are simulated. Figure 4.16b shows that the relative lack of clouds in GRASP-I leads to less long-wave radiation, in this case up to 80 W/m^2 less $L^\downarrow$ than GRASP-P.
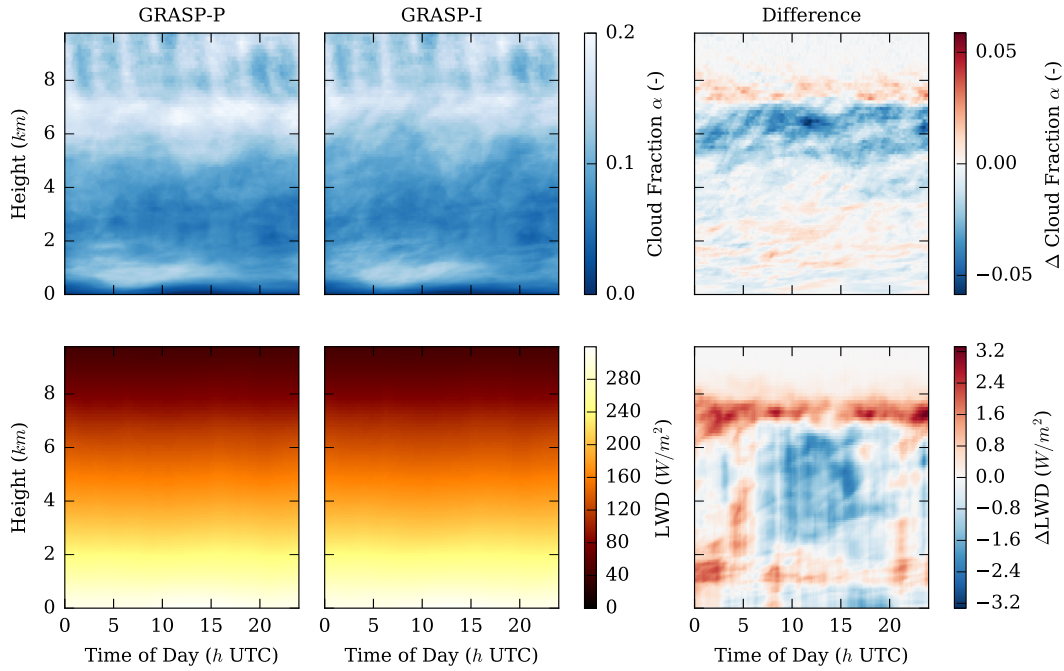

Figure 4.17: The average diurnal cycle of the vertical profiles of the cloud fraction α (-) and the long-wave down-welling radiation $L^\downarrow$ (LWD, W/m^2) at Cabauw (the Netherlands) as predicted by the two GRASP models a day ahead. The model with the prescribed radiation is displayed in the left column, the one with the interactive radiation in the middle column, and the difference between both models, calculated as GRASP-I minus GRASP-P, is shown in the right column. The first row shows the vertical profile of α through the course of the day, the second row shows $L^\downarrow$. The average diurnal profiles were calculated based on individual daily forecasts of every day in 2016.

Because we have established that GRASP-I produces less clouds on average, we might expect less long-wave radiation to come welling down the atmosphere. Figure 4.17 shows this is the case during day-time between 2 and 7 km altitude. However, figure 4.17 also shows regions where GRASP-I produced on average more $L^{\downarrow}$ than GRASP-P which are not necessarily corresponding to regions where GRASP-I simulated more clouds on average. Figure 4.18 shows that the differences in $L^{\downarrow}$ are negligibly small.
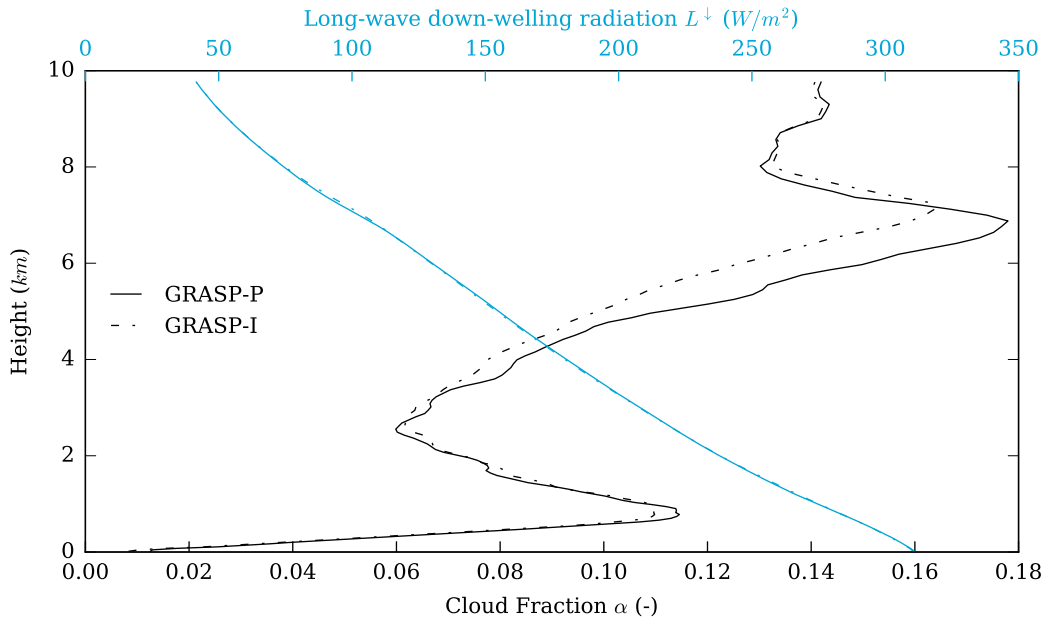

Figure 4.18: Average vertical profiles of all day-ahead forecasts in 2016 by the two GRASP models at Cabauw, the Netherlands. Solid lines represent the model with the prescribed radiation and dotted lines represent the one with the interactive radiation. The vertical profile of the average cloud fraction α is shown in black, the one of the average long-wave down-welling radiation $L^{\downarrow}$ (LWD, W/m^2) is displayed blue.

4.3 Statistical assessment of radiative prediction skill

The general radiative prediction skill of both GRASP models (GRASP-P and GRASP-I) was assessed by comparing the down-welling short-wave radiation at the bottom of the atmosphere $S_b^\downarrow$ (W/m^2) with observations from the Baseline Surface Radiation Network (BSRN). The GCM forecast that was used to drive the large-scale motions in both GRASP models, ECMWF's IFS, is also included in this study. This serves as a tool to not only assess the difference in forecast quality of the two GRASP models, but to also provide a benchmark to assess the quality of GRASP's radiation altogether.

4.3.1 Validation of surface radiation

Although both GRASP and IFS outputs contain detailed radiation fluxes and heating rates at many vertical levels, we are restricted in our validation to the radiation at Earth's surface at Cabauw for the simple reason that it is the only place we can compare the predictions with actual observations. Evaluating radiation at the bottom of the atmosphere is however very useful, because it reflects the models representation of the entire atmosphere through its interaction with radiation. The down-welling radiation that reaches Earth's surface affects the surface temperature and thus impacts many other processes. The overall first order statistics of this study are listed in table 4.1. The reader is assumed to be familiar with these statistic indicators, but in light of completeness, the formulas used to compute the scores in table 4.1 are listed in appendix B.

Table 4.1: Statistical indicators of day-ahead predicted $S_b^\downarrow$ at Cabauw, the Netherlands in 2016. The prognostic models (GRASP-P, GRASP-I and IFS) were compared with BSRN observations of $S_b^\downarrow$. Data pairs are temporal averages of 3 hours each. RMSE is the root mean squared error, rRMSE is the relative RMSE, MAE is the mean absolute error and r is the Pearson correlation coefficient.

Model	N	Mean (W/m^2)	Bias (W/m^2)	σ (W/m^2)	RMSE (W/m^2)	rRMSE (-)	MAE (W/m^2)	r (-)
GRASP-P	1301	280.1	3.7	122.4	122.4	.44	80.6	.84
GRASP-I	1301	285.2	8.9	115.4	115.7	.42	76.3	.85
IFS	1301	273.1	-3.2	87.2	87.3	.32	61.2	.90

The main results of table 4.1 are the following. GRASP with interactive radiation shows an improved root mean square error (RMSE) when compared to GRASP with prescribed radiation. The mean absolute error (MAE) decreased as well. This indicates that the implementation of interactive radiation reduced the error in $S_b^\downarrow$ on average which can be interpreted as an improvement of skill, albeit small. Nevertheless, both configurations are outperformed by IFS in terms of error magnitude.

In both GRASP configurations, the variance in the error is the main contributor to the total error. There is no large systematic deviation (bias) in our predictions of $S_b^\downarrow$ in both cases. The small positive bias that was already present in GRASP-P increased after the implementation of interactive radiation, which indicates that on average too much down-dwelling short-wave radiation reaches Earth's surface. These scores confirm that the average $S_b^\downarrow$ is higher in GRASP-I than in GRASP-P, as was discovered in the previous section.

Figure 4.19 displays the time series of the error in $S_b^\downarrow$ for both GRASP configurations during the year 2016. This visual representation resonates with the results in table 4.1: the error does not appear clearly biased, but is certainly subject to volatile fluctuations. Errors in the order of a few hundred W/m^2 are not uncommon, which is especially serious considering that the data pairs are averaged over 3 hours and thus cannot be dismissed as short mistakes.

Furthermore, figure 4.19 shows no correlation with respect to time. The absolute magnitude of errors appears somewhat larger in the summer months, but this is to be expected due to the higher solar irradiance at the top of the atmosphere $S_t^\downarrow$ in those months compared to the
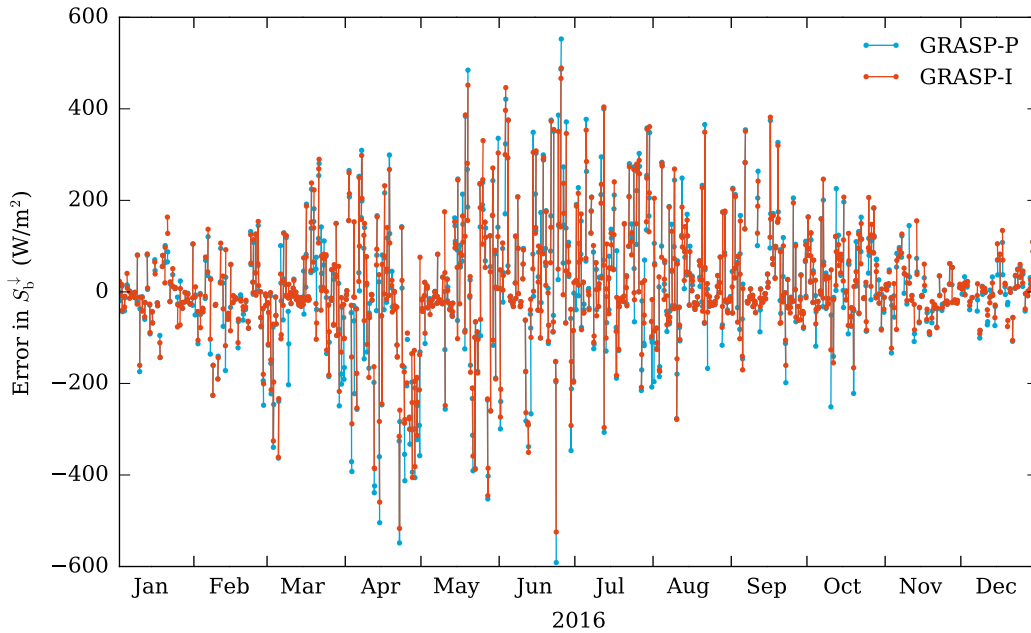
Figure 4.19: Error in $S_b^\downarrow$ for both GRASP configurations during 2016 at Cabauw, the Netherlands. Errors were calculated with respect to BSRN observations. Values are temporal averages of 3 hours.

winter months.

Another conclusion that can be drawn from figure 4.19 is that there is no big difference between the error in $S_b^\downarrow$ made by GRASP-P or by GRASP-I. This indicates that the inaccuracy in $S_b^\downarrow$ is not specifically influenced by the radiative configuration, and probably originates somewhere else in GRASP. In fact, all of the subsequent research yielded similar results for GRASP-P and GRASP-I, confirming that these errors are primarily independent of the configuration of the radiative transfer method. We will therefore continue by showing only the results for GRASP-P for the remainder of this chapter, and the reader may assume similar results for GRASP-I. For completeness, all results for GRASP-I are reported in appendix A.

4.3.2 Error correlation with cloud fraction

These results were followed by an examination of possible explanations of the errors. Linear correlations of $r = -0.44$ and $r = -0.42$ (for GRASP-P and GRASP-I, respectively) were found between the error in $S_b^\downarrow$ and the average cloud fraction $\langle \alpha \rangle$. The time series of 3 hour averaged cloud fractions and errors in $S_b^\downarrow$ are displayed in figure 4.20.

The negative correlation between these two signals suggests that negative errors in $S_b^\downarrow$ (i.e. when more down-welling solar radiation was observed in reality than GRASP had predicted a day ahead) might occur when there is a higher cloud fraction in GRASP (and vice versa). We can indeed observe in figure 4.20 (for example during the first days of March and at the end of April) that several successive days are suffering a large negative error in $S_b^\downarrow$ while there is a significant cloud fraction in GRASP.

This may seem somewhat obvious, as cloud fraction and short-wave radiation are not independent variables (the presence of clouds should indeed prohibit a fraction of the solar radiation from reaching the ground). However, this is not merely a negative correlation between cloud fraction and short-wave radiation, but we observe a negative correlation with the *error* of the short-wave radiation. From this follows that either the clouds in GRASP have a larger impact on radiation than they should, or too much clouds are simulated on moments when there
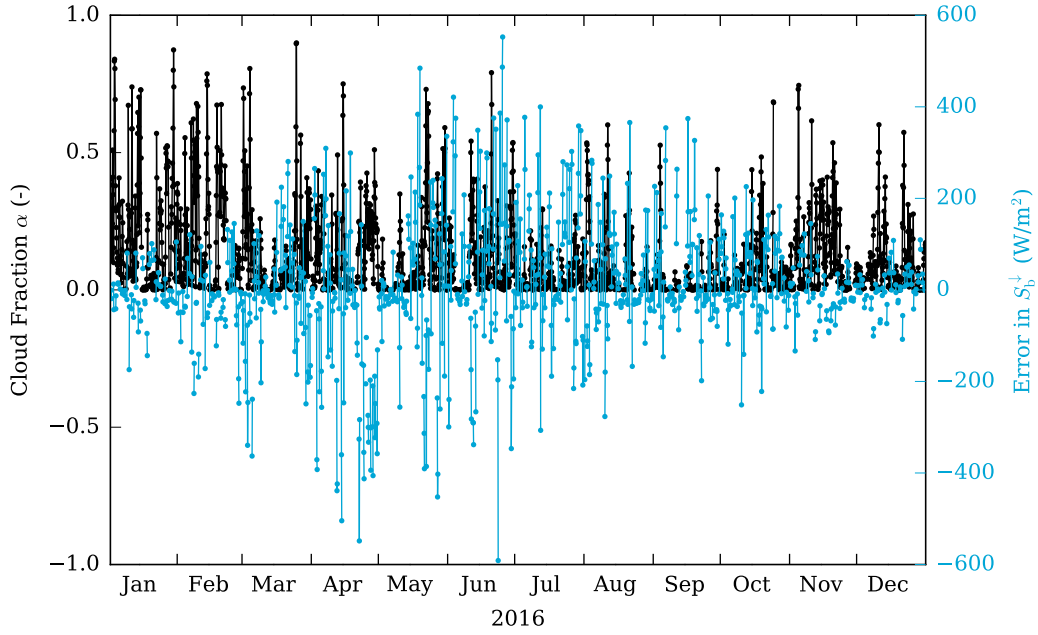
Figure 4.20: Output of GRASP-P for 2016 at Cabauw, the Netherlands. The cloud fraction is shown in black, the error in $S_b^\downarrow$ (calculated with respect to BSRN observations) is shown in blue. Variables have been averaged in time over 3 hour windows. Correlation between the two signals is $r = -0.44$. The results are similar for GRASP-I.

should be less.

Clouds consist of liquid water droplets, frozen ice crystals, or a combination of both. In the simulations, the cloud fraction is dependent on the distribution of the total (non-precipitating) water specific humidity q_t over the water vapor specific humidity q_v, the liquid water specific humidity q_l and the ice specific humidity q_i, as was discussed in chapter 2. These parameters are integrated over height z from Earth's surface to the top of atmosphere (TOA) to obtain a representation of the total mass of water (in a specific phase) in a vertical column with a cross section of one square meter:

$$\text{TCLW} = \int_0^{\text{TOA}} \rho(z)\, q_l(z)\, dz \tag{4.2}$$

$$\text{TCIW} = \int_0^{\text{TOA}} \rho(z)\, q_i(z)\, dz \tag{4.3}$$

$$\text{TCWV} = \int_0^{\text{TOA}} \rho(z)\, q_v(z)\, dz \tag{4.4}$$

where TCLW is the total column liquid water, TCIW is the total column ice water and TCWV is the total column water vapor (all three in kg/m^2). The correlation between these variables (as used in the call to RRTM-G) and the error in $S_b^\downarrow$ was calculated. The resulting Pearson correlation coefficients are listed in table 4.2, and indicate that the liquid and ice water content in GRASP's RRTM-G calls are to some extent correlated with the error in the down-welling short-wave radiation at Earth's surface. This suggests that the RRTM-G is implemented incorrectly, or is receiving erroneous liquid and/or ice water contents.

As a follow-up, the deviation between the total column water amounts in IFS and the corresponding total column water amounts that were used in the call to RRTM-G for the calculation of radiative transfer in GRASP was investigated. The results for GRASP-P are

Table 4.2: For each model, the Pearson correlation coefficients r between the error in $S_b^\downarrow$ and the variables in the top row. For the two GRASP models, the values of r are calculated based on the variables as they are used in the call to RRTM-G.

	$\langle\alpha\rangle$	TCLW	TCIW	TCWV
GRASP-P	-.44	-.37	-.31	.04
GRASP-I	-.42	-.34	-.32	.04
IFS	-.07	-.12	-.01	.05

displayed in figure 4.21 in scatterplots. Every single dot represent the average value of a particular variable over a time period of 3 hours. The y-axis quantifies the amount that was predicted by GRASP-P, and the amount on the x-axis is taken from the corresponding IFS forecast.

Because this was the GRASP run with prescribed radiation, these thermodynamic variables are not expected to differ much from IFS, and we would expect all dots around the diagonal. Large deviations from IFS during the simulation are not expected since GRASP-P should use the same initial conditions as IFS and employs the radiative tendencies that were calculated based on the specific humidities from IFS. However, figure 4.21 shows that there is a lot of deviation between the amount of liquid water in GRASP's call to RRTM-G and in IFS (left panel). This is most remarkable, as it shows that the state of the atmosphere in GRASP-P is not similar to the state of the atmosphere in IFS at all.
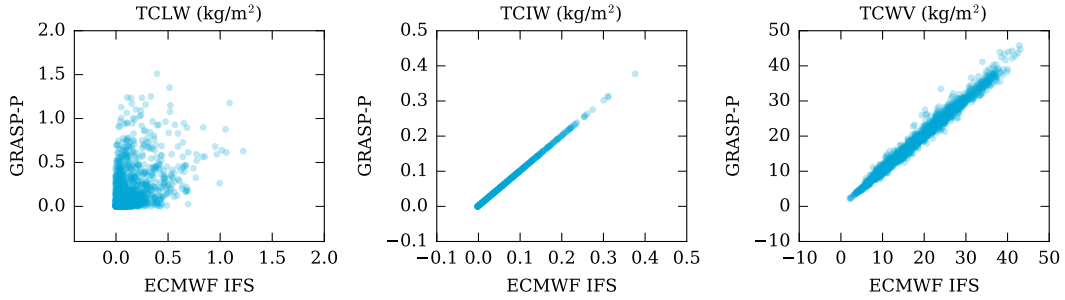

Figure 4.21: Scatterplots of total column water contents in ECMWF IFS and GRASP-P. From left to right, day-ahead predictions of total column liquid water, ice and water vapor are compared.

There is no difference between the amount of ice in GRASP and in IFS (middle panel), and since there is no correlation between the error of $S_b^\downarrow$ in IFS and its amount of ice, there is little reason at this point to believe that the amount of ice itself is wrong. The fact that the error in $S_b^\downarrow$ does correlate with the amount of ice suggests that for some reason, the presence of ice is contributing to the radiation error in an indirect way.

It is not unreasonable to presume that computational errors are made during the conversions of these variables to the GRASP interface during initialization. If this would be the case, the errors would already be present immediately after initialization. To test this, figure 4.22 therefore shows the same scatterplot, using only the very first value of each run (i.e. the values immediately after initialization of each simulation). There are still large deviations in the liquid water content between IFS and GRASP. Apparently, the liquid water content is altered strongly during initialization in the conversion of variables from the large-scale model to the GRASP interface. The deviations in the amount of liquid water motivate further research into the effects of liquid water on radiation in GRASP.
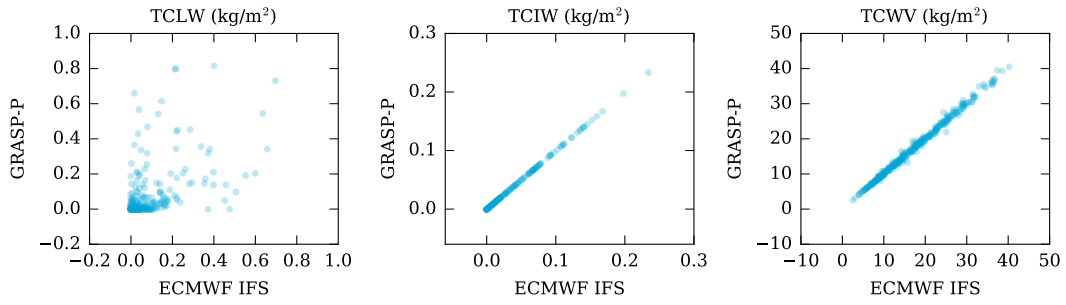
Figure 4.22: Scatterplots of total column water contents in ECMWF IFS and GRASP-P immediately after initialization. Each dot represents the first value in one GRASP-P run. From left to right, values of total column liquid water, ice and water vapor are compared.

4.3.3 Liquid water content

Figure 4.23 displays day-ahead forecasted short-wave down-welling radiation at the bottom of the atmosphere ($S_b^\downarrow$, W/m^2) by GRASP-P and the associated observations by BSRN. If a dot lies on the diagonal, it signifies a moment where GRASP-P had predicted the exact amount of $S_b^\downarrow$ that was later observed. If a dot lies above the diagonal, it means that GRASP-P had predicted more $S_b^\downarrow$ than was observed, and the other way around if a dot lies beneath the diagonal. The larger the distance of a certain dot from the diagonal, the larger the prediction error associated with that moment.

The goal of this part of the research is to characterize the prediction errors, so we might learn why they occur. Based on the results from table 4.2 and figures 4.21 and 4.22, a color map was used to signify the total column liquid water content (TCLW, kg/m^2) that was predicted by GRASP-P for every dot. The results are straightforward. Figure 4.23 shows that negative prediction errors (i.e. when GRASP's prediction of $S_b^\downarrow$ was too small) are often occurring when GRASP had predicted a relative high amount of liquid water.

We considered the possibility that the negative correlation between the amount of TCLW and error in $S_b^\downarrow$ is trivial in NWP models. Although unlikely, this correlation could be an artifact of radiative transfer methods, as the amount of water directly influences the simulated $S_b^\downarrow$. Figure 4.24 displays the same scatter plot as was displayed in figure 4.23, only showing the day-ahead IFS forecast instead of the GRASP forecasts. This figure confirms that the IFS forecast does not suffer the same negative correlation between the amount of TCLW and error in $S_b^\downarrow$, which implies that this is not simply a problem all NWP models suffer.
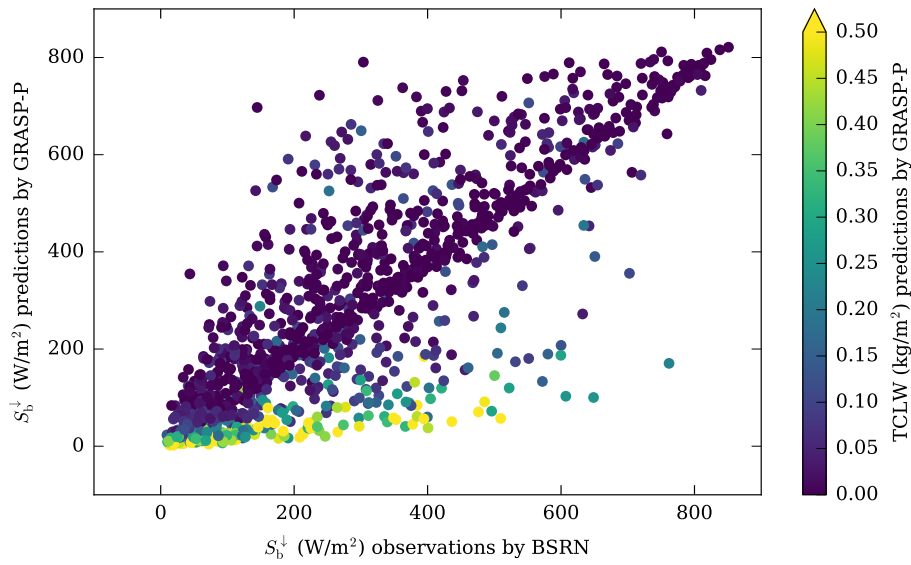
Figure 4.23: Scatterplot of day-ahead forecasted $S_{\mathrm{b}}^{\downarrow}$ (W/m²) by GRASP-P and the associated observations by BSRN for 2016 at Cabauw, the Netherlands. Variables have been averaged in time over 3 hour windows. The points are color-coded with GRASP's prediction of the total column liquid water (kg/m²). The results are similar for GRASP-I.

Figure 4.24: Scatterplot of day-ahead forecasted $S_{\mathrm{b}}^{\downarrow}$ (W/m²) by IFS and the associated observations by BSRN for 2016 at Cabauw, the Netherlands. Variables have been averaged in time over 3 hour windows. The points are color-coded with IFS's prediction of the total column liquid water (kg/m²). The results are similar for GRASP-I.
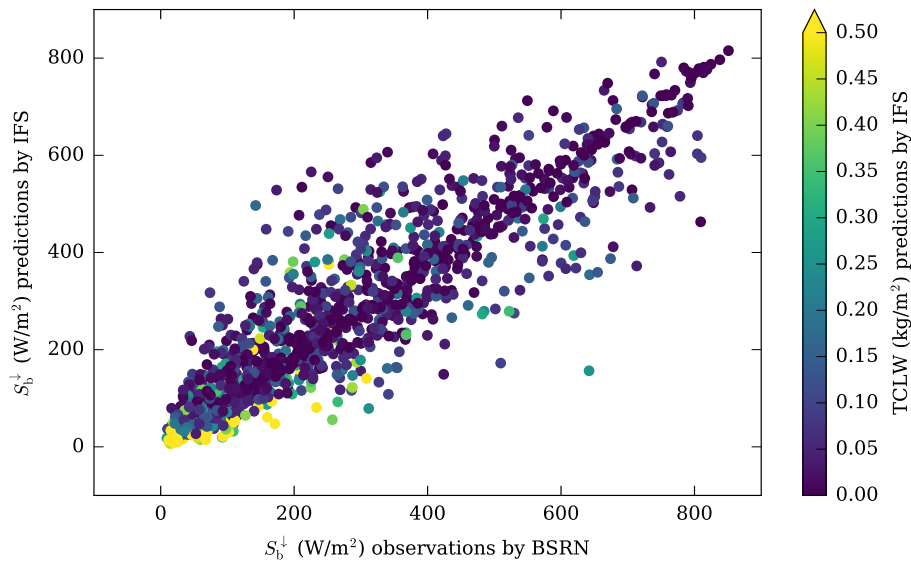
4.3.4 Error in liquid water content

We have established that GRASP alters the initial conditions of liquid water in converting the variables from the large-scale model to GRASP. Furthermore, we have seen that the amount of liquid water is correlated to the error in short-wave down-welling radiation. It seems likely that the error in $S_b^\downarrow$ may (at least in part) be attributed to errors in the amount of liquid water, caused by wrongly converting the initial conditions to GRASP's interface.

To evaluate the error GRASP makes in predicting TCLW we compiled 3 hour averages of the TCLW from the ERA5 re-analysis forecast. This is also an NWP model, but it is the closest thing to observations of TCLW. We were then able to reconstruct figure 4.23 where $S_b^\downarrow$ predictions by GRASP-P were scattered against corresponding observations by BSRN. Now, the deviation in TCLW between GRASP-P's prediction and ERA5's re-analysis is used to signify the error in liquid water in GRASP. The results are displayed in figure 4.25.

The figure shows that if GRASP-P's prediction of TCLW is correct, the prediction of $S_b^\downarrow$ is mostly correct as well. However, the moments at which GRASP-P creates too much liquid water (classified by the blueish dots in figure 4.25), too little $S_b^\downarrow$ reaches Earth's surface. When there is less TCLW in GRASP-P than there should have been (classified by the reddish dots in figure 4.25), there is an abundance of down-welling short-wave radiation at the surface. The linear correlation between the error in the prediction of the total column liquid water and the error in the prediction of short-wave down-welling radiation is $r = -0.48$.
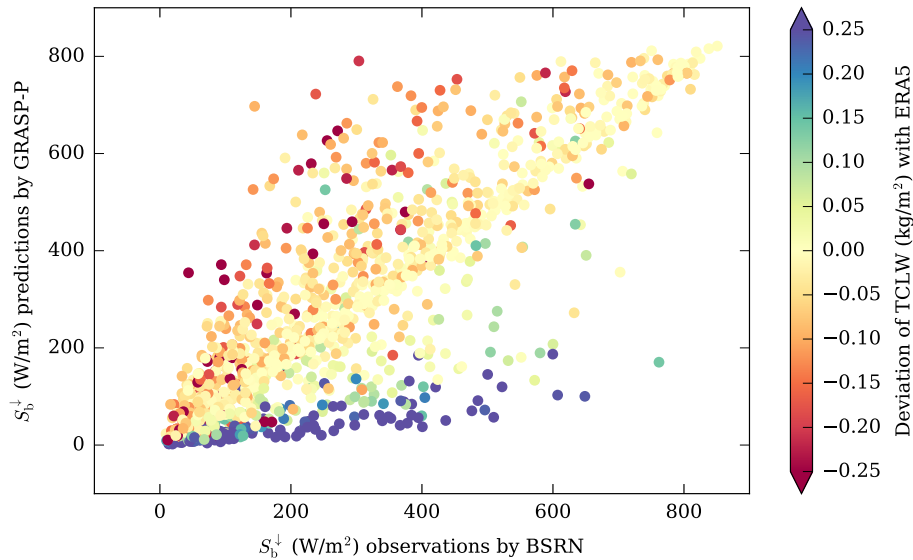

Figure 4.25: Scatterplot of day-ahead forecasted $S_b^\downarrow$ (W/m^2) by GRASP-P and the associated observations by BSRN for 2016 at Cabauw, the Netherlands. Variables have been averaged in time over 3 hour windows. The points are color-coded with deviation between GRASP's prediction of the total column liquid water (kg/m^2) and the associated re-analysis by ERA5. The results are similar for GRASP-I.

The implication of these results is straightforward. GRASP-P makes errors in its evaluation of total column liquid water and those inaccuracies have the anticipated effect on radiation: too much liquid water in the domain causes too little down-welling short-wave radiation on Earth's surface, and vice versa. Based on the earlier observation that deviations in the amount of liquid water are introduced in the conversion of initial conditions from IFS to GRASP, it is presumed that fixing these conversion errors could reduce the error in the liquid water content and improve the accuracy in radiative transfer. To investigate this, the deviations between the predicted amount of TCLW in GRASP forecasts and in IFS were calculated. These differences were used to color the scatter plots in figure 4.26.
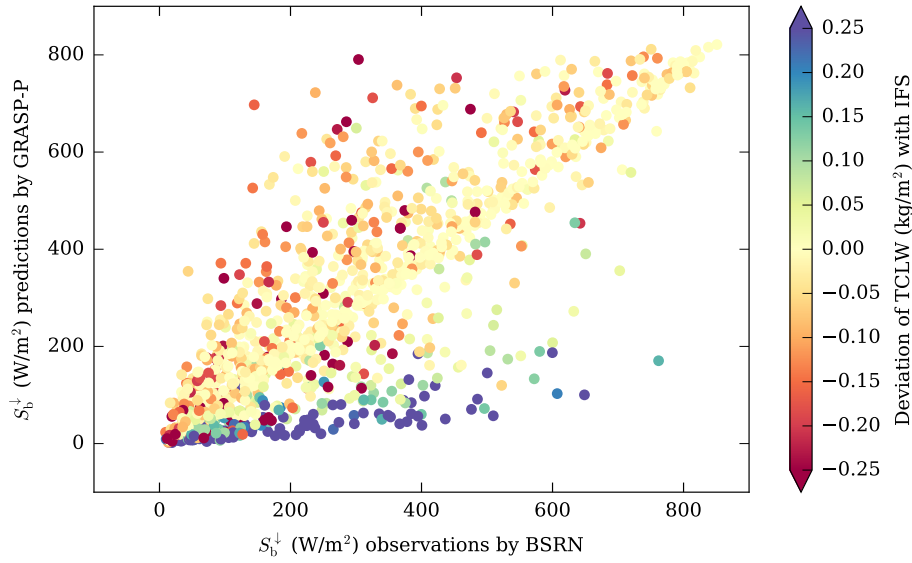
Figure 4.26: Scatterplot of day-ahead forecasted $S_b^\downarrow$ (W/m^2) by GRASP-P and the associated observations by BSRN for 2016 at Cabauw, the Netherlands. Variables have been averaged in time over 3 hour windows. The points are color-coded with deviation between GRASP's prediction of the total column liquid water (kg/m^2) and the associated prediction by IFS. The results are similar for GRASP-I.

In figure 4.26 it is apparent that the moments at which GRASP does not deviate from IFS in its diagnosis of the amount of liquid water, its prediction of $S_b^\downarrow$ is more often correct (the yellow dots in the figures often lie around the diagonal). When GRASP contains more liquid water than IFS (indicated by blueish dots), too little $S_b^\downarrow$ reaches Earth's surface. The other way around, too much $S_b^\downarrow$ reaches the surface if GRASP contains less liquid water than IFS. In conclusion, errors in the conversion of the initial conditions from the large-scale model to the GRASP interface are responsible for erroneous amounts of liquid water and the resulting inaccuracies in the prediction of solar radiation.

5

Discussions

5.1 Interpretation of the results

One of the major effects of the implementation of interactive radiation that was discovered was that clouds were rising more often. This process occurs in correlation with a significant increase in turbulent kinetic energy and regularly leads to cloud breakup. A possible interpretation of these results follows the following chain of reasoning.

At the top of a cloud, a parcel of dry, warm air from above the inversion may enter the cloud through entrainment. This parcel is cooled by the evaporation of cloud water. This evaporative cooling can cause the parcel to become denser than the surrounding cloud and negative buoyancy forces accelerate the parcel further downwards within the cloud. This instability is also known as the 'cloud top entrainment instability' (Deardorff, 1980).

The resulting buoyancy force promotes turbulence in the cloud, which in turn promotes entrainment, hence closing a positive feedback loop. Yamaguchi and Randall (2008) used large-eddy simulations to model evaporatively driven entrainment in cloud-topped mixed layers to test this feedback loop. They confirmed that buoyancy reversal indeed enables the development of entrainment, leading to cloud breakup as a result. Deardorff (1980) had already observed that the drying of the cloud by entrainment starts from the cloud base and works its way up with time.

These studies are in agreement with the observations that were made in this study. The implementation of interactive radiation enabled cloud dissipation in several hours, starting from the cloud base and working up with time, associated with increased turbulence indicating instabilities. This suggests that the implementation of interactive radiation promotes the occurrence of cloud top entrainment instability in our large-eddy simulations.

Evaporatively driven entrainment should also be able to manifest itself in the case of prescribed radiation, and therefore the implementation of an interactive radiative transfer method does not yet explain the sudden occurrence of these phenomena. However, cloud top entrainment instability is a positive runaway feedback loop, which may need a certain amount of entrainment before it gets started. Another possibility is that the radiative cooling by prescribed radiation does not exactly take place at the cloud top, and that this displacement prevents entrainment. Either way, dynamic feedback about the current state of the atmosphere may play a crucial role in overcoming this entrainment threshold through long-wave cloud top cooling.

The presence of a cloud leads to long-wave cloud top cooling, reducing the local temperature which in turn can lead to additional condensation (Guan et al., 1997). Configuring the radiative transfer method interactively, the next calculation of radiative transfer will take this higher liquid water load into account, leading to more long-wave cooling, thus again closing a positive feedback loop. Using prescribed radiation, cloud-top cooling also promotes additional condensation, but since the next calculation step of radiative transfer does not use this infor-

mation, this does not lead to more long-wave cooling and the same positive feedback loop is not closed.

There are signs in the results of this study that support this theory: more cloud-top long-wave cooling was observed in GRASP-I than in GRASP-P for the cases that displayed cloud breakup. Large cloud top long-wave cooling rates promote cloud top entrainment (Curry, 1986), possibly creating enough entrainment to initialize evaporatively driven cloud top entrainment instability, which subsequently causes the cloud to dry out from the base up.

It is difficult to validate the occurrence of these phenomena in the simulations without observations about whether these events actually happened. Nevertheless, we can use our results to make some statements about the occurrence of cloud top entrainment instability on a statistical basis. This study has shown that the GRASP-P has a small positive bias in short-wave down-welling radiation when compared to observations. This study also pointed out that the prediction skill in solar radiation is in essence controlled by the prediction skill of cloud cover. The increased cloud dissipation induced by the implementation of interactive radiation in GRASP-I resulted in a further increase in the bias of $S_{\mathrm{b}}^{\downarrow}$, which discourages the idea that evaporatively driven entrainment instabilities should have dried up the cloud layer this often.

In reality, cloud top entrainment instability does not necessarily lead to cloud destruction. Multiple studies have shown the Lilly-Randall-Deardorff criterion (used to determine whether cloud top entrainment instability occurs) to be true while observations actually report solid layer clouds (e.g. Albrecht, 1991, Hanson, 1984). According to Randall (1984), cloud top entrainment instability sometimes only deepens the cloud layer, without destroying it. Yamaguchi and Randall (2008) confirm this statement, adding that cloud top entrainment instability is generally weak, and cloud breakup is not expected when other atmospheric processes are present to maintain the cloud layer. In conclusion, although it is inspiring to observe that the implementation of interactive radiation enables the development of feedback loops between clouds and radiation, this study was not able to verify the occurrence of those feedback processes.

5.2 Recommendations

The first and foremost recommendation for future research is to revise the diagnosis of liquid water content. The errors that have been observed in the prediction of short-wave down-welling radiation were large, and were found to correlate with errors in the liquid water mixing ratio. Errors in liquid water content arise during the conversion of the initial conditions from the large-scale model to the GRASP interface. No advances in configuration or programming of radiative transfer will ever be able to correctly predict radiation, as long as cloud representation is false. The skill at which the state of atmosphere is predicted controls the radiative prediction skill. Right now, it seems that large profits in terms of radiative prediction skill can be realized by further investigation into the initialization errors during the conversion of liquid water content.

Figure 4.2 showed remarkable periodic patterns in the diurnal evolution of the average cloud fraction above 7 km altitude. It seems safe to assume that this is a simulation artifact, since the period of the pattern (3 hours) coincides with the temporal resolution of the large-scale weather model used for nudging, which is strongest in the top of the domain. Also, there is no reason to believe that such a pattern would occur in reality. It would be relatively easy to test whether these fringes are a result of the strong nudging in the upper part of the domain. The simulations of one of the models (doesn't matter whether it is GRASP-P or GRASP-I since they show the same fringes) should be run again keeping all parameters equal to the original run, except domain height. If the domain were to be increased to 20 km for example, finding the same fringes from ± 14 km upward in the diurnal average cloud fraction graph of that run would suggest that nudging is the cause. If, however, the fringes still appear from 7 km upward, it may be the result of another aspect of the simulation.

6

Conclusions

Using large-eddy simulations (LES) coupled to a general circulation model (GCM), the present study assessed the impact of interactive radiation in day-ahead weather forecasts. The implementation of interactive radiation was found to impact cloud representation in the simulations. In most cases it has been discovered that clouds started rising as a consequence of interactive radiation. This process occurs in correlation with a significant increase in turbulence kinetic energy.

Cloud-related radiative effects such as cloud-top radiative cooling are displaced along with the clouds, leading to differences in the thermodynamic state of the atmosphere in the simulations. These differences affect the liquid water potential temperature locally. The different cloud representations lead to large differences in radiative fluxes, both short- and long-wave.

The clouds that were raised using interactive radiation tend to break up more often between 5 and 7 km altitude, leading to an average decrease in cloud fraction of 0.02 at these altitudes in comparison with using prescribed radiation. As a result, interactive radiation increased the average amount of short-wave down-welling radiation in the atmosphere. On average, the difference varies from several W/m^2 around sunrise and sunset up to 15 W/m^2 in the middle of the day.

The liquid water potential temperature increased by 0.1 K on average throughout the domain as a consequence of the implementation of interactive radiation. Whether this is a result of the dryer atmosphere, the displaced heating rates, or a combination of both could not be concluded in this study.

By comparing the short-wave down-welling radiation at the surface from the day-ahead LES forecasts with observations from the Baseline Surface Radiation Network (BSRN), the predictive skill of solar radiation was quantitatively evaluated. In general, it was found that large prediction errors are made in GRASP. Even while averaged over time periods of 3 hour, GRASP-P and GRASP-I produced root mean squared errors of 122.4 W/m^2 and 115.7 W/m^2, respectively. Although an improvement, the latter RMSE is still far above that of the benchmark model that was used (ECMWF IFS, which showed an RMSE of 87.3 W/m^2).

Regardless of the radiative configuration, errors are made in the conversion of the initial conditions from the large-scale model to the GRASP interface, leading to errors in the diagnosis of the liquid water content. The error in the prediction of liquid water correlates with the error in solar radiation ($r = -0.48$). In conclusion, the large error in solar radiation can partly be attributed to these conversion errors, and improvements in the initialization of the thermodynamic state are required to advance the prediction skill of solar radiation.
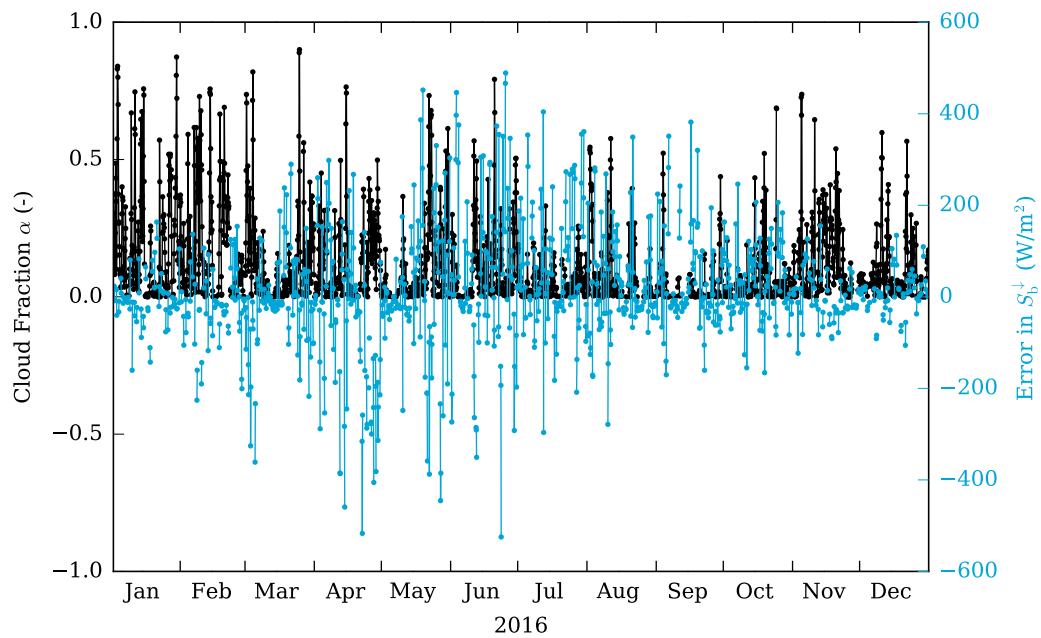
A
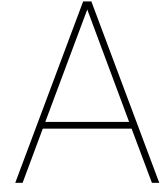
Extra Results

Figure A.1: Output of GRASP-I for 2016 at Cabauw, the Netherlands. The cloud fraction is shown in black, the error in $S_{\text{b}}^{\downarrow}$ (calculated with respect to BSRN observations) is shown in blue. Variables have been averaged in time over 3 hour windows. Correlation between the two signals is $r = -0.42$.
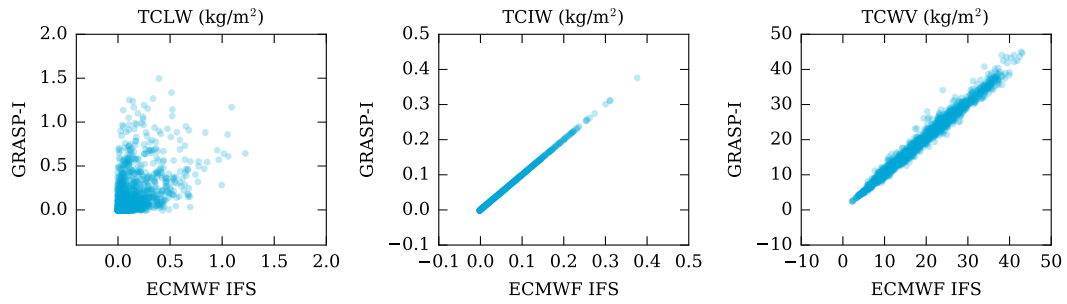
Figure A.2: Scatterplots of total column water contents in ECMWF IFS and GRASP-I. From left to right, day-ahead predictions of total column liquid water, ice and water vapor are compared.
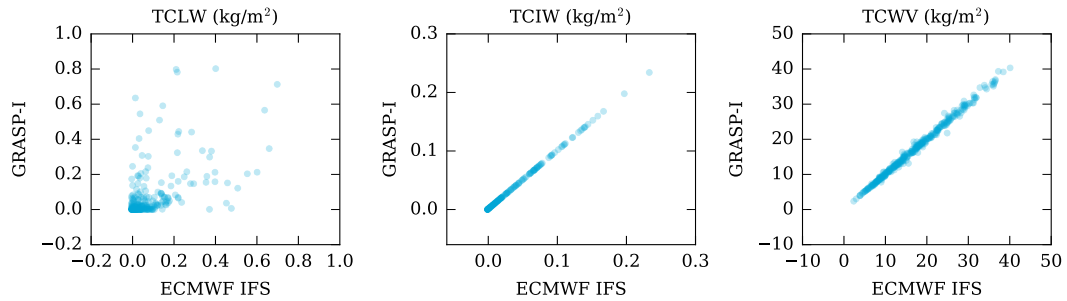

Figure A.3: Scatterplots of total column water contents in ECMWF IFS and GRASP-I immediately after initialization. Each dot represents the first value in one GRASP-I run. From left to right, day-ahead predictions of total column liquid water, ice and water vapor are compared.

Figure A.4: Scatterplot of day-ahead forecasted $S_{\mathrm{b}}^{\downarrow}$ (W/m^2) by GRASP-I and the associated observations by BSRN for 2016 at Cabauw, the Netherlands. Variables have been averaged in time over 3 hour windows. The points are color-coded with GRASP's prediction of the total column liquid water (kg/m^2).

Figure A.5: Scatterplot of day-ahead forecasted $S_{\mathrm{b}}^{\downarrow}$ (W/m²) by GRASP-P and the associated observations by BSRN for 2016 at Cabauw, the Netherlands. Variables have been averaged in time over 3 hour windows. The points are color-coded with GRASP's prediction of the liquid water content q_l (g/kg).
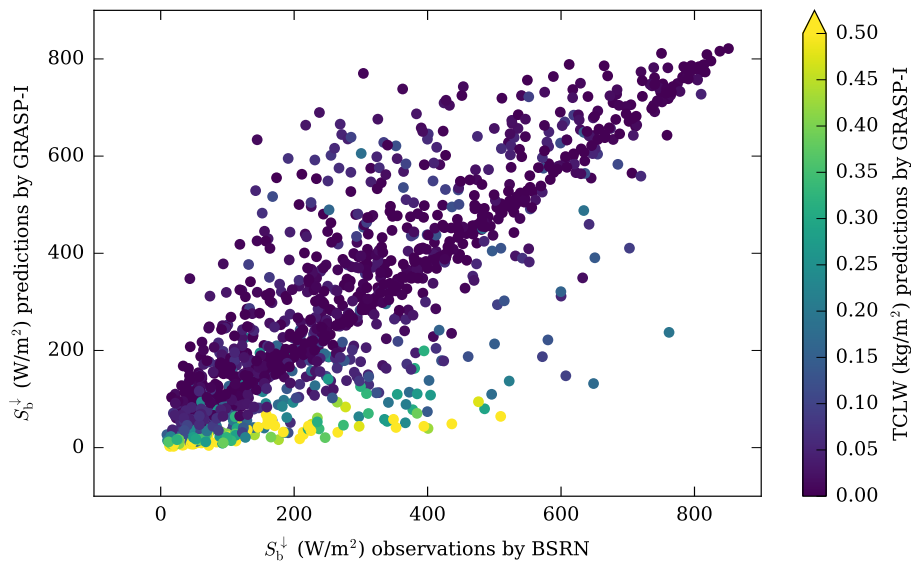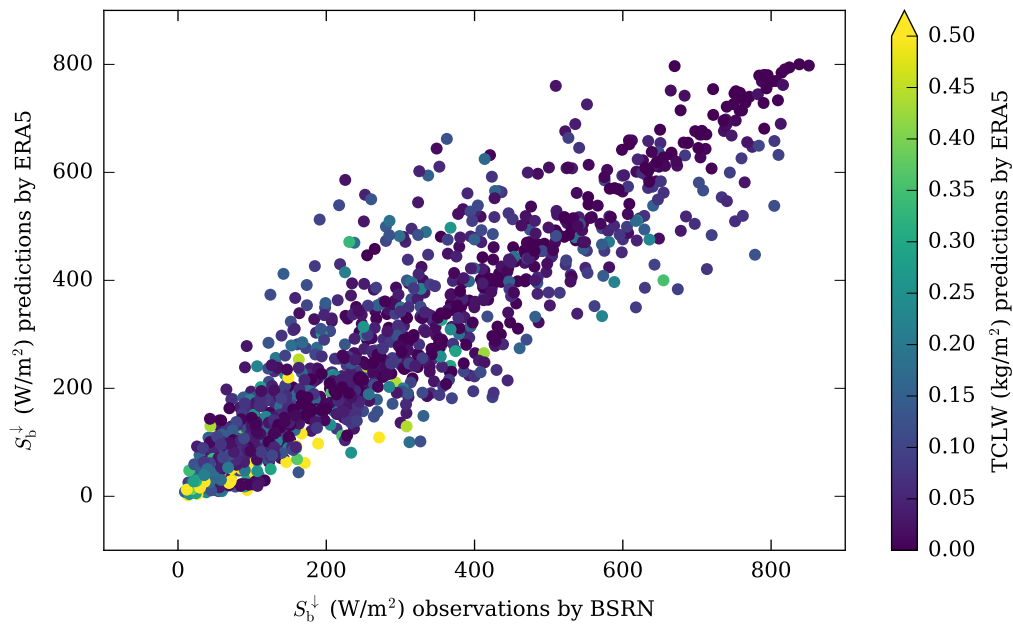

Figure A.6: Scatterplot of day-ahead forecasted $S_{\mathrm{b}}^{\downarrow}$ (W/m²) by GRASP-I and the associated observations by BSRN for 2016 at Cabauw, the Netherlands. Variables have been averaged in time over 3 hour windows. The points are color-coded with deviation between GRASP's prediction of the total column liquid water (kg/m²) and the associated re-analysis by ERA5.

Figure A.7: Scatterplot of day-ahead forecasted $S_{\mathrm{b}}^{\downarrow}$ (W/m²) by GRASP-I and the associated observations by BSRN for 2016 at Cabauw, the Netherlands. Variables have been averaged in time over 3 hour windows. The points are color-coded with deviation between GRASP's prediction of the total column liquid water (kg/m²) and the associated prediction by IFS.

Figure A.8: Scatterplot of day-ahead forecasted $S_{\mathrm{b}}^{\downarrow}$ (W/m²) by GRASP-P and the associated observations by BSRN for 2016 at Cabauw, the Netherlands. Variables have been averaged in time over 3 hour windows. The points are color-coded with GRASP's prediction of the liquid water content q_l (g/kg).
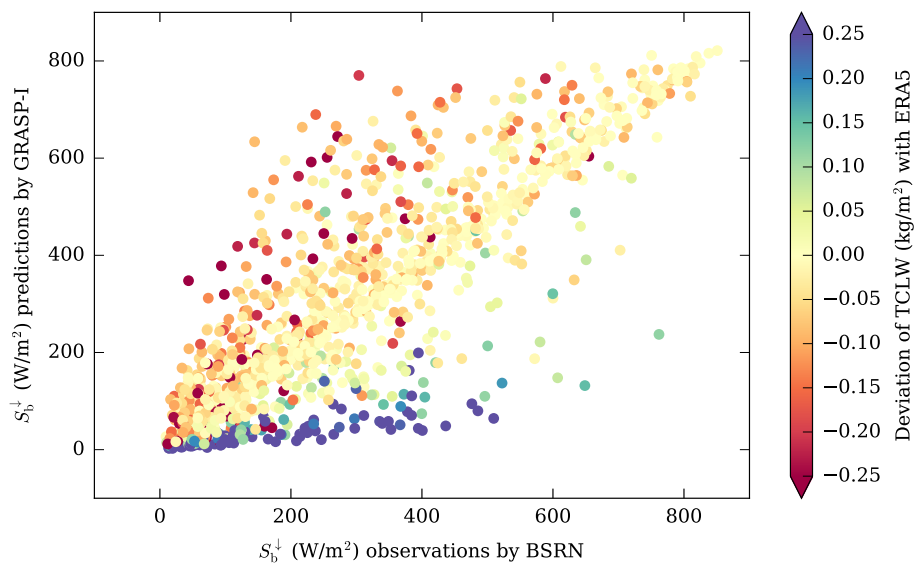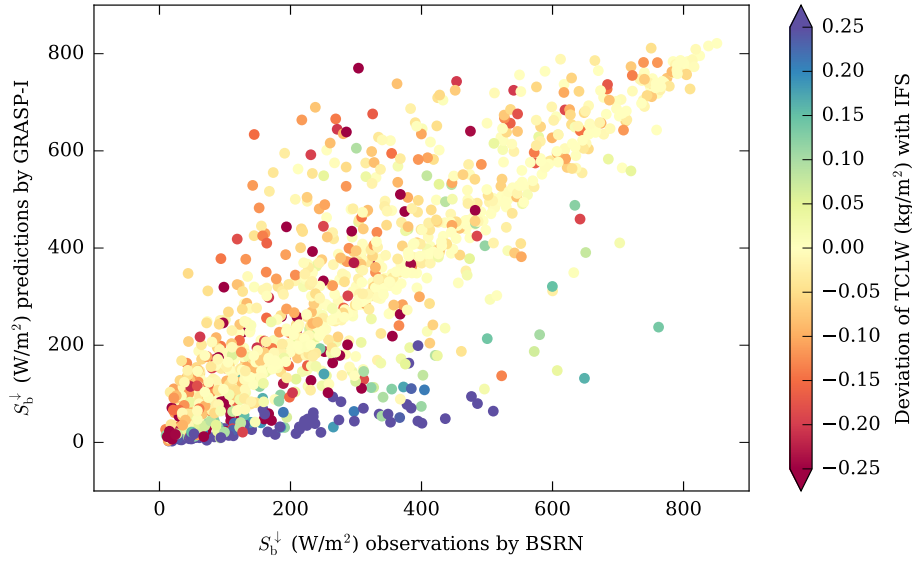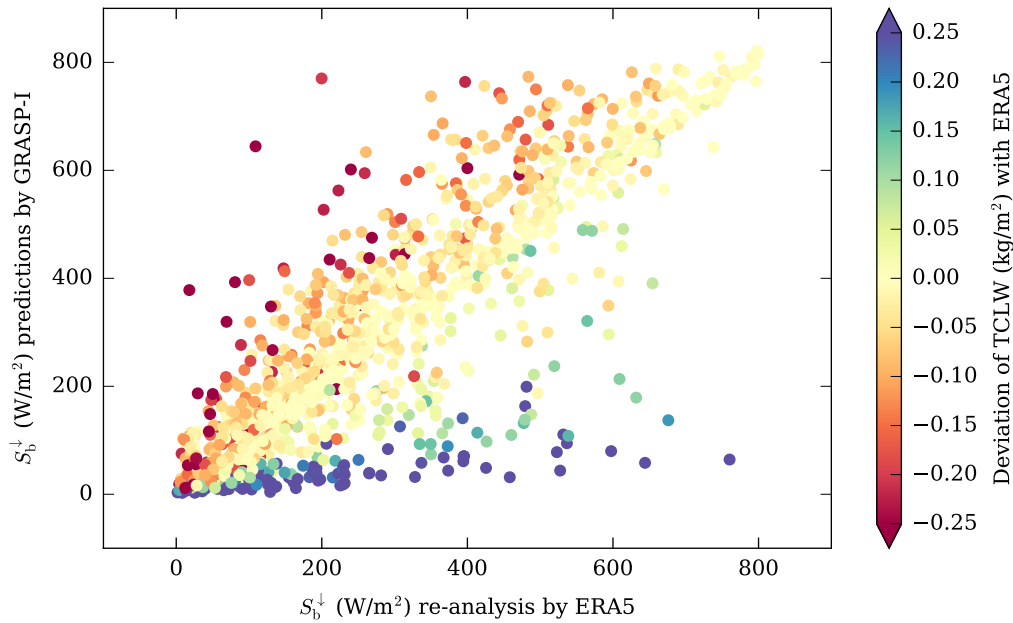
Figure A.9: Scatterplot of day-ahead forecasted $S_{\mathrm{b}}^{\downarrow}$ (W/m²) by GRASP-P and the associated observations by BSRN for 2016 at Cabauw, the Netherlands. Variables have been averaged in time over 3 hour windows. The points are color-coded with GRASP's prediction of the liquid water content q_l (g/kg).
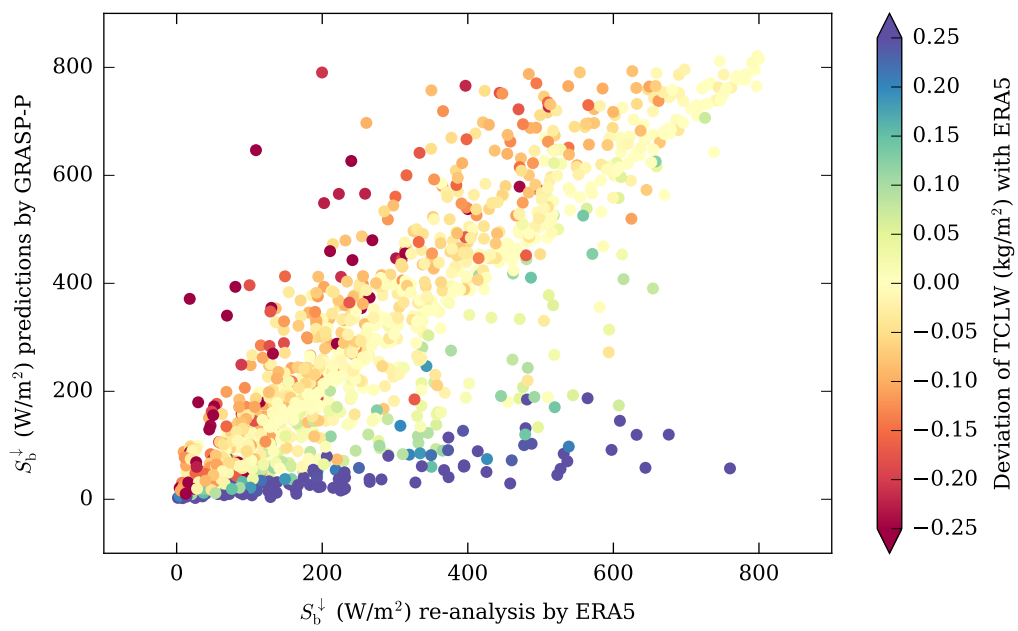
B

A Note on Statistics

In order to determine whether the implementation of cloud-radiation feedback is a success, a validation study was performed. To this end, the output of the GRASP models with and without cloud-radiation feedback were compared with observations. The forecasts of ECMWF's Integrated Forecasting System (IFS) are compared as well, to illustrate the performance of an established model, and to keep as a reference.

B.1 Statistical indicators

This section will explain which statistical indicators were used to assess the quality of the output of a certain model. Multiple models were compared with multiple observations, but the procedure for computing statistic indicators is always the same.

Let $y = (y_1, y_2, \ldots, y_n)$ be a vector of n predictions of a certain variable generated by model Y, and let $x = (x_1, x_2, \ldots, x_n)$ be the corresponding vector of the observed values that are being predicted. The mean of such a vector is calculated as the sum of all values divided by the number of values:

$$\bar{y} = \frac{1}{n} \sum_{i=1}^{n} y_i \tag{B.1}$$

which can be calculated for x in the exact same way.

For every data pair (x_i, y_i), the error $e_i = y_i - x_i$ is the difference between the predicted and the observed value. The bias is the mean of this error signal, $\text{Bias}(y, x) = \bar{e}$, which can be calculated by computing difference in the mean of both signals as such:

$$\begin{aligned} \text{Bias}(y, x) &= \frac{1}{n} \sum_{i=1}^{n} (y_i - x_i) \\ &= \frac{1}{n} \sum_{i=1}^{n} y_i - \frac{1}{n} \sum_{i=1}^{n} x_i \\ &= \bar{y} - \bar{x} \end{aligned} \tag{B.2}$$

The bias is thus a measure of the systematic error a model makes on average. It can convey useful information, but since positive and negative errors cancel out, it should not be interpreted as the average magnitude of the error. To that end, the mean absolute error (MAE) and the root mean squared error (RMSE) are some of the most widely used metrics in forecast evaluation studies. Their formulas, use and characteristics will be discussed here.

The MAE is a measure of the average magnitude of the errors, without taking their direction into account. It is calculated as:

$$\text{MAE}(y, x) = \frac{1}{n} \sum_{i=1}^{n} |y_i - x_i| \tag{B.3}$$

The RMSE is a similar measure of the average magnitude of the error, which is obtained by squaring the error before averaging and then taking the square root of the result:

$$\text{RMSE}(y, x) = \sqrt{\frac{1}{n} \sum_{i=1}^{n} (y_i - x_i)^2} \tag{B.4}$$

The use of either one of these statistic indicators has been the topic of debate within the climatic and environmental sciences. Willmott and Matsuura (2005) have for example suggested that the RMSE is an inappropriate and misinterpreted measure of the average error, and suggest that inter-comparisons based on output error should be based on MAE. On the other hand, Chai and Draxler (2014) have shown that there are cases when the RMSE is more appropriate to use than MAE.

A single metric only provides one projection of the characteristics of the model errors, and therefore it seems that neither metric alone can fully explain the nature of the errors. For that reason, this study presents a combination of statistical metrics including both MAE and RMSE in order to assess forecast performance, and attempts to understand the advantages and limitations of each of them.

Both MAE and RMSE express a measure of the average magnitude of the error between predictions and observations. They are both dimensioned, meaning that they express the model prediction error in the same units as the variable of interest. They are both negatively-oriented scores, which means low scores are better than high scores.

An important difference is that squaring the errors before taking the average causes the RMSE to be influenced more strongly by large errors than by small errors. The RMSE is thus not only a function of the magnitude of the error, but of the frequency distribution of error magnitudes as well. When large errors are especially undesirable, this means that the RMSE should be more useful. When the variance in errors is not of interest, the MAE is a less ambiguous indicator.

B.2 The bias-variance decomposition of the RMSE

Another useful feature of the RMSE is that it can be decomposed into two sources of error: a systemic error and a random error. The systemic error, also called bias, is the mean of the error between the predicted value and the observed value. The random error is the mean of the squared distance of any specific error from the mean error, also known as the standard deviation σ or the square root of the variance:

$$\sigma = \sqrt{\frac{1}{n} \sum_{i=1}^{n} [(e_i - \bar{e})^2]}. \tag{B.5}$$

In other words, the bias tells us the average error we can expect to find, and on top of that the standard deviation tells us how far the individual errors are spread out around this average

error. They are related as follows:

$$\sigma^2 = \frac{1}{n}\sum_{i=1}^{n}\left[(e_i - \bar{e})^2\right],$$

$$= \frac{1}{n}\sum_{i=1}^{n}\left[e_i^2 - 2\bar{e}e_i + \bar{e}^2\right],$$

$$= \frac{1}{n}\sum_{i=1}^{n}e_i^2 - \frac{2\bar{e}}{n}\sum_{i=1}^{n}e_i + \bar{e}^2,$$

$$= \frac{1}{n}\sum_{i=1}^{n}e_i^2 - 2\bar{e}^2 + \bar{e}^2,$$

$$= \frac{1}{n}\sum_{i=1}^{n}e_i^2 - \bar{e}^2,$$

$$= \underbrace{\frac{1}{n}\sum_{i=1}^{n}(y_i - x_i)^2}_{\text{RMSE}^2} - \underbrace{(\bar{y} - \bar{x})^2}_{\text{Bias}^2}. \tag{B.6}$$

The first term on the right hand side in equation B.6 can be recognized as the mean square error (MSE = RMSE^2) and the second term is the bias squared. In other words,

$$\text{RMSE}^2 = \sigma^2 + \text{bias}^2. \tag{B.7}$$

Bibliography

Abbe, C., 1901: The physical basis of long-range weather forecasts. *Monthly Weather Review*, **29 (12)**, 551–561.

Ahlgrimm, M., R. M. Forbes, J.-J. Morcrette, and R. A. Neggers, 2016: Arms impact on numerical weather prediction at ecmwf. *Meteorological Monographs*, **57**, 28–1.

Albrecht, B., M. Fang, and V. Ghate, 2016: Exploring stratocumulus cloud-top entrainment processes and parameterizations by using doppler cloud radar observations. *Journal of the Atmospheric Sciences*, **73 (2)**, 729–742.

Albrecht, B. A., 1991: Fractional cloudiness and cloud-top entrainment instability. *Journal of the atmospheric sciences*, **48 (12)**, 1519–1525.

Amaya, J., O. Cabrit, D. Poitou, B. Cuenot, and M. El Hafi, 2010: Unsteady coupling of navier–stokes and radiative heat transfer solvers applied to an anisothermal multicomponent turbulent channel flow. *Journal of Quantitative Spectroscopy and Radiative Transfer*, **111 (2)**, 295–301.

Andersson, E., and J. Thépaut, 2008: Ecmwfs 4d-var data assimilation system–the genesis and ten years in operations. *ECMWF Newsletter*, **115**, 8–12.

Arakawa, A., 2004: The cumulus parameterization problem: Past, present, and future. *Journal of Climate*, **17 (13)**, 2493–2525.

Arellano, J. V.-G., P. G. Duynkerke, and K. F. Zeller, 1995: Atmospheric surface layer similarity theory applied to chemically reactive species. *Journal of Geophysical Research: Atmospheres*, **100 (D1)**, 1397–1408.

Barker, H., J. Cole, J.-J. Morcrette, R. Pincus, P. Räisänen, K. von Salzen, and P. Vaillancourt, 2008: The monte carlo independent column approximation: An assessment using several global atmospheric models. *Quarterly Journal of the Royal Meteorological Society*, **134 (635)**, 1463–1478.

Bauer, P., A. Thorpe, and G. Brunet, 2015: The quiet revolution of numerical weather prediction. *Nature*, **525 (7567)**, 47.

Betts, A., 1973: Non-precipitating cumulus convection and its parameterization. *Quarterly Journal of the Royal Meteorological Society*, **99 (419)**, 178–196.

Boilley, A., C. Thomas, M. Marchand, E. Wey, and P. Blanc, 2016: The solar forecast similarity method: a new method to compute solar radiation forecasts for the next day. *Energy Procedia*, **91**, 1018–1023.

Böing, S., A. Siebesma, J. Korpershoek, and H. J. Jonker, 2012a: Detrainment in deep convection. *Geophysical Research Letters*, **39 (20)**.

Böing, S. J., H. J. Jonker, W. A. Nawara, and A. P. Siebesma, 2014: On the deceiving aspects of mixing diagrams of deep cumulus convection. *Journal of the Atmospheric Sciences*, **71 (1)**, 56–68.

Böing, S. J., H. J. Jonker, A. P. Siebesma, and W. W. Grabowski, 2012b: Influence of the subcloud layer on the development of a deep convective ensemble. *Journal of the Atmospheric Sciences*, **69 (9)**, 2682–2698.

Brunetti, M., and F. Prodi, 2015: The climate system. *EPJ Web of Conferences*, EDP Sciences, Vol. 98, 02001.

Chai, T., and R. R. Draxler, 2014: Root mean square error (rmse) or mean absolute error (mae)?–arguments against avoiding rmse in the literature. *Geoscientific model development*, **7 (3)**, 1247–1250.

Chandrasekhar, S., 1950: Radiative transfer. clarendon. Oxford.

Chen, T., W. B. Rossow, and Y. Zhang, 2000: Radiative effects of cloud-type variations. *Journal of climate*, **13 (1)**, 264–286.

Collow, A. B., V. P. Ghate, M. A. Miller, and L. C. Trabachino, 2016: A one-year study of the diurnal cycle of meteorology, clouds and radiation in the west african sahel region. *Quarterly Journal of the Royal Meteorological Society*, **142 (694)**, 16–29.

Curry, J. A., 1986: Interactions among turbulence, radiation and microphysics in arctic stratus clouds. *Journal of the atmospheric sciences*, **43 (1)**, 90–106.

de Roode, S. R., and P. G. Duynkerke, 1996: Dynamics of cumulus rising into stratocumulus as observed during the first lagrangianexperiment of astex. *Quarterly Journal of the Royal Meteorological Society*, **122 (535)**, 1597–1623.

de Roode, S. R., P. G. Duynkerke, and H. J. Jonker, 2004: Large-eddy simulation: How large is large enough? *Journal of the atmospheric sciences*, **61 (4)**, 403–421.

Deardorff, J., 1976: Usefulness of liquid-water potential temperature in a shallow-cloud model. *Journal of Applied Meteorology*, **15 (1)**, 98–102.

Deardorff, J., 1980: Cloud top entrainment instability. *Journal of the Atmospheric Sciences*, **37 (1)**, 131–147.

Deardorff, J. W., 1970: Preliminary results from numerical integrations of the unstable planetary boundary layer. *Journal of the Atmospheric Sciences*, **27 (8)**, 1209–1211.

Di Giuseppe, F., and A. M. Tompkins, 2015: *A parameterization of cloud overlap as a function of wind shear and its impact in ECMWF forecast.* European Centre for Medium-Range Weather Forecasts.

Dorrestijn, J., D. Crommelin, J. Biello, and S. Böing, 2013: A data-driven multi-cloud model for stochastic parametrization of deep convection. *Philosophical Transactions of the Royal Society A: Mathematical, Physical and Engineering Sciences*, **371 (1991)**, 20120 374.

Duynkerke, P., and A. Driedonks, 1988: Current problems in the stratocumulus-topped atmospheric boundary layer. *Scripta Metallurgica*.

Duynkerke, P. G., 1999: Turbulence, radiation and fog in dutch stable boundary layers. *Boundary-Layer Meteorology*, **90 (3)**, 447–477.

Duynkerke, P. G., H. Q. Zhang, and P. J. Jonker, 1995: Microphysical and turbulent structure of nocturnal stratocumulus as observed during astex. *Journal of the atmospheric sciences*, **52 (16)**, 2763–2777.

Ebell, K., S. Crewell, U. Löhnert, D. D. Turner, and E. J. O'Connor, 2011: Cloud statistics and cloud radiative effect for a low-mountain site. *Quarterly Journal of the Royal Meteorological Society*, **137 (S1)**, 306–324.

Edwards, J., S. Basu, F. Bosveld, and A. Holtslag, 2014: The impact of radiation on the gabls3 large-eddy simulation through the night and during the morning transition. *Boundary-layer meteorology*, **152 (2)**, 189–211.

Elterman, L., 1964: Atmospheric attenuation model, 1964, in the ultraviolet, visible, and infrared regions for altitudes to 50 km. Tech. rep., Air Force Cambridge Resarsch Labs Handscom AFB MA.

Emanuel, K. A., 1994: *Atmospheric convection*. Oxford University Press on Demand.

Fefferman, C. L., 2006: Existence and smoothness of the navier-stokes equation. *The millennium prize problems*, **57**, 67.

Fidaros, D., C. Baxevanou, T. Bartzanas, and C. Kittas, 2010: Numerical simulation of thermal behavior of a ventilated arc greenhouse during a solar day. *Renewable Energy*, **35 (7)**, 1380–1386.

Franzke, C. L., T. J. O'Kane, J. Berner, P. D. Williams, and V. Lucarini, 2015: Stochastic climate theory and modeling. *Wiley Interdisciplinary Reviews: Climate Change*, **6 (1)**, 63–78.

Fu, Q., and K. Liou, 1992: On the correlated k-distribution method for radiative transfer in nonhomogeneous atmospheres. *Journal of the Atmospheric Sciences*, **49 (22)**, 2139–2156.

Fu, Q., K. Liou, M. Cribb, T. Charlock, and A. Grossman, 1997: Multiple scattering parameterization in thermal infrared radiative transfer. *Journal of the atmospheric sciences*, **54 (24)**, 2799–2812.

Goody, R., and Y. Yung, 1989: Radiation: Theoretical basis. Oxford University Press, Oxford, UK.

Guan, H., M. Yau, and R. Davies, 1997: The effects of longwave radiation in a small cumulus cloud. *Journal of the atmospheric sciences*, **54 (17)**, 2201–2214.

Hanjalić, K., S. Kenjeres, M. Tummers, and H. Jonker, 2007: *Analysis and modelling of physical transport phenomena*. VSSD.

Hanson, H. P., 1984: On mixed-layer modeling of the stratocumulus-topped marine boundary layer. *Journal of the atmospheric sciences*, **41 (7)**, 1226–1234.

Hersbach, H., and D. Dee, 2016: Era5 reanalysis is in production. *ECMWF newsletter*, **147 (7)**.

Heus, T., and Coauthors, 2010: Formulation of and numerical studies with the dutch atmospheric large-eddy simulation (dales). *Geosci. Model Dev*, **3**, 415–444.

Hogan, R. J., and A. Bozzo, 2016: *ECRAD: A new radiation scheme for the IFS*. European Centre for Medium-Range Weather Forecasts.

Hogan, R. J., and S. Hirahara, 2015: *Effect of solar zenith angle specification on mean shortwave fluxes and stratospheric temperatures*. European Centre for Medium-Range Weather Forecasts.

Hogan, R. J., and Coauthors, 2017: *Radiation in numerical weather prediction*. European Centre for Medium-Range Weather Forecasts.

Iacono, M. J., J. S. Delamere, E. J. Mlawer, M. W. Shephard, S. A. Clough, and W. D. Collins, 2008: Radiative forcing by long-lived greenhouse gases: Calculations with the aer radiative transfer models. *Journal of Geophysical Research: Atmospheres*, **113 (D13)**.

Ineichen, P., 2016: Validation of models that estimate the clear sky global and beam solar irradiance. *Solar Energy*, **132**, 332–344.

Jiang, H., and W. R. Cotton, 2000: Large eddy simulation of shallow cumulus convection during bomex: Sensitivity to microphysics and radiation. *Journal of the atmospheric sciences*, **57 (4)**, 582–594.

Kato, S., T. P. Ackerman, J. H. Mather, and E. E. Clothiaux, 1999: The k-distribution method and correlated-k approximation for a shortwave radiative transfer model. *Journal of Quantitative Spectroscopy and Radiative Transfer*, **62 (1)**, 109–121.

Knap, W., J. Bijma, Y. Hinssen, A. Los, C. van Oort, J. Warmer, and E. Worrell, 2010: The baseline surface radiation network (bsrn) station at the cabauw observatory. Tech. rep., Tech. Rep.

Ladyzhenskaya, O. A., 2003: Sixth problem of the millennium: Navier-stokes equations, existence and smoothness. *Russian Mathematical Surveys*, **58 (2)**, 251.

Lange, M., and U. Focken, 2006: *Physical approach to short-term wind power prediction.* Springer.

Larson, V. E., K. E. Kotenberg, and N. B. Wood, 2007: An analytic longwave radiation formula for liquid layer clouds. *Monthly weather review*, **135 (2)**, 689–699.

Lilly, D. K., 1968: Models of cloud-topped mixed layers under a strong inversion. *Quarterly Journal of the Royal Meteorological Society*, **94 (401)**, 292–309.

Liu, Y., W. Wu, M. Jensen, and T. Toto, 2011: Relationship between cloud radiative forcing, cloud fraction and cloud albedo, and new surface-based approach for determining cloud albedo. *Atmospheric Chemistry and Physics*, **11 (14)**, 7155–7170.

Lorenz, E., J. Hurka, D. Heinemann, and H. G. Beyer, 2009: Irradiance forecasting for the power prediction of grid-connected photovoltaic systems. *IEEE Journal of selected topics in applied earth observations and remote sensing*, **2 (1)**, 2–10.

Lynch, P., 2006: *The emergence of numerical weather prediction: Richardson's dream.* Cambridge University Press.

MacVean, M., and P. Mason, 1990: Cloud-top entrainment instability through small-scale mixing and its parameterization in numerical models. *Journal of the Atmospheric Sciences*, **47 (8)**, 1012–1030.

Marquardt Collow, A. B., and M. A. Miller, 2016: The seasonal cycle of the radiation budget and cloud radiative effect in the amazon rain forest of brazil. *Journal of Climate*, **29 (21)**, 7703–7722.

Mathiesen, P., and J. Kleissl, 2012: *Evaluation of Numerical Weather Prediction for Solar Forecasting: Final Project Report.* California Energy Commission.

Mauritsen, T., and Coauthors, 2012: Tuning the climate of a global model. *Journal of advances in modeling Earth systems*, **4 (3)**.

Mc Garrigle, E., and P. Leahy, 2013: The value of accuracy in wind energy forecasts. *2013 12th International Conference on Environment and Electrical Engineering*, IEEE, 529–533.

Mellado, J. P., 2017: Cloud-top entrainment in stratocumulus clouds. *Annual Review of Fluid Mechanics*, **49**, 145–169.

Mlawer, E. J., S. J. Taubman, P. D. Brown, M. J. Iacono, and S. A. Clough, 1997: Radiative transfer for inhomogeneous atmospheres: Rrtm, a validated correlated-k model for the longwave. *Journal of Geophysical Research: Atmospheres*, **102 (D14)**, 16 663–16 682.

Moeng, C.-H., D. H. Lenschow, and D. A. Randall, 1995: Numerical investigations of the roles of radiative and evaporative feedbacks in stratocumulus entrainment and breakup. *Journal of the atmospheric sciences*, **52 (16)**, 2869–2883.

Morcrette, J., H. W. Barker, J. Cole, M. J. Iacono, and R. Pincus, 2008: Impact of a new radi-
    ation package, mcrad, in the ecmwf integrated forecasting system. *Monthly weather review*,
    136 (12), 4773–4798.

Morcrette, J., and Coauthors, 2007: Recent advances in radiation transfer parameterizations.
    ECMWF Research Department Technical Memorandum, **(593)**, 50.

Paltridge, G. W., and C. M. R. Platt, 1976: *Radiative processes in meteorology and climatology*.
    Elsevier Scientific Pub. C.

Parding, K., L. M. Hinkelman, T. P. Ackerman, and S. A. McFarlane, 2011: Shortwave absorp-
    tance in a tropical cloudy atmosphere: Reconciling calculations and observations. *Journal
    of Geophysical Research: Atmospheres*, **116 (D19)**.

Perez, R., S. Kivalov, J. Schlemmer, K. Hemker Jr, D. Renné, and T. E. Hoff, 2010: Validation
    of short and medium term operational solar radiation forecasts in the us. *Solar Energy*,
    84 (12), 2161–2172.

Perez, R., and Coauthors, 2013: Comparison of numerical weather prediction solar irradiance
    forecasts in the us, canada and europe. *Solar Energy*, **94**, 305–326.

Pincus, R., H. W. Barker, and J.-J. Morcrette, 2003: A fast, flexible, approximate technique for
    computing radiative transfer in inhomogeneous cloud fields. *Journal of Geophysical Research:
    Atmospheres*, **108 (D13)**.

Pincus, R., P. M. Forster, and B. Stevens, 2016: The radiative forcing model intercompar-
    ison project (rfmip): Experimental protocol for cmip6. *Geoscientific Model Development
    (Online)*, **9 (9)**.

Pincus, R., C. Hannay, and K. F. Evans, 2005: The accuracy of determining three-dimensional
    radiative transfer effects in cumulus clouds using ground-based profiling instruments. *Journal
    of the atmospheric sciences*, **62 (7)**, 2284–2293.

Pincus, R., and B. Stevens, 2009: Monte carlo spectral integration: A consistent approximation
    for radiative transfer in large eddy simulations. *Journal of Advances in Modeling Earth
    Systems*, **1 (2)**.

Pincus, R., and B. Stevens, 2013: Paths to accuracy for radiation parameterizations in atmo-
    spheric models. *Journal of Advances in Modeling Earth Systems*, **5 (2)**, 225–233.

Räisänen, P., and H. W. Barker, 2004: Evaluation and optimization of sampling errors for the
    monte carlo independent column approximation. *Quarterly Journal of the Royal Meteoro-
    logical Society*, **130 (601)**, 2069–2085.

Randall, D. A., 1984: Stratocumulus cloud deepening through entrainment. *Tellus A: Dynamic
    Meteorology and Oceanography*, **36 (5)**, 446–457.

Reda, I., and A. Andreas, 2004: Solar position algorithm for solar radiation applications. *Solar
    energy*, **76 (5)**, 577–589.

Richardson, L. F., 1922: Weather prediction by numerical process cambridge university press.
    Cambridge Richardson Weather prediction by numerical process, **1922**.

Rodgers, C., 1968: Some extensions and applications of the new random model for molecular
    band transmission. *Quarterly Journal of the Royal Meteorological Society*, **94 (399)**, 99–102.

Roesch, A., M. Wild, A. Ohmura, E. G. Dutton, C. N. Long, and T. Zhang, 2011: Assessment
    of bsrn radiation records for the computation of monthly means. *Atmospheric Measurement
    Techniques*, **4 (2)**, 339–354.

Roger, M., C. B. Da Silva, and P. J. Coelho, 2009: Analysis of the turbulence–radiation interactions for large eddy simulations of turbulent flows. *International Journal of Heat and Mass Transfer*, **52 (9-10)**, 2243–2254.

Roulston, M. S., D. T. Kaplan, J. Hardenberg, and L. A. Smith, 2003: Using medium-range weather forcasts to improve the value of wind energy production. *Renewable Energy*, **28 (4)**, 585–602.

Russchenburg, H., and Coauthors, 2002: Cesar: Cabauw experimental site for atmospheric research. *Proceedings of the XXVIIth General Assembly of the International Union of Radio Science, 17-24 August., 2002, Maastricht, The Netherlands*, np–np.

Schalkwijk, J., E. J. Griffith, F. H. Post, and H. J. Jonker, 2012: High-performance simulations of turbulent clouds on a desktop pc: Exploiting the gpu. *Bulletin of the American Meteorological Society*, **93 (3)**, 307–314.

Schalkwijk, J., H. J. Jonker, A. P. Siebesma, and F. C. Bosveld, 2015a: A year-long large-eddy simulation of the weather over cabauw: An overview. *Monthly Weather Review*, **143 (3)**, 828–844.

Schalkwijk, J., H. J. Jonker, A. P. Siebesma, and E. Van Meijgaard, 2015b: Weather forecasting using gpu-based large-eddy simulations. *Bulletin of the American Meteorological Society*, **96 (5)**, 715–723.

Seifert, A., T. Heus, R. Pincus, and B. Stevens, 2015: Large-eddy simulation of the transient and near-equilibrium behavior of precipitating shallow convection. *Journal of Advances in Modeling Earth Systems*, **7 (4)**, 1918–1937.

Siebesma, A. P., and Coauthors, 2003: A large eddy simulation intercomparison study of shallow cumulus convection. *Journal of the Atmospheric Sciences*, **60 (10)**, 1201–1219.

Smagorinsky, J., 1963: General circulation experiments with the primitive equations: I. the basic experiment. *Monthly weather review*, **91 (3)**, 99–164.

Solomon, S., 2007: Ipcc (2007): climate change the physical science basis. *AGU Fall Meeting Abstracts*, 96.

Stevens, B., 2015: Rethinking the lower bound on aerosol radiative forcing. *Journal of Climate*, **28 (12)**, 4794–4819.

Stevens, B., W. R. Cotton, G. Feingold, and C.-H. Moeng, 1998: Large-eddy simulations of strongly precipitating, shallow, stratocumulus-topped boundary layers. *Journal of the atmospheric sciences*, **55 (24)**, 3616–3638.

Stevens, B., and Coauthors, 2003: On entrainment rates in nocturnal marine stratocumulus. *Quarterly Journal of the Royal Meteorological Society*, **129 (595)**, 3469–3493.

Stowasser, M., and K. Hamilton, 2006: Relationship between shortwave cloud radiative forcing and local meteorological variables compared in observations and several global climate models. *Journal of climate*, **19 (17)**, 4344–4359.

Thomas, G. E., and K. Stamnes, 2002: *Radiative transfer in the atmosphere and ocean*. Cambridge University Press.

Urraca, R., A. M. Gracia-Amillo, T. Huld, F. J. Martinez-de Pison, J. Trentmann, A. V. Lindfors, A. Riihelä, and A. Sanz-Garcia, 2017: Quality control of global solar radiation data with satellite-based products. *Solar Energy*, **158**, 49–62.

Verbois, H., R. Huva, A. Rusydi, and W. Walsh, 2018: Solar irradiance forecasting in the tropics using numerical weather prediction and statistical learning. *Solar Energy*, **162**, 265–277.

Williams, D., 2007: Nasa sun fact sheet.

Williams, D. R., 2004: Earth fact sheet. *Structural geology of the Earths interior: Proc. Natl. Acad. Sci. NASA (17 Nov 2010)*, **76 (9)**.

Willmott, C. J., and K. Matsuura, 2005: Advantages of the mean absolute error (mae) over the root mean square error (rmse) in assessing average model performance. *Climate research*, **30 (1)**, 79–82.

Wyngaard, J. C., 2004: Toward numerical modeling in the terra incognita. *Journal of the atmospheric sciences*, **61 (14)**, 1816–1826.

Yamaguchi, T., and D. A. Randall, 2008: Large-eddy simulation of evaporatively driven entrainment in cloud-topped mixed layers. *Journal of the Atmospheric Sciences*, **65 (5)**, 1481–1504.

Zamora, R. J., E. G. Dutton, M. Trainer, S. A. McKeen, J. M. Wilczak, and Y.-T. Hou, 2005: The accuracy of solar irradiance calculations used in mesoscale numerical weather prediction. *Monthly weather review*, **133 (4)**, 783–792.